Planning and Optimization Algorithms for Image-Guided Medical Procedures

by

Ron Alterovitz

B.S. (California Institute of Technology) 2001M.S. (University of California, Berkeley) 2003

A dissertation submitted in partial satisfaction of the requirements for the degree of

Doctor of Philosophy

in

Engineering - Industrial Engineering and Operations Research

in the

GRADUATE DIVISION

of the

UNIVERSITY OF CALIFORNIA, BERKELEY

Committee in charge:

Professor Ken Goldberg, Chair Professor Jean Pouliot Professor Alper Atamtürk Professor James O'Brien

Fall 2006

The dissertation of Ron Alterovitz is approved.

Chair	Date
	Date
	Date
	Date
	Date
	D 0000

University of California, Berkeley Fall 2006 Planning and Optimization Algorithms for Image-Guided Medical Procedures

Copyright © 2006

by

Ron Alterovitz

Abstract

Planning and Optimization Algorithms for Image-Guided Medical Procedures

by

Ron Alterovitz

Doctor of Philosophy in Engineering - Industrial Engineering and Operations

Research

University of California, Berkeley

Professor Ken Goldberg, Chair

Exciting advances in medical imaging are enabling clinicians to noninvasively examine anatomy and metabolic processes deep below the skin's surface. To effectively utilize this new wealth of digital information, new computational methods are needed to plan and optimize medical procedures on a patient-specific basis. In this dissertation, we combine ideas from robotics, physically-based modeling, and operations research to develop new planning and optimization algorithms for image-guided medical procedures.

We focus on four planning and optimization problems, each of which introduces new computational challenges and is subject to unique constraints imposed by the physician's treatment requirements, the patient's anatomy, and the physical limitations of medical equipment and devices. First, we develop an image registration method that explicitly considers tissue deformation when mapping targets between images acquired at different times. Results using prostate medical images indicate a statistically significant improvement in registration accuracy compared to previous methods. Second, we develop a motion planning algorithm for traditional needle insertion procedures to correct for tissue deformation caused by forces exerted by the needle. The method, which combines a finite element model of soft tissue with numerical optimization, is applicable to a variety of minimally invasive

procedures, from biopsies to cancer treatments such as cryotherapy and brachytherapy. Third, we develop a nonholonomic motion planning algorithm that explicitly considers uncertainty in motion, and we apply it to a new class of highly flexible bevel-tip needles that can be steered to targets in soft tissue previously inaccessible to stiff needles. The algorithm combines geometric planning with Markov Decision Processes and Dynamic Programming. Results indicate that traditional shortest paths do not maximize the probability of successfully acquiring the target when the needle's response to controls is not known with certainty. Fourth, we consider dose optimization for high-dose-rate brachytherapy cancer treatment, a medical procedure in which physicians place radioactive sources in close proximity to cancer cells. We formulate the dose optimization problem as a linear program, enabling the fast

computation of mathematically optimal solutions and the statistical validation of interna-

tionally used clinical planning software. Overall, these results advance the development of

new planning and optimization algorithms for image-guided medical procedures.

Professor Ken Goldberg Dissertation Committee Chair

To my family...

Contents

\mathbf{C}	onter	$_{ m nts}$		ii
Li	st of	Figur	es	vi
Li	st of	Table	${f s}$	xii
\mathbf{A}	ckno	wledge	ements	xiii
1	Intr	oduct	ion	1
	1.1	Plann	ing and Optimization Algorithms	3
		1.1.1	Target Localization in Deformable Tissues	4
		1.1.2	Motion Planning for Rigid Needles in Deformable Tissue	5
		1.1.3	Motion Planning for Steerable Needles	5
		1.1.4	Dose Optimization for Brachytherapy Cancer Treatment	6
	1.2	Brach	ytherapy for Treating Prostate Cancer	6
	1.3	Contr	ibutions	9
	1.4	Disser	rtation Overview	10
2	Bio	mecha	nical Modeling and Simulation of Soft Tissue Deformations	12
	2.1	Funda	amentals of Continuum Mechanics	14
		2.1.1	Deformable Bodies	15
		2.1.2	The 1-D Case	16
		2.1.3	The 3-D Case	18
		2.1.4	The 2-D Case	21
	2.2	Simul	ating Soft Tissue Deformations	21
		2.2.1	Mass-Spring Method	21

		2.2.2	Finite Element Method	22
	2.3	Simul	ating Needle Procedures	28
		2.3.1	Related Work on Needle Insertion and Surgery Simulation	28
		2.3.2	Input Anatomy Model	29
		2.3.3	Model of Needle Insertion	30
		2.3.4	Cutting at the Needle Tip	31
		2.3.5	Friction Along the Needle Shaft	33
		2.3.6	Needle Retraction	33
		2.3.7	Visualization of Needle Insertion	34
	2.4	Applie	cation to Prostate Brachytherapy Cancer Treatment	34
	2.5	Concl	usion and Future Work	35
0	T D-	T	and and an entire Defense like Langua Destruction	9.0
3		_	calization using Deformable Image Registration	38
	3.1		luction to Deformable Image Registration	39
	3.2		mable Registration with Model Parameter Estimation	42
		3.2.1	Method Input	42
		3.2.2	Finite Element Model of Soft Tissue Deformation	43
		3.2.3	Quality Metric	44
		3.2.4	Optimization of Uncertain Parameters	44
		3.2.5	Visualizing Registration Output	45
	3.3		cation to Prostate Cancer Treatment	46
		3.3.1	Patient Image Acquisition	50
		3.3.2	Application of the Deformable Registration Method	51
		3.3.3	Warping the MRSI Grid	53
		3.3.4	Method Evaluation and Parameter Selection	54
		3.3.5	Results	54
		3.3.6	Discussion	57
	3.4	Concl	usion and Future Work	60
4	Mo	tion P	lanning for Rigid Needles in Deformable Soft Tissue	61
	4.1		ed Work: Sensorless Planning and Needle Insertion	63
	4.2		em Definition	64
	4.3		e Insertion Planning Method	66
			Method Overview	66

		4.3.2	Planning Method	67
	4.4	Applic	ation to Brachytherapy Seed Implantation	71
		4.4.1	Target Test Case	72
		4.4.2	Optimizing Insertion Depth	72
		4.4.3	Optimizing Insertion Height	73
	4.5	Conclu	sion and Future Work	74
5	Mo	tion Pl	anning for Steerable Needles	76
	5.1	Uncert	ainty and Motion Planning	77
	5.2	Relate	d Work on Nonholonomic Motion Planning and MDP's	80
	5.3	Motion	n Planning Problem Definition	81
	5.4	Motion	n Planning Method	83
		5.4.1	Problem Formulation	83
		5.4.2	State Space Discretization	84
		5.4.3	Optimization Using Infinite Horizon Dynamic Programming	86
	5.5	Compu	ntational Results	87
	5.6	Conclu	sion and Future Work	90
6	Dos	se Opti	mization for High-Dose-Rate Brachytherapy	93
	6.1	Introd	uction to HDR Brachytherapy and Dose Optimization	95
	6.2	Linear	Programming for HDR Brachytherapy	96
		6.2.1	Patient Data Input	98
		6.2.2	Dose Calculation	96
		6.2.3	Clinical Criteria	96
		6.2.4	Linear Programming Formulation	100
	6.3	Applic	ation to Prostate Cancer Treatment	103
		6.3.1	Patient Data Sets	104
		6.3.2	Evaluation Metrics	105
		6.3.3	Results	105
	6.4	Discus	sion	107
	6.5	Conclu	asion and Future Work	110
7	Cor	nclusion	1	113
	7.1	Contri	butions	114

Bibliog	graphy		120
7.3	Concl	usion	119
	7.2.2	Planning Algorithms for Image-Guided Medical Procedures $\ \ldots \ \ldots$	118
	7.2.1	Realistic Simulation of Image-Guided Medical Procedures	116
7.2	Future	e Work	116
	7.1.4	Dose Optimization for Brachytherapy Cancer Treatment	115
	7.1.3	Motion Planning for Steerable Needles	115
	7.1.2	Motion Planning for Rigid Needles in Deformable Tissue	114
	7.1.1	Target Localization using Deformable Image Registration	114

List of Figures

1.1	Information flow for computer-assisted image-guided medical procedures. In this dissertation, we focus on developing computational tools: planning/optimization algorithms and physically-based simulation algorithms	3
1.2	MRSI data for the prostate is obtained with a balloon endorectal probe, as shown in an axial MR image at the mid-gland of the prostate (a). Radiation treatment is performed with the probe removed (b). The balloon endorectal probe causes substantial deformation of the prostate	4
1.3	The prostate, shown here in the sagittal plane, consists of multiple zones, including the anterior fibromuscular band, the central zone, and the peripheral zone [88, 40]. In this figure, the cranial direction is to the left	7
1.4	During permanent seed brachytherapy (a), needles carrying radioactive seeds are inserted transperineally into the patient, who is lying on his back [131]. The quality of intra-operative transrectal ultrasound images is very poor (b), making it difficult to track the penetration of the needle into the deformed prostate	8
2.1	A deformable body B in its reference state is deformed to B' by displacement field u	16
2.2	A 1-D bar of length L in the reference state (a). Due to force f , the bar extends to length $L + \Delta$ in the deformed state	16
2.3	The components of the stress tensor σ in 3-D for an infinitesimal cube from a deformable body B	19
2.4	A regular mass-spring mesh for a 2-D object. The horizontal and vertical springs resist compression or tension while the diagonal springs are required to resist pure shear strains	22
2.5	A 2-D finite element reference mesh G composed of triangular elements is shown in (a). The deformed mesh G' is shown in (b). The node labeled with \times in mesh G is displaced by vector \mathbf{u} in deformed mesh G'	24
2.6	Slice of deformable tissue in the yz plane. The needle is inserted from right to left parallel to the z -axis, causing the tissue to deform	30
2.7	The needle is in the interior of the mesh with needle tip node $c=i$ at point p .	31

2.8	The needle tip is inserted to the left in (a) through (c). The tip node is moved onto the shaft in (c) and the next tip node is selected	32
2.9	A portion of a reference mesh with a needle path (the dotted line) is shown in (a) with tip node i and shaft nodes l and h . As the tip node i moves downward in (b) and (c), triangle (i, l, h) becomes degenerate	33
2.10	The simulation user interface, which is based on an ultrasound image, is intended to mimic the experience of a physician performing brachytherapy. The physician interactively guides the needle using a mouse and implants seeds (small squares). Tissue deformations and seed locations are predicted and displayed. The implantation error is the distance between the seed and its target (cross) after needle retraction	36
2.11	Sample frames from a simulation of brachytherapy needle insertion based on deforming an ultrasound image of the human prostate using our finite element model	36
3.1	Fixed image F and a moving image M are enclosed in dashed lines. The object of interest in F is translated and rotated in M . The transformation T defines a rigid transformation that maps points \mathbf{x} from F to \mathbf{x}' in M	40
3.2	Fixed image F and a moving image M are enclosed in dashed lines. The object of interest in F is translated, rotated, and deformed in M . The transformation T defines a deformable transformation that maps points \mathbf{x} from F to \mathbf{x}' in M	40
3.3	MRSI data for the prostate is obtained with a balloon endorectal probe inserted and inflated (a) or a rigid endorectal probe (c) as shown in the axial MR images at the mid-gland of the prostate. Radiation treatment is performed with the probe removed (b), (d)	47
3.4	Spectroscopy data is obtained for voxels inside the MRSI grid overlaid on an the axial probe-in MR image (a). Our image registration method warps the MRSI grid to the probe-out image for use during treatment planning (b).	48
3.5	Conformal Delaunay triangular mesh (black triangles) for a probe-out image with central gland and peripheral zone of the prostate, probe entry location (rectum), and bones segmented (in white)	52
3.6	Probe-out image A with segmented prostate gland (outlined in white, middle) and rectum (outlined in white, bottom) (a) and the corresponding probe-in image B with prostate and probe segmented (b). The method computes image $F(A)$ (c) which displaces mesh nodes along the rectum in the probe-out image to the probe outline in the probe-in image and estimates the resulting soft tissue deformations. The image registration quality (DSC value) between (b) and (c) is 97.8%	53
3.7	Sensitivity of mean image registration quality (DSC and point errors) to the	56

3.8	Sensitivity of mean DSC image registration quality (a) and computation time (b) to the number of nodes n in the mesh, with error bars for standard deviations	56
3.9	Sample balloon probe case. A comparison of input and output images shows the nonlinear warping of the MRSI grid. The probe-in image (a) closely matches the computed deformed probe-out image (b) outside the endorectal probe. The MRSI grid is warped to the undeformed probe-out image (c) for use during treatment planning	57
3.10	Sample rigid probe case	58
4.1	Four vertical frames illustrate brachytherapy needle insertion based on deforming an ultrasound image of the human prostate using simulation. The left column shows results without planning, producing substantial placement error. The right column shows results with the sensorless plan, with minimal placement error. The target implant location is indicated in all frames with a cross fixed in the world frame. Frame (a) outlines the undeformed prostate. In Frame (b), the needle is inserted and the radioactive seed (small square) is released at the needle tip. In Frame (c), the needle is retracted. Frame (d) indicates the resulting placement error, the distance between the target and resulting actual seed location. Without planning, placement error is substantial: 26% of the prostate diameter, resulting in damage to healthy tissue and failure to kill cancerous cells. With sensorless planning, shown in the bottom image of Frame (d), placement error is negligible in this simulation.	62
4.2	Slice of deformable tissue in the yz plane. The needle is inserted from right to left parallel to the z -axis, causing the tissue to deform	65
4.3	Consider a mesh representation of soft tissue as defined in chapter 2 used for simulation. Let the target be located at node k of the mesh. At time step $i=0$, the coordinate of the target in the reference mesh, denoted by \times , coincides with the target in the world frame, denoted by \bullet , because displacement $\mathbf{u_{k0}}$ of node k is 0 (a). At time step $i>0$, the tissue is deformed (b). Both the \times and \bullet represent the same location within the tissue, but the world frame coordinate differs from the reference frame coordinate by the displacement $\mathbf{u_{ki}} \neq 0$	67
4.4	When the needle pushes against the lower half of the prostate from the right, the prostate rotates clockwise slightly because it is stiffer than the surrounding tissue. This slight rotation can lead to significant changes in the optimal needle insertion height	68
4.5	Needles should generally be inserted deeper than the target depth to compensate for tissue deformations and minimize placement error. The bold portion of the line denotes feasible seed placements inside the prostate	72
4.6	For all candidate insertion heights y_r , optimal depth z_r^* (a) and resulting error (b) are computed. Placement error is negligible for $\mathbf{p_r} = (1.59 \text{ cm}, 3.80 \text{ cm})$.	73

4.7	Twelve sample points were selected as targets marked "+" inside the prostate. Actual seed placements using simulation are marked "•". Lack of planning results in major placement errors averaging 20% of the prostate diameter (a), which will lead to a poor radioactive dose distribution. Placement error was neglible using the planner (b)	74
5.1	Our motion planner computes controls (insertions and direction changes, indicated by dots) to steer the needle from an insertion entry region (vertical line on left between the solid squares) to the target (open circle) inside soft tissue, without touching critical areas indicated by polygonal obstacles in the imaging plane. The motion of the needle is not known with certainty; the needle tip may be deflected during insertion due to tissue inhomogeneities or other unpredictable soft tissue interactions. We explicitly consider this uncertainty to generate motion plans to maximize the probability of success, P_s , the probability that the needle will reach the target without colliding with an obstacle or exiting the workspace boundary. Relative to minimizing path length, our planner can generate longer paths with greater clearance from obstacles to maximize P_s	79
5.2	The state of a steerable needle during insertion is characterized by tip position \mathbf{p} , tip orientation angle θ , and bevel direction b (a). Rotating the needle about its base changes the bevel direction but does not affect needle position (b). The needle will cut soft tissue along an arc (dotted vector) based on bevel direction	82
5.3	A needle in the bevel-left direction with orientation θ is tracing the solid control circle with radius r (a). A direction change would result in tracing the dotted circle. The control circle is divided into $N_c = 40$ discrete arcs of length δ (b). The control circle points are rounded to the nearest point on the Δ -density grid, and transitions for insertion of distance δ are defined by the vectors between rounded control circle points (c)	85
5.4	When the needle is inserted, the insertion angle θ may be deflected by some angle β . We model the probability distribution of β using a normal distribution with mean 0 and standard deviation σ_i for insertion or σ_r for direction change. For a discrete sample of deflections ($\beta = \{-2\alpha, -\alpha, 0, \alpha, 2\alpha\}$), we obtain the probability of each deflection by integrating the corresponding area under the normal curve.	86
5.5	As in figure 5.1, optimal plans maximizing the probability of success P_s illustrate the importance of considering uncertainty in needle motion. The shortest path plan passes through a narrow gap between obstacles (a). Since maximizing P_s explicitly considers uncertainty, the optimal expected path has greater clearance from obstacles, decreasing the probability that large deflections will cause failure to reach the target. Here we consider medium (b) and large (c) variance in tip deflections for a needle with smaller radius of curvature than in figure 5.1	88

5.6	Optimal plans demonstrate the importance of considering uncertainty in needle motion, where σ_i and σ_r are the standard deviations of needle tip deflections that can occur during insertion and direction changes, respectively. For higher σ_r relative to σ_i , the optimal plan includes fewer direction changes. Needle motion uncertainty at locations of direction changes may be substantially higher than uncertainty during insertion due to transverse stiffness of the needle	89
5.7	The optimal needle insertion location y , angle θ , and bevel direction b are found by scanning the DP look-up table for the feasible start state with maximal P_s . Here we plot optimization surfaces for $b=0$. The low regions correspond to states from which the needle has high probability of colliding with an obstacle or exiting the workspace, and the high regions correspond to better start states	90
5.8	Three simulated image-guided needle insertion procedures from a fixed starting point with needle motion uncertainty standard deviations of $\sigma_i = 5^{\circ}$ during insertion and $\sigma_r = 20^{\circ}$ during direction changes. After each insertion distance δ , we assume the needle tip is localized in the image and identified using a dot. Based on the DP look-up table, the needle is either inserted (small dots) or a direction change is made (large dots). The effect of uncertainty can be seen as deflections in the path, i.e., locations where the tangent of the path abruptly changes. Since $\sigma_r > \sigma_i$, deflections are more likely to occur at points of direction change. In all cases, $P_s = 72.35\%$ at the initial state. In (c), multiple deflections and the nonholonomic constraint on needle motion prevent the needle from reaching the target	91
6.1	Transverse slice of a CT scan with white contours of the prostate (1), urethra (2), and rectum (3). The catheters are marked with black dots	94
6.2	The clinical criteria, plotted here for a typical prostate cancer case, are specified using cost functions which define penalty as a function of dose for each dose calculation point type	101
6.3	The percent difference in objective function value between the optimal solution (found using the LP method) and the solution found by SA for 20 prostate cancer patient cases. The difference is statistically significant $(P = 1.54 \times 10^{-7})$	106
6.4	Mean dosimetric index results for the SA and LP methods for 20 prostate cancer patient cases. Error bars indicate maximum and minimum values for the 20 patient cases	108
6.5	Dose-volume-histogram (DVH) plots for the prostate (a), urethra (b), rectum (c), and bladder (d) for the patient case with greatest difference in dosimetric indices between the LP and SA solutions. For dose less than D^{min} for each tissue type, the desired volume is 100%. For dose greater than D^{max} , the	
	desired volume 0%	109

List of Tables

3.1	DSC mean and standard deviation (in parentheses) for image registration quality.	55
3.2	Point displacement error means and standard deviations (in parentheses) for sample homologous points on the boundary of the prostate central gland and peripheral zone near the midline	55
6.1	Clinical criteria parameters for dose penalty cost functions for a typical prostate cancer case	100
6.2	HDR dose optimization LP formulation constants, variables, and functions.	102
6.3	Improvement of LP solutions over SA solutions for 20 prostate cancer patient cases calculated as the absolute difference in dosimetric index percent values. Negative values indicate deterioration in the dosimetric index. The significance P of the differences was computed using paired t -tests	107

Acknowledgements

I would like to thank my advisor, Professor Ken Goldberg, for his mentoring over the last 5 years. From his research insights to his tips on presenting results to the research community, his help and advice have been invaluable. I would also like to especially thank Jean Pouliot and Dr. Joe Hsu from the UCSF Department of Radiation Oncology for introducing me to key problems in medicine that can be tackled with computer science and engineering methods.

Thank you to my thesis and qualifier committee members, James O'Brien, Andrew Lim, and Alper Atamtürk, for their insights and advice that helped me improve my research methods and results.

I would like to thank my research collaborators at The Johns Hopkins University, especially Allison Okamura, Noah Cowan, Bob Webster, and Russ Taylor, for all their ideas and career advice. I would also like to thank my collaborators at UCSF, John Kurhanewicz, Etienne Lessard, Yongbok Kim, Sue Noworolski, and Richard Taschereau, for their help and for patiently introducing me to medical background necessary for my research.

I would like to thank current and former members of Ken Goldberg's Alpha Lab with whom I have discussed research over the years, including Dezhen Song, K. "Gopal" Gopalakrishnan, and Anthony Levandowski. I would also like to thank all the UC Berkeley undergraduate students who I have had the pleasure to work with, including Vijay Vasudevan, Michael Yu, Brian Sung Chul Choi, and Ryan Chen.

I would also like to thank members of the research community who have given me advice over the years, including Cenk Cavusoglu, Simon DiMaio, Frank Tendick, Frank van der Stappen, Steve LaValle, Ruzena Bajcsy, Kimmen Sjölander, and Tim Tong.



Chapter 1

Introduction

Exciting advances in medical imaging are enabling clinicians to noninvasively examine anatomy and metabolic processes deep below the skin's surface. From computed tomography capable of displaying the patient's 3-D anatomy with sub-millimeter resolution, to spectroscopy imaging that can identify the location of metabolic compounds in tissue, the quantity and detail of patient-specific imaging data available to clinicians is rapidly increasing. Combining this wealth of digital information with advances in computation power has the potential to significantly improve patient care. To fully realize this potential, new computational tools are needed to plan and optimize surgical and interventional medical procedures.

In this dissertation, we develop new algorithms for image-guided medical procedures. Our approach combines biomedical imaging, biomechanical modeling, and new geometric planning and optimization algorithms. This approach takes advantage of advances in robotics algorithms, finite element modeling, and operations research. Increases in computer processing speed are enabling the integration of results from these disparate fields in a novel fashion, allowing the creation and implementation of effective planning and optimization algorithms for image-guided medical procedures.

The input to these methods is digital imaging information. Molecular-scale imaging techniques such as Magnetic Resonance Spectroscopy Imaging (MRSI) enable physicians

to noninvasively and precisely identify the location of anomalies such as cancerous lesions. Computed Tomography (CT) can display the patient's 3-D anatomy with a resolution as fine as 0.5 mm. Ultrasound imaging can display moving tissues in real-time. And X-ray fluoroscopy can image and localize medical devices such as needles inside human tissue. These imaging modalities can be used in combination with traditional surgical tools as well as new devices such as flexible needles that can be steered through soft tissues to targets deep below the skin surface. However, these imaging modalities and surgical tools are each subject to their own set of physical constraints, which must be considered during procedure planning and optimization.

A challenge clinicians commonly face is compensating for errors caused by soft tissue deformations that occur when imaging devices or surgical tools, such as needles, physically contact soft tissue. We develop computational models and simulations of soft tissue deformation using finite element methods (FEM). Although FEM is generally used for off-line simulation of stiff solid materials, we harness the power of modern computers to perform real-time FEM simulation of soft tissues. We demonstrate how these simulations can be used as a component of higher-level planning algorithms, such as image registration algorithms to map targets across images and motion planning algorithms to compensate for errors caused by tissue deformations during needle insertion. We also develop algorithms that explicitly consider uncertainty in the response of a surgical tool due to patient variability and the complexity of tool/tissue interaction. Throughout this dissertation, we emphasize statistical analysis and theoretical guarantees for algorithm performance.

In figure 1.1, we illustrate our proposed information flow for computer-assisted image-guided medical procedures. Between the traditional image acquisition and treatment phases, a computational phase incorporates new algorithms to plan and optimize the procedure. Developing these computational tools is the focus of this dissertation. We develop a physically based simulation algorithm using a finite element method and develop planning and optimization algorithms based on nonlinear optimization, dynamic programming, and linear programming.

Our results can apply to a variety of medical applications, from biopsies to anesthesia

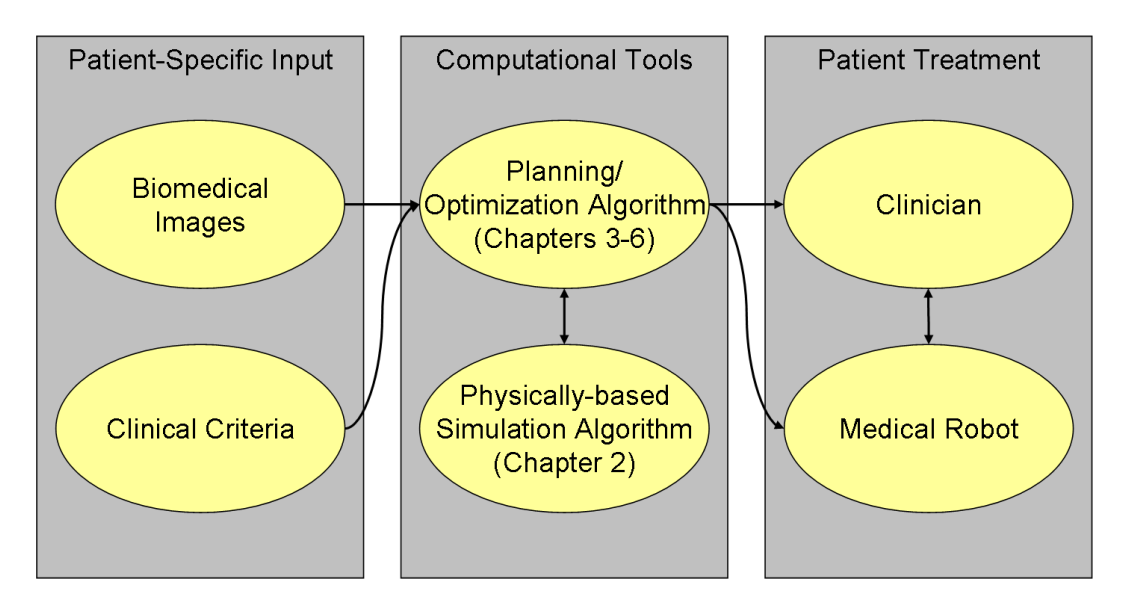
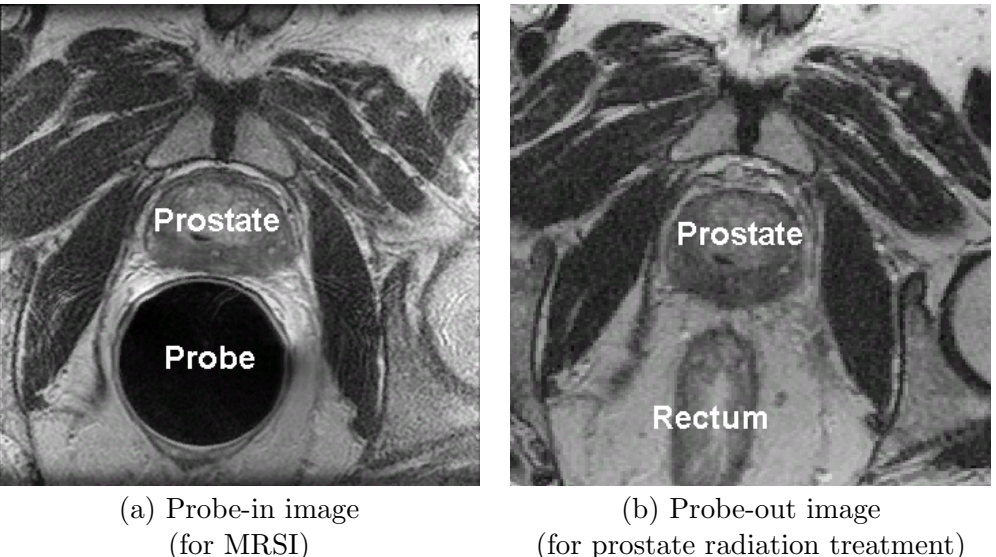


Figure 1.1. Information flow for computer-assisted image-guided medical procedures. In this dissertation, we focus on developing computational tools: planning/optimization algorithms and physically-based simulation algorithms.

injections to radiation cancer treatment. In this dissertation, we emphasize the application to prostate brachytherapy, a medical procedure for treating prostate cancer in which physicians use needles to place radioactive seeds in close proximity to cancerous cells.

1.1 Planning and Optimization Algorithms

We focus on four planning and optimization problems: target localization in deformable tissues, motion planning for rigid needles in deformable tissue, motion planning for steerable needles, and dose optimization for brachytherapy cancer treatment. Each of these problems introduces new computational challenges and is subject to unique planning and optimization constraints imposed by the physician's treatment requirements, the patient's anatomy, and the physical limitations of medical equipment and devices. We present planning and optimization algorithms for each of these general problems, and then customize the solution to the specific application of prostate brachytherapy.



(for prostate radiation treatment)

Figure 1.2. MRSI data for the prostate is obtained with a balloon endorectal probe, as shown in an axial MR image at the mid-gland of the prostate (a). Radiation treatment is performed with the probe removed (b). The balloon endorectal probe causes substantial deformation of the prostate.

1.1.1 Target Localization in Deformable Tissues

Recent advances in MR Spectroscopic Imaging (MRSI) are enabling physicians to noninvasively pinpoint the location of cancerous cells inside the body by measuring concentrations of metabolic compounds correlated with cancer [94]. But to obtain a sufficient signal-to-noise ratio for MRSI, a probe must be placed close to the organ of interest, which often results in substantial deformations of the surrounding soft tissues, as shown in figure 1.2. We develop an image registration algorithm that explicitly considers soft tissue deformations using a finite element model and estimates uncertain tissue parameters using nonlinear optimization. We apply the method to register diagnostic MRSI prostate images with radiation treatment planning images in which the probe is removed. Results for 10 prostate cancer patient cases indicate a statistically significant improvement over past methods [9].

1.1.2 Motion Planning for Rigid Needles in Deformable Tissue

With the increasing use of minimally invasive image-guided medical interventions, needle insertion is becoming ubiquitous in modern medical procedures, from biopsies to anesthesia injections to cancer treatments such as cryotherapy and brachytherapy. Accurately guiding a needle to a specific target inside the human body is crucial for the success of these procedures. However, significant errors are common in current practice due to deformation of soft tissue caused by forces exerted on the tissue by the needle during insertion. We design and implement a software simulation that models the biomechanical tissue deformations that occur during needle insertion. We then develop a motion planning algorithm to compensate for errors caused by soft tissue deformation by combining efficient finite element models with an optimization algorithm for needle entry location and insertion depth. We apply the planner to an example from prostate brachytherapy [16], where the success of the procedure depends on the accurate placement of radioactive seeds within the prostate gland [46, 131] and ignoring these deformations can result in misplaced seeds [134, 131].

1.1.3 Motion Planning for Steerable Needles

With researchers from The Johns Hopkins University, we are developing a new class of highly flexible bevel-tip medical needles (patent pending) that can be steered to targets in soft tissue previously inaccessible to rigid needles [160]. Needle steering can be viewed as a type of nonholonomic motion planning for a car-like mobile robot. We develop a motion planning algorithm for steerable needles to avoid obstacles and account for needle motion uncertainty due to patient variability and the complexity of needle/tissue interaction. The planner models uncertainty in needle motion using a Markov Decision Process and solves for an optimal plan using infinite horizon dynamic programming. Using simulation, we show that accounting for needle motion uncertainty during planning can significantly increase the probability of reaching targets without colliding with obstacles [5].

1.1.4 Dose Optimization for Brachytherapy Cancer Treatment

Using medical images of patient anatomy and estimates of tumor location, physicians prescribe radiation dose requirements for cancerous tumors and surrounding tissues. We re-introduce linear programming into dose optimization by developing a fast and exact method to compute radioactive source locations and dwell times to maximize satisfaction of physician specified dose constraints for high-dose-rate brachytherapy cancer treatment. The method uses the objective and clinical criteria framework of Inverse Planning by Simulated Annealing (IPSA), an approach developed at the University of California, San Francisco (UCSF) that has been used in the treatment of over a thousand patients. We applied the method to 20 prostate cancer patient cases [12]. Unlike previous methods used for dose optimization, our new LP method guarantees a mathematically optimal solution.

1.2 Brachytherapy for Treating Prostate Cancer

In this dissertation, we demonstrate our methods on the specific application of prostate cancer treatment. Prostate cancer kills over 30,000 Americans each year [120]. It is the second leading cause of cancer death for men in the United States (after lung cancer). One in six American men will be diagnosed with prostate cancer during their lifetime, and someone will die from it approximately every 18 minutes [83]. By applying new planning and optimization algorithms to the treatment of this disease, this dissertation takes steps toward addressing the question: how can computation help improve patient care?

The prostate is roughly the size of a walnut. It is shaped like a pyramid, with average transverse \times anteroposterior \times craniocaudal dimensions of 4 cm \times 3 cm \times 3 cm \times 3 cm [34, 88]. The prostate is located inferior to the bladder and anterior to the rectum and surrounds the urethra, as shown in figure 1.3.

Brachytherapy, a minimally invasive medical procedure in which physicians place radioactive seeds in close proximity to cancerous tumors, is increasingly being used clinically to treat prostate cancer because it can be used to deliver a high dose to the cancerous

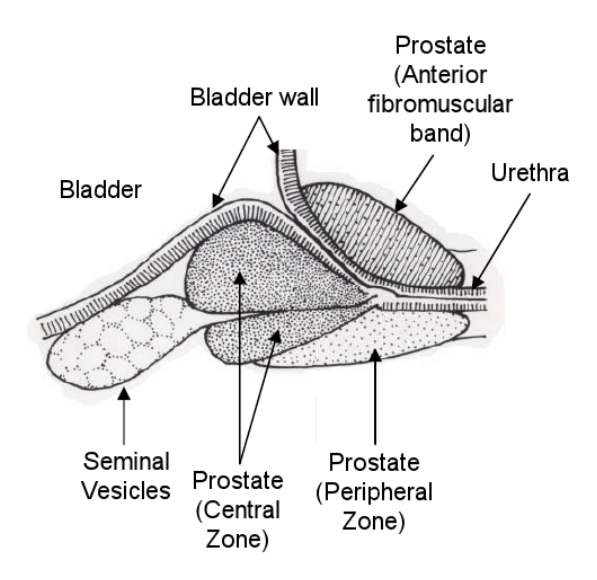


Figure 1.3. The prostate, shown here in the sagittal plane, consists of multiple zones, including the anterior fibromuscular band, the central zone, and the peripheral zone [88, 40]. In this figure, the cranial direction is to the left.

tumor and a low dose to surrounding healthy tissue. The radioactive seeds, approximately 4 mm long and 0.8 mm in diameter, are guided to their destination using hollow medical needles. Using medical images, the physician prescribes radiation doses for the prostate and surrounding tissues. The radioactive dose delivered by the seeds should "conform" to the physician specified prescriptions over the patient anatomy. Past studies indicate that improving radiation dose conformality improves patient health and reduces normal tissue complication rates [154, 80, 93].

Two variants of prostate brachytherapy are commonly used in medical practice: Low Dose Rate (LDR) and High Dose Rate (HDR). LDR brachytherapy is typically referred to as permanent seed brachytherapy. Because the response of cancer cells to radiation depends on dose rate, the variant of the procedure that is selected for a particular patient depends on the location and stage of the prostate cancer and other medical considerations [117].

In permanent seed brachytherapy, physicians use needles to permanently implant low dose rate radioactive seeds inside the prostate, which will irradiate the prostate and surrounding tissue over several months. Prior to implantation, a CT or MR image is obtained of the patient anatomy and a dosimetric plan is prepared that specifies seed locations in-

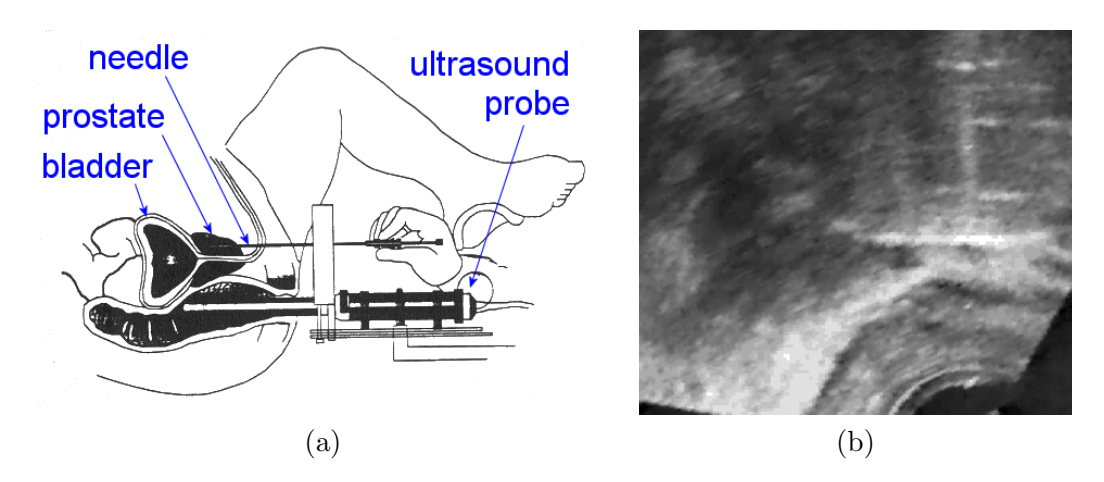


Figure 1.4. During permanent seed brachytherapy (a), needles carrying radioactive seeds are inserted transperineally into the patient, who is lying on his back [131]. The quality of intra-operative transrectal ultrasound images is very poor (b), making it difficult to track the penetration of the needle into the deformed prostate.

side the prostate that satisfy physician specified dose requirements, such as a minimum peripheral dose coverage, a uniform dose distribution inside the prostate gland, protection of the urethra, and a dose boost to the tumor. Approximately 100 seeds and biodegradable spacers are loaded into 20 to 25 needles. The physician inserts each needle transperineally into the patient, who is lying on his back as shown in figure 1.4. Seeds and spacers are pushed out of the needle when the depth of the needle specified by the dosimetric plan is reached. Achieving the desired seed placement is left to the physician, who must take into account factors such as needle bending and tissue deformations during the implant process [46, 134, 131].

In High Dose Rate (HDR) brachytherapy, physicians insert catheters into the prostate through the perineum under ultrasound guidance in the operating room. Approximately 18 catheters are required to offer sufficient dwell time positions to cover the entire prostate. A CT or MR image is then obtained of the patient anatomy and the physician prescribes dose requirements for each point in the prostate and surrounding tissues. A plan is then created which specifies seed dwell positions and dwell times that satisfy the physician prescribed dose requirements. To execute the plan, the catheters are attached to a robot (such as a Nucletron MicroSelectron High Dose Rate Remote Afterloader) for treatment delivery. The robot moves a single radioactive source inside each catheter to each dwell position for the

pre-computed dwell times [108]. This procedure may be repeated before the catheters are removed.

1.3 Contributions

The main contributions of this dissertation are new algorithms that computationally plan and optimize image-guided medical procedures based on physician-specified clinical criteria. With the exception of motion planning for steerable needles, which have not yet been approved by the U.S. Food and Drug Administration (FDA) for human trials, all algorithms developed in this dissertation have been tested with data from human patients based on clinical medical images. In this research, we:

- Identified and implemented appropriate models and algorithms to interactively estimate soft tissue deformations due to forces applied during surgical and interventional medical procedures. The software tools integrate methods from real-time physically-based modeling in computer graphics and classical finite element modeling.
- Developed a 2-D simulation of medical needle insertion. The simulation estimates tissue deformations using a finite element model and real-time mesh maintenance.
- Designed and implemented a 2-D deformable image registration method that explicitly
 considers tissue deformations when mapping targets between images. Results using
 prostate medical images indicate a statistically significant improvement in registration
 accuracy compared to previous methods.
- Designed and implemented a motion planning algorithm for traditional stiff needle insertion procedures to correct for errors caused by predicted soft tissue deformations.
 The method combines a finite element model of needle insertion in soft tissue with numeric optimization.
- Developing a new class of *steerable* needles with researchers from The Johns Hopkins University. The needles have two features enabling steering: a bevel-tip that exerts

asymmetric forces on the surrounding soft tissue, and high flexibility causing the needles to bend in the direction of their bevel. The new needles can be steered to targets in soft tissue previously inaccessible to stiff needles.

- Designed and implemented a motion planning algorithm that explicitly considers uncertainty in motion for nonholonomic mobile robots subject to a constant turning radius, and applied the planner to steerable needles. The algorithm combines geometric planning with Markov Decision Processes and Dynamic Programming. Results indicate that traditional shortest paths do not maximize the probability of successfully acquiring the target when the needle's response to controls is not known with certainty.
- Formulated the HDR brachytherapy dose optimization problem as a linear program, enabling the fast computation of mathematically optimal solutions. The linear program uses the objective and clinical criteria framework developed at the University of California, San Francisco (UCSF) and maximizes satisfaction of physician specified dose prescriptions.
- Used the optimal HDR brachytherapy solutions obtained by our linear program as
 a baseline to statistically validate the optimization performance of current clinical
 software that has been used in the treatment of over a thousand cancer patients
 internationally and is based on the probabilistic optimization method of simulated
 annealing.

1.4 Dissertation Overview

In Chapters 2 through 6, we introduce new computational tools for computer-assisted image-guided medical procedures, as illustrated in figure 1.1. In Chapter 2, we present biomechanical models of soft tissue and develop a simulation of soft tissue deformation based on a finite element method. This simulation tool will serve as a building-block for the planning and optimization algorithms presented in subsequent chapters. In Chapter

3, we develop an image registration algorithm to automatically map targets identified in one image to their corresponding locations in another image in which the soft tissues have deformed. The method simulates soft tissue deformation and estimates uncertain tissue parameters to significantly improve registration quality compared to previous methods. We then present new motion planning algorithms to guide needles to desired targets. In Chapter 4 we present the first motion planning algorithm, designed for traditional rigid needles, which compensates for predicted tissue deformations caused by needle insertion. The method combines a finite element model of soft tissue from Chapter 2 with numerical optimization. The second algorithm, presented in Chapter 5, considers motion planning for a new class of needles: steerable needles that can bend around obstacles to reach targets inaccessible to traditional rigid needles. Our motion planning algorithm explicitly considers uncertainty in the steerable needle's response to controls; it efficiently samples the state space and formulates the planning problem as a Markov Decision Process, which can be solved in polynomial time using dynamic programming, to maximize the probability that the needle will successfully reach the target. In Chapter 6, we develop a method based on linear programming to optimize radioactive source locations and dwell times for highdose-rate brachytherapy prostate cancer treatment. Finally, in Chapter 7, we conclude and suggest new research directions where the combination of imaging data, biomechanical modeling, and planning and optimization algorithms can potentially improve patient care.

Chapter 2

Biomechanical Modeling and Simulation of Soft Tissue Deformations

Human surgery is increasingly based on minimally invasive procedures that operate inside the body through narrow openings, reducing disturbance to healthy tissue, minimizing risk of infection, and speeding recovery. However, reduced visual and tactile feedback for the physician can make these procedures more difficult to perform than traditional open surgical procedures. Fast and accurate computer simulations of these procedures can facilitate physician training and assist in pre-operative planning and optimization.

Surgery simulation creates a virtual environment in which a physician can interact with organs and tissues that are simulated on a computer. Simulations are being developed for a wide array of medical procedures, including laparoscopic surgery [142], bronchoscopy [29], and endoscopic surgery [18]. Surgery simulation aims to complement the traditional apprenticeship model of physician training; physicians can train in a controlled environment that exposes them to both common and rare cases and can practice new techniques without risks to patient safety. Studies indicate that surgical skills learned using computational simulators directly improve operating room performance by significantly decreasing procedure

time and reducing the number of medical errors [142, 137, 65]. In one videotaped study on gallbladder dissection, physicians trained using surgery simulation performed the task 29% faster and with six times fewer errors compared to traditional training [142].

In addition to training, surgery simulation can also be applied to medical procedure planning. With patient-specific imaging data and a sufficiently realistic simulation of a procedure including the surgical tools and tissue, a planner can search the space of possible tissue/tool interaction sequences to identify a plan that is best suited to accomplish the clinical objectives. The ultimate goal is to provide a pre-operative plan, integrated with medical imaging, to the physician or robotic hardware that will perform that procedure [135, 152, 136].

Just as flight simulators give pilots an opportunity to learn and practice flying in a variety of visibility and weather conditions, surgery simulators aim to allow physicians to perform a procedure "virtually" on a computer to practice on difficult patient cases without risking patient safety. But whereas flight simulation requires models of airflow and rigid objects such as the plane, landforms, and buildings, the key challenge in surgery simulation is simulating deformable tissue interactively. Accurately simulating and displaying tissue deformations and tool-tissue interactions in real-time poses a computationally challenging problem and is the topic of much current research.

In this chapter, we combine methods from classical finite element methods with recent approaches from computer graphics to create a real-time interactive simulation with sufficient accuracy to warrant further investigation for clinical applications. We focus on medical procedures that involve needle insertion. Needle insertion is a key component of many image-guided minimally invasive medical interventions, such as biopsies or cancer treatments such as thermal ablation, cryotherapy, and brachytherapy. Accurately guiding a needle to a specific target inside the human body is crucial for the success of these procedures. However, significant errors are common in current practice due to soft tissue deformation and human variability.

Consider the application of permanent seed prostate brachytherapy, a minimally invasive

medical procedure in which physicians use needles to permanently implant seeds inside the prostate that irradiate surrounding tissue over several months. The success of this procedure depends on the accurate placement of radioactive seeds within the prostate gland [46, 131]. Unfortunately, inserting and retracting needles causes the surrounding soft tissues to displace and deform: ignoring these deformations during the implantation contributes to seed misplacement [134, 131, 149]. Physicians must therefore learn to compensate for these effects in an attempt to implant the seeds accurately in the prostate at the pre-planned positions. A dynamic simulation can facilitate physician training and procedure planning by allowing a physician or optimizing planner to determine how physician-controlled and patient-specific parameters will affect seed placement.

In this chapter, we first provide background on simulation of deformable objects before presenting our simulation of medical needle insertion. In section 2.1, we provide an introduction to continuum mechanics, a mathematical framework that has successfully been used to characterize living tissues and their deformations under applied forces. We then discuss research on soft tissue simulation in section 2.2. We then present our key contribution: the development of a simulation of medical needle insertion. The simulation incorporates a biomechanical model of needle/tissue interaction using a finite element method and mesh modification. The method displays the deforming tissue using texture-mapping. This simulation will serve as a building block for the planners in Chapter 3 and Chapter 4.

2.1 Fundamentals of Continuum Mechanics

Continuum mechanics aims to describe the effect of external forces or disturbances on the global behavior of solids, liquids, and gases. The theory behind continuum mechanics was originally developed in the early nineteenth century by Claude-Louis Navier, Siméon Denis Poisson, and George Green [162]. It has since been successfully applied in numerous domains, from airplane design to bridge construction to nanotechnology. Since living tissue is composed of discrete cells, which in turn are composed of molecules and atoms, living tissue is not an ideal continuous material. However, the approximation of a continuous material.

uous material is reasonable for many living tissues; a large class of living tissues has been successfully characterized using the language of continuum mechanics [63, 92, 33, 31].

In continuum mechanics, we assume that field quantities such as the densities of mass, velocity, and energy are continuous over time and space inside the material [64]. We will consider a *deformable body*, a continuous material within a closed surface. We can use continuum mechanics to study how such a deformable body behaves when it is subjected to external influences such as forces or temperature changes.

In this section, will describe the fundamentals of continuum mechanics. We start by formally defining a deformable body. We then introduce the basic concepts of continuum mechanics using a simple 1-D example, and then generalize to 3-D and 2-D deformable bodies. We will use the framework of continuum mechanics to compare and analyze methods for simulating soft tissue deformations in section 2.2.

2.1.1 Deformable Bodies

We consider a deformable body B, a continuous material within a closed surface, which is a subset of the space \Re^n where $n \in \{1, 2, 3\}$. The deformable body is composed of a set of material points $\mathbf{p} \in B$. The initial geometry of the deformable body is its reference state.

External forces applied to a deformable body B may cause material points $\mathbf{p} \in B$ to move, resulting in a deformed body B'. B' specifies the geometry of the deformed state of the deformable body.

The displacement of a material point is its position change from B to B'. We define the transformation of a body B to a deformed state B' by a displacement field, which specifies the displacement for each material point in B, as shown in figure 2.1. Each point $\mathbf{p} \in \beta$ is transformed to a new point $\mathbf{p}' \in B'$ such that $\mathbf{p}' = \mathbf{p} + u(\mathbf{p})$, where $u(\mathbf{p})$ specifies the displacement field for each $\mathbf{p} \in B$. In continuum mechanics, we assume the mapping u that transforms B to B' is single valued, continuous, and has a unique inverse [64].

In dynamic simulations of deformable bodies, the displacement field $u(\mathbf{p})$ is a function of time. At all times, the displacement field is defined with respect to the original reference

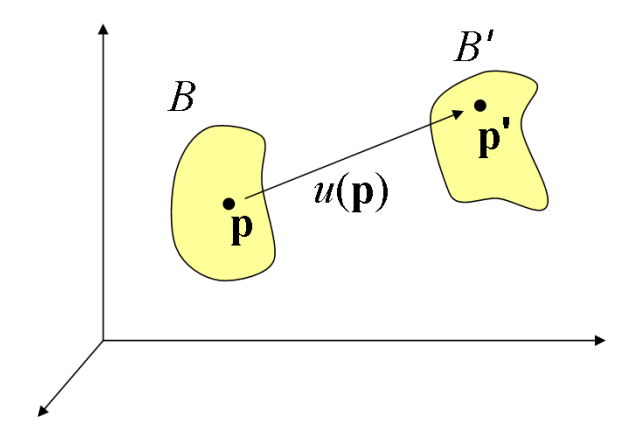


Figure 2.1. A deformable body B in its reference state is deformed to B' by displacement field u.

state. We define coordinates for points in the reference state in the material coordinate frame. The coordinates of displaced points during the simulation are defined in the world coordinate frame.

2.1.2 The 1-D Case

We introduce fundamental concepts from continuum mechanics with a simple 1-D example, a bar constrained along the x-axis. As illustrated in figure 2.2(a), the bar is fixed (i.e., attached to a wall) on the left at x = 0. At rest, the bar has length L. When a force f is applied to the bar along its axis, the bar will deform. If f points along the positive x-axis, the bar extends by a distance Δ , as shown in figure 2.2(b).

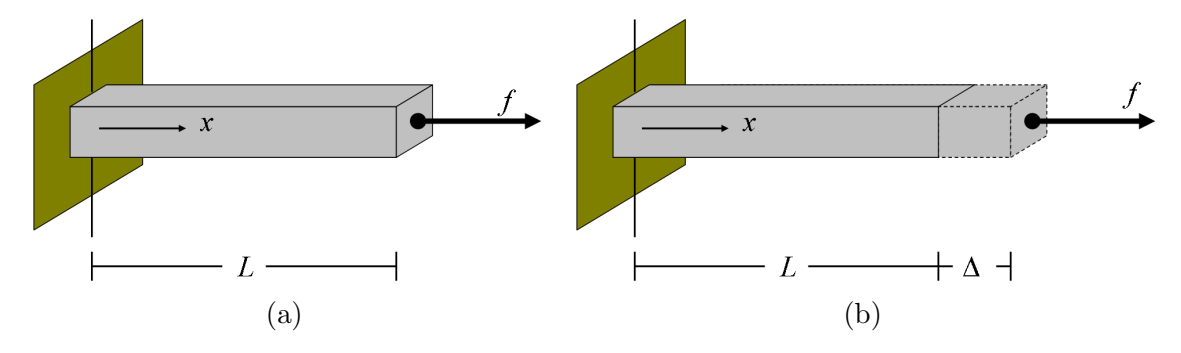


Figure 2.2. A 1-D bar of length L in the reference state (a). Due to force f, the bar extends to length $L + \Delta$ in the deformed state.

Stress is a measurement of force intensity: the total force acting on a surface divided

by the area of that surface. Unlike force, which is a global quantity acting on the entire deformable body, stress is defined pointwise. In the 1-D bar example, stress σ at point x is defined by

$$\sigma(x) = \frac{f}{A},$$

where A is the (infinitesimal) cross-sectional area of the bar. Stress has units force per unit area. In the SI measurement system, stress has units of Pascals (Pa), which is a derived unit for Newtons per square meter.

Stress may result in a deformation of the deformable body. *Deformation* is measured as relative displacement, or

$$u(x + \Delta x) - u(x)$$
.

Strain is a measurement of relative deformation at a point. For a point x on a 1-D bar, strain ϵ is the ratio between the change in length of a segment (of infinitesimal length about x) and the original length of the segment:

$$\epsilon(x) = \frac{u(x + \Delta x) - u(x)}{\Delta x}.$$

In the limit as $\Delta x \to 0$,

$$\epsilon(x) = \frac{du}{dx}.$$

Strain has units of length per unit length, which is effectively unitless.

The relationship between stress and strain depends on the underlying material of the deformable body. We mathematically represent this relationship using a *constitutive relation*. In general, the constitutive relation is determined through physical experiments [63]. When the relation between stress and strain is linear, the material is linearly elastic and

$$\sigma = E\epsilon$$
,

where E is the Young's modulus, a property of the material [64]. This relation is often referred to as Hooke's Law.

Given the geometry of the 1-D deformable body, the constitutive relation of the material, and the external applied forces, we can compute the resulting displacement field for the deformable body. We accomplish this by defining the stress resulting from the applied forces, computing the strain by plugging the stress into the constitutive relation, and integrating over the volume of the deformable body. For the 1-D bar example where the bar is composed of a linearly elastic material, the elongation Δ of the bar is computed by integrating strain over the length of the bar:

$$\Delta = \int_0^L \frac{du}{dx} dx = \int_0^L \epsilon(x) dx = \int_0^L \frac{\sigma(x)}{E} dx = \int_0^L \frac{f}{AE} dx = f \frac{L}{AE}.$$
 (2.1)

The quantity

$$k = \frac{f}{\Delta} = \frac{AE}{L}$$

is the *stiffness* of the bar. In 1-D, stiffness is a function of the Young's modulus and the geometry of the bar. For a linearly elastic material,

$$f = k\Delta$$
.

Stiffness represents the amount of force required to achieve a unit displacement.

2.1.3 The 3-D Case

In 3-D, the relationships between stress, strain, and the constitutive relation are equivalent to the 1-D case. However, stress and strain are represented by tensors with 6 degrees of freedom rather than by scalars. Detailed derivations of the formulas for these tensors are available in standard continuum mechanics texts [64]. Here we focus on the fundamentals that will be applicable to soft tissue simulation in section 2.2.

To define stress at a point in 3-D, we consider an infinitesimal cube centered about the point. We illustrate the 9 components of stress at a point in 3-D in figure 2.3. Stress σ is defined by a 3 × 3 tensor

$$\sigma = \left[\begin{array}{ccc} \sigma_{11} & \sigma_{12} & \sigma_{13} \\ \\ \sigma_{21} & \sigma_{22} & \sigma_{23} \\ \\ \sigma_{31} & \sigma_{32} & \sigma_{33} \end{array} \right],$$

where indices 1, 2, and 3 correspond to the x, y, and z axes, respectively. The elements along the diagonal are the *normal* stress components, while the off-diagonal elements are the *shear* stress components. The stress tensor is symmetric, resulting in 6 unique components [64].

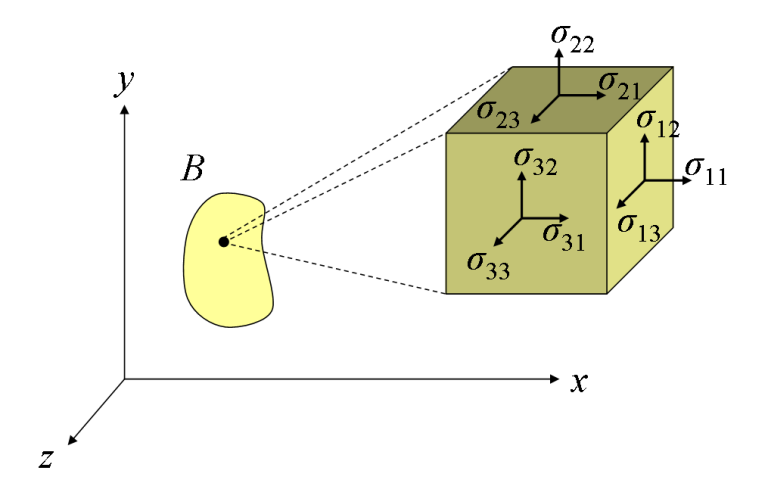


Figure 2.3. The components of the stress tensor σ in 3-D for an infinitesimal cube from a deformable body B.

Strain in 3-D is also defined by a 3×3 symmetric matrix with 6 unique components [64]:

$$\epsilon = \begin{bmatrix} \epsilon_{11} & \epsilon_{12} & \epsilon_{13} \\ \epsilon_{21} & \epsilon_{22} & \epsilon_{23} \\ \epsilon_{31} & \epsilon_{32} & \epsilon_{33} \end{bmatrix}.$$

Given the point-wise displacement field u for the deformable body, strain in 3-D can be computed similarly to 1-D by measuring the change in length of an infinitesimal segment. For a point \mathbf{p} with displacement $\mathbf{u} = u(\mathbf{p})$, strain is a quadratic function:

$$\epsilon_{11} = \frac{\partial u_1}{\partial p_1} + \frac{1}{2} \left[\left(\frac{\partial u_1}{\partial p_1} \right)^2 + \left(\frac{\partial u_2}{\partial p_1} \right)^2 + \left(\frac{\partial u_3}{\partial p_1} \right)^2 \right]$$
 (2.2)

and

$$\epsilon_{12} = \frac{\partial u_1}{\partial p_2} + \frac{\partial u_2}{\partial p_1} + \left[\frac{\partial u_1}{\partial p_1} \frac{\partial u_1}{\partial p_2} + \frac{\partial u_2}{\partial p_1} \frac{\partial u_2}{\partial p_2} + \frac{\partial u_3}{\partial p_1} \frac{\partial u_3}{\partial p_2} \right]$$
(2.3)

and similarly for the other strain components. Although quadratic strain is necessary to accurately model large rotations [172], higher order strain terms are often dropped to define the simpler "geometrically linear" strain:

$$\epsilon_{11} = \frac{\partial u_1}{\partial p_1} \tag{2.4}$$

$$\epsilon_{12} = \frac{\partial u_1}{\partial p_2} + \frac{\partial u_2}{\partial p_1} \tag{2.5}$$

which is applicable to smaller deformations without large rotations.

Once an appropriate representation of strain is selected, we can relate stress to strain using a constitutive relation that is appropriate for the material composing the deformable body. For a linearly elastic material,

$$\sigma_{ij} = \sum_{k=1}^{3} \sum_{l=1}^{3} C_{ijkl} \epsilon_{kl}$$

where \mathbf{C} is a tensor of 81 elastic coefficients. For isotropic materials, tensor \mathbf{C} can be derived from only two independent values: the Young's modulus E and Poisson's ratio ν . The constitutive relation in 3-D for isotropic linearly elastic materials is:

$$\sigma_{ij} = \sum_{k=1}^{3} \left(\frac{E\nu}{(1-2\nu)(1+\nu)} \right) \epsilon_{kk} \delta_{ij} + 2 \left(\frac{E}{2(1+\nu)} \right) \epsilon_{ij}$$

where δ_{ij} is the Kronecker delta function:

$$\delta_{ij} = \begin{cases} 1 & : i = j \\ 0 & : i \neq j \end{cases}.$$

As in the 1-D case, the Young's modulus is a measure of the stiffness of a material. Poisson's ratio is a measure of compressibility; when an object is stretched, Poisson's ratio quantifies the object's tendency to become thinner. In nonlinear methods such as Kelvin-Voigt, the tensor \mathbf{C} can be functions of strain ϵ and strain rate $\dot{\epsilon}$ [64, 173].

Given the relationship between stress and strain, in 1-D we were able in equation 2.1 to obtain an analytic closed-form expression for the displacement of a point on the bar due to an external force by integrating over the volume of the bar. In higher dimensions, obtaining an analytic expression relating displacement to external forces is not possible, except for a small number of geometrically simple problems. To compute displacements for geometrically complicated deformable bodies, numerous methods have been developed to numerically compute approximate solutions, including mass-spring methods [35], boundary element methods [82], finite difference methods [35], and finite element methods [173]. In section 2.2, we focus on methods applicable to soft tissue deformations.

2.1.4 The 2-D Case

For certain problems, the stress and strain tensors defined for 3-D analysis can be simplified for 2-D analysis. One common approximation is plane strain, in which we assume $\epsilon_{33} = \epsilon_{23} = \epsilon_{31} = 0$. This assumption is valid when the object does not substantially displace or deform in the z-direction, which commonly occurs when the z-direction dimension of the body is large or restrained from motion. In 2-D surgery simulation, plane strain is appropriate if the tissue does not deform normal to the selected imaging plane.

2.2 Simulating Soft Tissue Deformations

Simulation of surgical and interventional medical procedures such as needle insertion requires estimating biomechanical deformations of soft tissue when forces are applied. Because of the complicated geometry of tissue and the wide array of possible forces that can be applied by surgical instruments, closed form solutions for soft tissue displacement fields cannot be computed in general.

Historically, several methods have been developed for discretizing tissue into smaller elements for which the equations of continuum mechanics can be directly applied, and then numerically combining solutions from the discrete chunks into a global solution to obtain a tissue displacement field. The history of offline animation and real-time simulation of deformable objects is summarized in [68]. Here we discuss the mass-spring method and finite element methods, both of which are capable of simulating deformable bodies with complicated geometries and composed of heterogeneous materials.

2.2.1 Mass-Spring Method

Mass-spring methods have been common for simulating a diverse array of human tissues including muscles [156] and blood vessels [32]. In this method, the tissue is defined using a discrete set of virtual point masses, or nodes, that represent the tissue volume. Because each node represents a small volume of tissue around it, this approach is sometimes referred

to as the lumped element model (LEM) [35]. Adjacent nodes are connected by massless linear response springs to form a 2-D or 3-D linkage of springs, as shown in figure 2.4. The dynamics of a node j in the mass-spring model is governed by $\mathbf{F}_j = \mu_j \mathbf{a}_j$, where \mathbf{a}_j is the acceleration of node j, μ_j is the mass of node j, and \mathbf{F}_j is the force applied to node j, which includes external forces and internal forces based on spring compression or extension. Viscous forces can also be added. Standard explicit or implicit time integration methods can be used to compute velocity and position of each node j from acceleration for each time step of the simulation [21]. Mass-spring models are relatively easy to implement. However, the arrangement of 1-D springs to define a 2-D or 3-D object has a significant impact on the deformation behavior of the object making it difficult to restrict volume changes or to model isotropic (or pre-defined anisotropic) material properties. Furthermore, there is no direct connection between spring stiffness coefficients and the Young's modulus and Poisson's ratio of continuum mechanics.

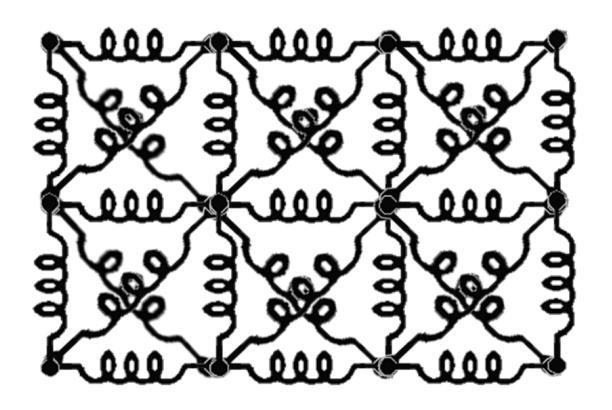


Figure 2.4. A regular mass-spring mesh for a 2-D object. The horizontal and vertical springs resist compression or tension while the diagonal springs are required to resist pure shear strains.

2.2.2 Finite Element Method

The development of the finite element method (FEM) can be traced back to the early 1940's, including key contributions by Alexander Hrennikof and Richard Courant. Finite element methods have been used extensively in the mechanical engineering community to model stiff materials. Unlike the mass-spring method, the finite element method is directly

based on the equations of continuum mechanics. The feasibility and potential of using a finite element approach for computer animation was demonstrated by Terzopolous et al. [153], and Stéphane Cotin et al. made early contributions to finite element modeling for surgery simulation [42].

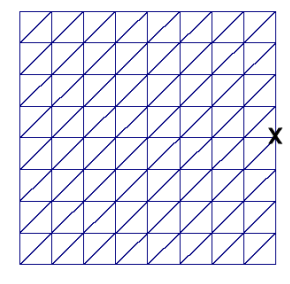
Details on the finite element method are available in standard texts [173]. The first step of the finite element method is to subdivide the deformable body into a finite set of elements. These elements correspond to a geometric discretization of the object. Fields quantities, like displacement, velocity, or acceleration, can be interpolated within each element using *shape functions* specific to the element shape. Finally, the equations of continuum mechanics can be applied to numerically solve for the interactions between the elements.

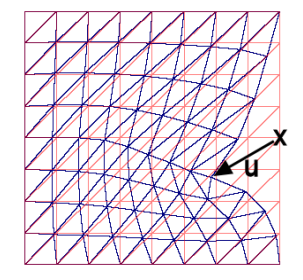
Geometric Discretization

In FEM, a deformable object is decomposed into a mesh of simple elements, generally triangles or quadrilaterals in 2-D or tetrahedra or hexahedra in 3-D. An extreme point of any element is called a node.

The reference mesh G defines the geometry of the deformable object in its reference state, where G is composed using n nodes and m elements. Each node's coordinate is stored in the node coordinate vector \mathbf{x} . In 2-D, \mathbf{x} is of dimension d=2n and each node has 2 displacement degrees of freedom (DOF). A deformation is defined by a displacement vector \mathbf{u} , which specifies the displacement of each node in mesh G. The deformed mesh G' is constructed in the world frame using the displaced node coordinates $\mathbf{x}' = \mathbf{x} + \mathbf{u}$, as shown in figure 2.5.

In continuum mechanics, boundary conditions specify constraints on the deformation of a deformable body. Boundary conditions can be applied at any nodes in the finite element mesh. These include displacement constraints (such as marking a node as fixed, like a node inside a bone) and external forces (due to tool/tissue interactions, like needle insertion). We define external forces in an external forces vector \mathbf{f} , with dimension 2n in 2-D, where each entry corresponds to a displacement degree of freedom in \mathbf{x} .





- (a) Finite element mesh G
- (b) Deformed finite element mesh G'

Figure 2.5. A 2-D finite element reference mesh G composed of triangular elements is shown in (a). The deformed mesh G' is shown in (b). The node labeled with \times in mesh G is displaced by vector \mathbf{u} in deformed mesh G'.

Interpolation

In continuum mechanics, field quantities such as displacement, velocity, acceleration, and mass density are continuous over the deformable body. Given values for these quantities at n discrete nodes in a finite element mesh, we use *shape functions* (also known as *basis functions*) to interpolate the value of these quantities at any point in the deformable body. Since adjacent elements share common nodes, the field quantities will be continuous over the entire deformable body defined by the mesh. In section 2.3, we use linear shape functions within each element, which can be derived using barycentric coordinates [122].

Solving System of Equations

Using a geometric discretization and shape functions, the finite element method provides a framework for calculating the internal stress distribution of elements in the mesh [173]. More specifically, given a vector of external forces acting on nodes of the deformable body, we can compute a vector of node displacements such that the internal forces generated by element stresses balances the external forces.

A simulation computes displacement \mathbf{u}_i as a function of time step i as external forces \mathbf{f}_i change over time. In this discussion, we initially assume the deformable body does not undergo large deformations or rotations and assume a linear relationship between stress and strain (Cauchy strain).

Linear Quasi-static Formulation The static formulation minimizes the total strain energy over the deformable body to compute its static equilibrium state [173]. Using the finite element method, deformation \mathbf{u}_i at time step i is computed using the formula

$$\mathbf{K}\mathbf{u}_i = \mathbf{f}_i$$

where \mathbf{u}_i is the nodal displacement vector, \mathbf{f}_i is the force displacement vector, and \mathbf{K} is the stiffness matrix based on the material properties of the elements in the mesh defining the deformable object. A quasi-static simulation assumes the deformable object reaches its equilibrium state at each time step.

Real-time visual performance for surgery simulation of the human liver using linear quasi-static FEM was achieved by Stéphane Cotin et al., although the required preprocessing step took 8 hours on a standard PC [43]. This method, for smaller meshes, was also used by DiMaio et al. for modeling force distributions during needle insertion in tissue phantoms [52, 53].

Dynamic Formulation and the Newmark Method Rather than calculating only static deformations, we can simulate the dynamic behavior of soft tissues by solving for the acceleration, velocity, and displacement of each node for every time step to produce a history-dependent simulation. For a 2-D mesh composed of 3-node triangular elements, the dynamic FEM problem is defined by a system of d = 2n linear equations:

$$\mathbf{Ma}_i + \mathbf{Cv}_i + \mathbf{Ku}_i = \mathbf{f}_i \tag{2.6}$$

where \mathbf{M} is the mass matrix, \mathbf{C} is the damping matrix, \mathbf{K} is the stiffness matrix, \mathbf{f}_i is the external force vector, \mathbf{a}_i is the nodal acceleration vector, \mathbf{v}_i is the nodal velocity vector, and \mathbf{u}_i is the nodal displacement vector at time step i [173]. The matrices \mathbf{M} , \mathbf{C} , and \mathbf{K} are defined using the material properties of the elements in the mesh defining the deformable object, which include stiffness, compressibility, Rayleigh damping coefficients, and mass density [173]. Since they are constructed by superimposing the element mass, damping, and stiffness matrices, the number of non-zero entries in each of these matrices is O(d). When

a node in the reference mesh is moved or constrained, these matrices must be updated, a process that takes constant time for each DOF.

To solve for \mathbf{u}_i from its time derivatives \mathbf{v}_i and \mathbf{a}_i in the system 2.6, we integrate over time for each time step i. One efficient option is to use the Newmark method [163], which translates the differential system into a linear system of equations with parameters β and γ which are used to solve for displacement \mathbf{u}_{i+1} and velocity \mathbf{v}_{i+1} . Let h be the time step duration. Displacement and velocity for the next time step are approximated as:

$$\mathbf{u}_{i+1} = \mathbf{u}_i + h\mathbf{v}_i + (1-\beta)\frac{h^2}{2}\mathbf{a}_i + \beta\frac{h^2}{2}\mathbf{a}_{i+1}$$

$$\mathbf{v}_{i+1} = \mathbf{v}_i + (1-\gamma)h\mathbf{a}_i + h\mathbf{a}_{i+1}$$

We consider two solvers: a slower more accurate solver for planning and a faster solver for interactive simulation. When real-time interactive performance is desired, the value of h is adaptive; it is set using the system clock to the amount of time that has passed since the last iteration was completed.

When more accuracy is required, we set the Newmark method parameters $\beta=0.5$ and $\gamma=0.5$ to obtain the implicit system:

$$\left(\mathbf{M} + \frac{h}{2}\mathbf{C} + \frac{h^2}{4}\mathbf{K}\right)\mathbf{a}_{i+1} = \mathbf{f}_{i+1} - \left(\frac{h}{2}\mathbf{C} + \frac{h^2}{4}\mathbf{K}\right)\mathbf{a}_i - (\mathbf{C} + h\mathbf{K})\mathbf{v}_i - \mathbf{K}\mathbf{u}_i$$

$$\mathbf{v}_{i+1} = \mathbf{v}_i + \frac{h}{2}(\mathbf{a}_i + \mathbf{a}_{i+1})$$

$$\mathbf{u}_{i+1} = \mathbf{u}_i + h\mathbf{v}_{i+1} + \frac{h^2}{4}(\mathbf{a}_i + \mathbf{a}_{i+1})$$

Acceleration is obtained by solving the linear system using an iterative numerical method such as Gauss-Seidel or Conjugate Gradient that takes advantage of the sparsity of the matrices. Since \mathbf{K} , \mathbf{M} , and \mathbf{C} contain only O(d) non-zero entries, the iterative method will take $O(d^2)$ time in the worst case, although typically the number of iterations is much less than d.

For interactive simulation, we avoid solving a linear system by setting the Newmark

method parameters to $\beta = 0$ and $\gamma = 0.5$ to obtain an explicit system.

$$\mathbf{u}_{i+1} = \mathbf{u}_i + h\mathbf{v}_i + \frac{h^2}{2}\mathbf{a}_i$$

$$\left(\mathbf{M} + \frac{h}{2}\mathbf{C}\right)\mathbf{a}_{i+1} = \mathbf{f}_{i+1} - \mathbf{K}\mathbf{u}_{i+1} - \mathbf{C}\left(\mathbf{v}_i + \frac{h}{2}\mathbf{a}_i\right)$$

$$\mathbf{v}_{i+1} = \mathbf{v}_i + \frac{h}{2}\left(\mathbf{a}_i + \mathbf{a}_{i+1}\right)$$

Mass lumping, which approximates the continuous material as a particle system, decouples the system of equations into a set of algebraic equations [171, 126]. For soft materials, mass lumping results in a small loss of accuracy in the dynamics of the object [171]. With mass lumping, each time step requires only O(d) time to compute and does not require any extensive pre-computation.

In most cases, explicit integration is considered inferior to implicit integration because it is unstable for large time steps [21]. However, this instability is most prevalent for stiff materials since the maximum time step length is inversely proportional to the natural frequency of the dynamic system 2.6. Since the natural frequency is small for soft tissues, explicit integration can often be used effectively for these simulations [171].

Nonlinear FEM The above finite element formulations use Cauchy strain, a linear approximation that loses accuracy for greater deformations. Green's strain, or quadratic strain, correctly handles larger strains and global rotations [122, 172, 126, 114]. Zhuang and Canny and Picinbono et al., in addition to relaxing the quasi-static assumption, also simulate large deformations using quadratic strain, which generates a nonlinear system of equations [172, 126]. To achieve real-time visual performance for reasonably sized meshes, Zhuang uses two key approximations: mass lumping (as described above) and a graded mesh.

To accurately model large deformations, it may also be necessary to take into account the nonlinear elasticity of some materials [19, 165]. Azar et al. develop an offline FEM model of the female breast to track the position of a tumor for a biopsy procedure [19]. Because of the large deformations caused by compression, a piece-wise linear function was used to approximate the nonlinear elasticity of the tissues. Wu et al. use mass lumping

and adaptive mesh refinement to achieve real-time performance [165]. A key mathematical limitation of using Green's strain is that it cannot properly handle large compressions; simulated internal forces incorrectly decline when an element is compressed to less than 30% of its material volume [122].

2.3 Simulating Needle Procedures

2.3.1 Related Work on Needle Insertion and Surgery Simulation

We develop a 2-D simulation of tissue deformations that occur during needle insertion due to forces exerted by the needle. The model is based on a set of scalar parameters including needle friction, sharpness, velocity, and insertion location. These parameters can be selected, within limits, by the physician to improve placement accuracy. This model allows us to produce an interactive simulation and analyze the sensitivity of current medical methods to these parameters [17, 14, 15].

Simulating needle insertion requires a model of the forces exerted by the needle on soft tissue. Okamura, Simone, and O'Leary measured needle insertion forces during robot-assisted percutaneous therapy and separated the forces into distinct components: tissue stiffness forces, a cutting force at the needle tip, and frictional forces along the needle shaft [147, 123]. Kataoka et al. separately measured cutting and frictional forces during needle insertion into a canine prostate [86]. We include these force components in our model of needle insertion. DiMaio and Salcudean extracted needle insertion force profiles from camera images of needle insertion in an artificial tissue phantom [52, 53]. They used a quasi-static finite element method to replicate tissue phantom experiments in simulation, and extract a force distribution, which they modeled with a parameterized surface. Directly integrating these force profiles into a quasi-static finite element simulation of needle insertion results in a simulation with extremely fast update rates (500Hz), which is sufficient for both visual and haptic feedback. However, the method for extracting force profiles cannot be directly performed *in-vivo* for living tissues.

Setting accurate parameters for tissue material properties is also important for realistic simulation of needle insertion. Krouskop et al. estimated the elastic modulus for prostate and breast tissue using ultrasonic elastography [92]. Recent work has estimated nonlinear tissue property parameters [33, 85].

To simulate needle insertion, needle cutting and frictional forces are applied at nodes of the finite element mesh. DiMaio and Salcudean relied on node snapping, which moves the closest mesh node to the needle path in the world frame [52, 53]. Nienhuys et al. proposed mesh refinement to mitigate the discretization error caused by node snapping [121]. These methods incur an error in the location of applied needle forces that is dependent on the tissue mesh density. Our method uses mesh modification to move nodes in the reference mesh to the needle tip and along the needle shaft so the path cut by the needle is directly encoded within the reference mesh.

2.3.2 Input Anatomy Model

We specify the anatomy geometry (i.e. the tissues relevant to the simulation) using a finite element mesh. The input required for our geometric model includes a bitmap image of a 2-D slice of tissue and a segmentation of the tissue types in the image using polygons. Based on the polygonal segmentation boundaries, we automatically generate a finite element mesh G composed of n nodes and m triangular elements in a regular right triangle mesh or using the constrained Delaunay triangulation software program Triangle [144].

To compute tissue deformations, the model must also include the tissue material properties, the boundary conditions for the finite element mesh, and the needle properties. We approximate soft tissues as linearly elastic, homogeneous, isotropic materials. For each segmented tissue type, the model requires as input the tissue material properties: the Young's modulus, Poisson's ratio, damping coefficients, and mass density. Each element in the mesh may be assigned unique material properties, which allows for the simulation of multiple tissue types in one mesh. We assume no gaps between different tissue types. Mesh nodes defining elements inside bones are constrained to be fixed. A boundary condition of either

free or fixed must be specified for each node on the perimeter of the finite element mesh. Needle properties that must be specified include the cutting force (force required to cut a unit length of tissue) and the static and kinetic coefficients of friction between the tissue and needle.

2.3.3 Model of Needle Insertion

We simulate the insertion and retraction of a thin rigid needle into a 2-D slice of soft linearly elastic tissue. We do not model physiological changes that result from needle insertion, such as edema (tissue swelling). Without loss of generality, we set the coordinate axes of the world frame so that the needle is inserted along the z-axis. In 2-D, the y-axis corresponds to needle insertion height. Once the needle is in contact with tissue, we assume the needle's y-coordinate is fixed and it only moves parallel to the z-axis. Needle insertion corresponds to increasing depth z, as shown in figure 2.6.

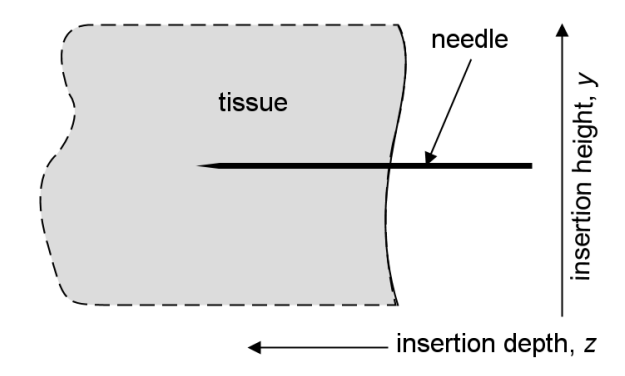


Figure 2.6. Slice of deformable tissue in the yz plane. The needle is inserted from right to left parallel to the z-axis, causing the tissue to deform.

We use a finite element method (FEM) with Newmark time integration, as described in section 2.2, to compute the displacement vector **u** for soft tissues when forces are applied by a needle during insertion or retraction. Rather than modeling the needle as a distinct meshed object, we instead model the needle implicitly by simulating the forces applied by the needle to the soft tissue. This method for representing the needle facilitates real-time interactive performance since no expensive collision detection between the needle and soft tissue is required. The needle exerts force on the tissue at the needle tip, where the

needle is displacing and cutting the tissue, and frictional forces are applied along the needle shaft [147]. These forces applied by the needle are computed and the force vector \mathbf{f}_i is updated at every time step.

We apply forces as boundary conditions on elements in the mesh. Since the needle may be inserted at any location, it is usually necessary to modify the reference mesh in real-time to ensure that element boundaries are present where the tip and friction forces must be applied. To apply the tip force, a node is maintained at the needle tip location during insertion. To apply the friction forces, a list of nodes along the needle shaft is maintained and these shaft nodes are constrained to only move along the z-axis.

2.3.4 Cutting at the Needle Tip

Let point \mathbf{p} be the location of the needle tip in the reference mesh. At all times during needle insertion, a node c is constrained to be located at the needle tip point \mathbf{p} . Let i, j, j and k be the nodes of a triangular element, as shown in figure 2.7. The needle tip at node c=i is moving horizontally to the left as shown by the vector \mathbf{r}' in figure 2.7(b). This vector is linearly transformed to the reference mesh in figure 2.7(a) and is denoted by \mathbf{r} . We assume that the z-component of \mathbf{r} always points in the positive z direction. In the reference mesh, vector \mathbf{r} intersects the segment formed by nodes j and k at the point \mathbf{q} . Let f_c be the force applied by the needle at node c and let f_b represent the magnitude of the force required to cut a length b of tissue. When $f_c \geq f_b$, the tip of the needle moves a distance b along \mathbf{r} in the reference mesh to a new point $\mathbf{p} + b\mathbf{r}$.

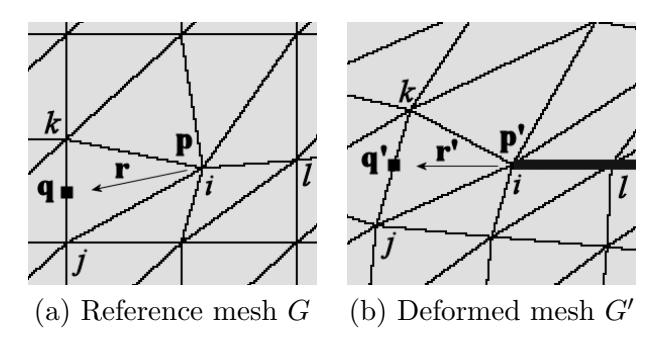


Figure 2.7. The needle is in the interior of the mesh with needle tip node c=i at point p.

After each time step during needle insertion, **p** moves closer to **q** when tissue is cut. To

maintain a planar mesh with non-overlapping elements, it is necessary to prevent a collision of node i with the segment (j, k). This is accomplished by considering the Euclidean distance between node i and \mathbf{q} and between node i and node l, the first node on the needle shaft behind the tip node. When the distance from node l to node i is more than twice the distance from node i to point \mathbf{q} , node i is added to the needle shaft: the z-component of node i is freed and returned to its original value and the node is constrained to lie on the needle axis by fixing its y-component displacement degree of freedom. The closer of node j or k is moved to $\mathbf{p} + b\mathbf{r}$ and is defined as the new tip node c. Key frames from a simulation using this type of mesh modification are shown in figure 2.8.

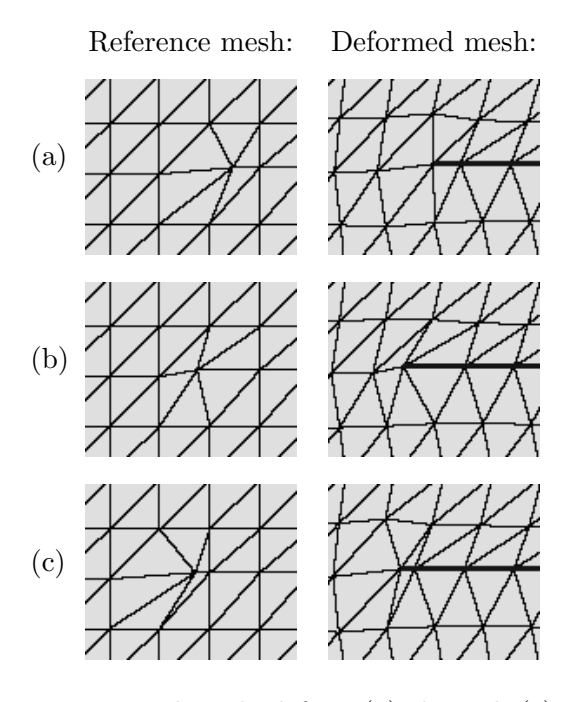


Figure 2.8. The needle tip is inserted to the left in (a) through (c). The tip node is moved onto the shaft in (c) and the next tip node is selected.

The mesh modification described is not guaranteed to be feasible for all needle insertion paths. For a topologically valid planar mesh, all elements must have strictly positive area. Consider the needle path shown in figure 2.9 and the corresponding mesh modifications. The tip node may move such that triangle (i, l, h) has negative area. Negative area triangles are formed when the last shaft node l is either above or below both the previous shaft node l and the tip node l. For this to occur, the l-component of l-co

triangular mesh prevents the formation of negative area triangles. Negative area triangles never occurred during the analysis in section 2.4, which used a sufficiently fine mesh and achieved visual real-time performance.

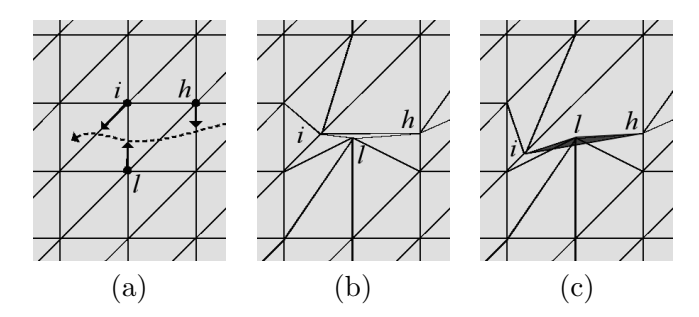


Figure 2.9. A portion of a reference mesh with a needle path (the dotted line) is shown in (a) with tip node i and shaft nodes l and h. As the tip node i moves downward in (b) and (c), triangle (i, l, h) becomes degenerate.

2.3.5 Friction Along the Needle Shaft

Our stick-slip approach to modeling static and kinetic friction between the needle shaft and the tissue is based on Baraff and Witkin [21], who modeled the friction between cloth and rigid objects. When the tangential velocity of a node along the needle shaft and the velocity of the needle are equal to within a small threshold v_s , then static friction is applied: the node is attached to the needle and moves at the same velocity along the z-axis. When the tangential force f_s required to attach the node to the needle exceeds the slip force parameter $f_{s_{max}}$, then the node is freed to slide along the needle shaft and a dissipative force f_k is applied. The dissipative force is proportional to the normal force, which we approximate as proportional to the surrounding tissue stiffness.

2.3.6 Needle Retraction

During needle retraction, a tip node is not maintained since no cutting force is required. When the needle retracts past a node on the shaft, that node is removed from the shaft node list. Friction is applied on all the shaft nodes exactly as during insertion.

2.3.7 Visualization of Needle Insertion

The visual feedback of the simulation is intended to mimic the experience of a physician performing needle insertion under imaging guidance, such as ultrasound or MRI, where the needle insertion axis is on the imaging plane. As input, the visualization requires a 2-D image corresponding to the undeformed reference state of the tissue. We use texture-mapping to warp the input image and display the deformations resulting from forces exerted by the needle. We take advantage of the fact that the interpolation function inside triangular elements for linearly elastic finite element methods is linear, as described in section 2.2.2. We use the node coordinates in mesh G as texture coordinates for the input image, which is displayed using the node coordinates in mesh G'.

2.4 Application to Prostate Brachytherapy Cancer Treatment

We apply our simulation of needle insertion to prostate brachytherapy. Our anatomy model of the prostate is based on an image obtained at UCSF Medical Center using an ultrasound probe in the sagittal plane, as shown in figure 1.4. The image is the first frame an ultrasound video that includes a full needle insertion into the prostate in the saggital plane. The prostate in the image was segmented by a physician at UCSF. The polygonal segmentation was used to manually generate a mesh composed of n=676 nodes and m=1250 triangular elements. The ultrasound image also served as the texture map image for the simulator. The boundary of the mesh is defined by a square for which the right face (where the needle is inserted) is free, the bottom face corresponding the trans-rectal ultrasound probe is rigid, and the other two faces containing the bladder and bone are also marked rigid.

We set the Young's modulus E and Poisson's ratio ν based on the results of Krouskop et al. to E=60 kPa and $\nu=0.49$ for the prostate and E=30 kPa and $\nu=0.49$ for the surrounding tissue which we model as fat [92]. Needle properties are treated as variables

that can be set in the user interface of the simulation. To set default values, we compared the output of the simulation with the ultrasound video from UCSF and set unknown simulation parameters so that the simulation output closely matched the ultrasound video. Although it is difficult for non-specialists to identify gland boundaries in ultrasound, UCSF clinicians comparing the two image sequences judged them as remarkably similar. We hope to perform controlled experiments to further evaluate simulation accuracy across multiple patients.

At any time during needle insertion, a seed can be implanted at the location of the needle tip $\mathbf{s} = \mathbf{p}$ in the reference mesh. We assume that the seed does not move in the reference mesh after it is implanted. Since the mesh may be modified after seed implantation, the seed may not always be located at a node. For computational efficiency, a mesh element e containing \mathbf{s} is stored in memory. The location of the seed \mathbf{s}' in the deformed mesh is found using the shape functions of e and the displacement of the element nodes in constant time [173]. When any node f of element f is moved during the simulation, it is necessary to update the element containing the seed. Since the point f may only be inside an element containing node f, the standard zero-winding rule for polygon inside-outside tests is applied to find the new containing element in constant time.

The simulator was implemented in C++ using OpenGL for visualization and tested on a 750MHz Pentium III PC with 256MB RAM. When executed in interactive simulation mode, a user can guide the needle and implant seeds using a mouse, as shown in figure 2.10. For a model with 1250 triangular elements, the simulator responds at the rate of 24 frames per second, sufficient for visual feedback (but not fast enough for haptic control).

The visual feedback of the simulation is intended to mimic the experience of a physician performing brachytherapy, as shown in figure 2.11. We believe this output can be useful for physician training [17]. The interactive simulation runs on standard PC's running Windows.

2.5 Conclusion and Future Work

We developed a 2-D biomechanical simulation of needle insertion in soft tissues based on a finite element model and a reduced set of scalar parameters including needle friction,



Figure 2.10. The simulation user interface, which is based on an ultrasound image, is intended to mimic the experience of a physician performing brachytherapy. The physician interactively guides the needle using a mouse and implants seeds (small squares). Tissue deformations and seed locations are predicted and displayed. The implantation error is the distance between the seed and its target (cross) after needle retraction.

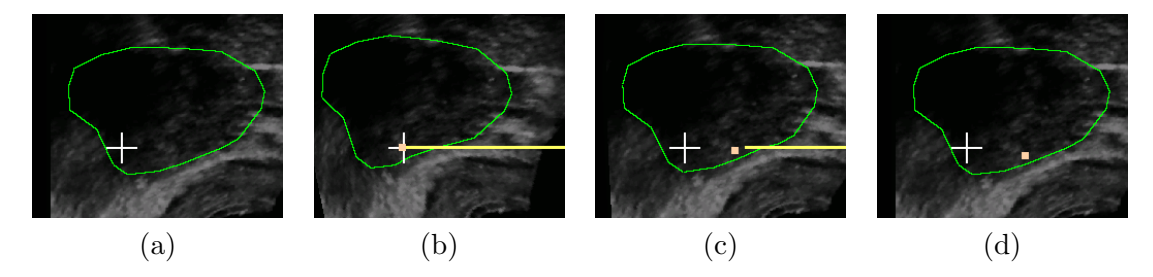


Figure 2.11. Sample frames from a simulation of brachytherapy needle insertion based on deforming an ultrasound image of the human prostate using our finite element model.

sharpness, and velocity, where the mesh is updated to maintain element boundaries along the needle shaft and the effects of cutting at the needle tip and frictional forces are simulated. The simulation achieves 24 frames per second for 1250 triangular elements on a 750Mhz PC. The speed of the simulation is affected by the scalability of the finite element method system solver. We described solvers requiring between O(d) and $O(d^2)$ time. The value of d will not rise during a simulation because no new nodes are added, and it may in fact decrease as the y-axis DOF of some nodes are lost when they are constrained along the needle shaft. A screen capture of the software is shown in figure 2.10. In future work, we plan to extend our current 2-D finite element simulation and planner to 3-D elements and

nonlinear tissue material properties. Further validation of the needle insertion simulation using animal or patient video sequences is also desired. To facilitate physician training, the simulation can be run interactively using different patient anatomies and tissue properties. We plan to test future versions of our needle insertion simulation as a tool for physician training.

Chapter 3

Target Localization using

Deformable Image Registration

Recent advances in medical imaging are enabling physicians to non-invasively pinpoint the location of cancerous cells inside the body. But after obtaining diagnostic images in which the cancer is localized, the patient is generally treated in a different facility, days, weeks, or months later. During this time, the patient may experience substantial changes, such as tumor size changes or weight changes that affect the location of the cancer cells relative to markers on the patient's skin. Furthermore, due to the clinical constraints of the diagnostic imaging modality and treatment procedure, the patient's position may be differ between the diagnostic and and treatment phases. For radiation cancer treatment, these patient changes due to time, movement, and imaging modality constraints can lead to misalignment of the radiation dose, reducing the conformality of dose to the tumor and resulting in suboptimal treatment [9, 22, 71].

In this chapter, we develop an image registration approach that explicitly considers tissue deformations and variations in model parameters between patients to improve target localization across images acquired at different times. The method, which is based on a biomechanical model of soft tissue deformation, combines a nonlinear optimization algorithm with results from soft tissue modeling described in chapter 2.

We apply the new method to register diagnostic MRSI prostate images with radiation treatment planning images. To obtain a sufficient signal-to-noise ratio for MRSI, a probe must be placed near the prostate, which results in substantial deformations of the surrounding soft tissues, as shown in figure 1.2. This probe must be removed during treatment. Results for 10 prostate cancer patient cases indicate that our method provides a statistically significant improvement in target registration accuracy compared to past methods [9].

3.1 Introduction to Deformable Image Registration

Registration is the process of finding a spatial transform that maps points from one image to the corresponding points in another image of the same subject [168]. The input data to the image registration process is two images: the first image is defined as the fixed image (or reference image) F and the second image is defined as the moving image (or deforming image) M. The goal of registration is to determine a spatial transform T that will align the moving image with the fixed image.

Most image registration methods, including the method developed in this chapter, use a software framework consisting of a transform, a metric, and an optimizer [168]. The transform T, parameterized by a set of transform parameters \mathbf{p} , defines a mapping of points from the fixed image onto the moving image. This transform can be used to generate a transformed moving image M' by applying the the transform $\mathbf{x}' = T(\mathbf{x}|\mathbf{p})$ for each pixel coordinate $\mathbf{x} \in F$ and setting the pixel intensity at pixel coordinate \mathbf{x} of M' to the pixel intensity at \mathbf{x}' of M. The metric $S(\mathbf{p}|F, M, T)$ measures the similarity of the the transformed moving image M' with the fixed image F. An optimizer searches over the space of all feasible transform parameters \mathbf{p} to maximize the quantitative registration quality criterion defined by the metric S so M' matches F as best as possible.

In rigid registration, we assume that the spatial transform T that maps points from the fixed image to the moving image is a rigid body transform: it includes only translation and rotation, as shown in figure 3.1. Given a point \mathbf{x} in F, the corresponding point in M is given by $\mathbf{x}' = T(\mathbf{x}|\mathbf{p})$. In 2-D, the parameter vector \mathbf{p} for a rigid transform $T(\mathbf{p})$

has a dimension of 3 (x-axis translation, y-axis translation, and rotation by θ degrees in the xy-plane). When registering rigid 3-D volumes, \mathbf{p} has a dimension of 6 (3 translation degrees of freedom and 3 rotation degrees of freedom) [168].

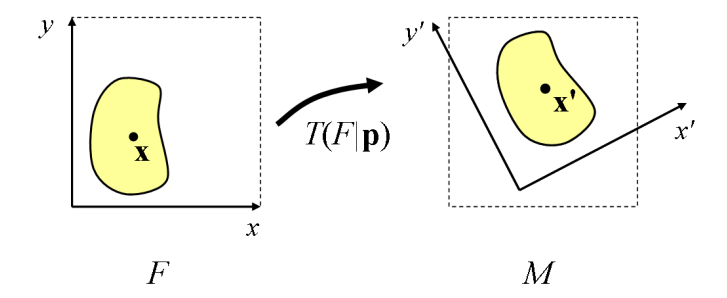


Figure 3.1. Fixed image F and a moving image M are enclosed in dashed lines. The object of interest in F is translated and rotated in M. The transformation T defines a rigid transformation that maps points \mathbf{x} from F to \mathbf{x}' in M.

However, soft tissues may deform between image acquisitions due to causes such as patient position changes, physiological changes such as bladder volume changes, and imaging requirements such as probes. In these cases, the assumption of a rigid transform is no longer valid. In *non-rigid* or *deformable registration*, we do not assume that the transform T is limited to translation and rotation. Instead, T can represent an arbitrary mapping from F to M, as shown in figure 3.2.

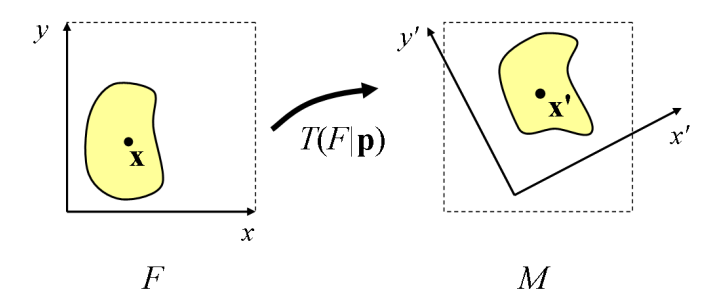


Figure 3.2. Fixed image F and a moving image M are enclosed in dashed lines. The object of interest in F is translated, rotated, and deformed in M. The transformation T defines a deformable transformation that maps points \mathbf{x} from F to \mathbf{x}' in M.

In the most general case, a deformable transform T would define a mapping individually for every pixel in F to its corresponding location in M. For 3-D images with x, y, z pixel dimensions of d_x, d_y, d_z , respectively, this would result in a parameter set \mathbf{p} of dimension $3d_xd_yd_z$. Since medical images today are typically of the dimensions $256 \times 256 \times 256$,

optimizing a parameter vector of dimension $3 \cdot 256^3 = 50,331,648$ variables with a possibly nonlinear, non-convex objective metric S is computationally intractable.

To limit the dimension of **p** and make the deformable registration problem computationally tractable, numerous methods have been developed that explicitly compute transformations for a subset of pixels in the image, and then intelligently interpolate the transformation for the remaining pixels in the image. Methods based on this principle include B-splines [168], energy models [164], viscous models [38], and elastic models [20]. Each of these methods implicitly makes assumptions about the types of deformations that occur in the subject of the image being registered.

In this chapter, we develop a deformable registration algorithm specifically designed for medical images that explicitly considers soft tissue deformations and variations in model parameters between patients. Rather than relying on a mathematical abstraction such as B-splines that has no physical basis, our approach is based on building a biomechanical model of the tissue in the image. By explicitly modeling the underlying anatomical structures, our approach is physically based.

The core of our image registration method is a biomechanical model based on a finite element method. In 1982, Bajcsy and Broit performed pioneering work in the application of elastic finite element models to deformable image registration [20]. Initial methods used a regular finite element grid and computed a set of external forces that deform the grid to minimize a function defined by an elastic energy and a similarity energy. This work was later extended to include a rigid registration pre-processing step and multi-resolution hierarchical registration [168]. Advances in geometric algorithms and computation speed are now enabling the generation of finite element meshes that conform to tissue type boundaries and simulations that explicitly model sources of large soft tissue deformations in just seconds or minutes of computation time. Recent work has modeled large deformations such as the compression of breast tissue for biopsies [19], as well as our work on prostate deformations due to forces exerted by needles during insertion into soft tissue [16].

However, biomechanical models require knowledge of tissue material properties such as

stiffness and compressibility. In past work on deformable image registration that we are aware of, tissue material properties are either fixed as constants for all patients [167, 26, 45] or implicitly held constant across an entire image [164]. After building a biomechanical model, we include uncertain parameters such as tissue material properties in **p** as variables. This allows our optimizer to estimate these uncertain parameters and maximize deformable image registration quality. When applied to prostate MRS/MR images, our new method results in a significant improvement over previous methods, as discussed in section 3.3.5.

3.2 Deformable Registration with Model Parameter Estimation

Our image registration method defines a transform T that maps points between a fixed image and a moving image. Given a fixed image F and a moving image M, the goal is to compute parameters \mathbf{p}^* such that $T(F|\mathbf{p}^*) = M$. In our method, T is invertible. The inverse mapping T^{-1} transforms every point in the moving image M to its coordinate in the fixed image F.

At the core of our method to compute T is a finite element method that estimates the deformation of soft tissues in the fixed image due to known external forces or constraints. Treating the uncertain tissue stiffness properties and external forces as unknown variables, we estimate their values using nonlinear local optimization to maximize image registration quality.

3.2.1 Method Input

The input for our image registration method includes a fixed image F and moving image M. To build a biomechanical model, the method also requires polygonal segmentation boundaries of distinct tissue types in the images. This information is typically already available in radiation oncology applications since segmentation is required for dose planning. Although segmentation is usually performed by hand for reliability in clinical practice,

methods are being developed to automatically segment tissue types [168]. Each segmented region in the images must be labeled with a corresponding tissue type, such as bone or muscle. We let m be the number of distinct tissue types in the fixed image F.

Our method also optionally accepts as input known constraints on tissue deformation between the images. These constraints are specified as a set H of homologous point pairs. For each pair $(\mathbf{x}, \mathbf{x}') \in H$, \mathbf{x} is a point in the fixed image and \mathbf{x}' is the coordinate of the homologous point in the moving image. For images in which no bones are present, we require $|H| \geq 1$ to ensure that the linear system of equations defined by the finite element method in section 3.2.2 is solvable.

Our method also optionally accepts as input a set L of points or polygonal tissue type boundaries that may be subject to external forces of unknown magnitudes. For example, points on the segmented boundary of the bladder should be listed since the bladder may expand or contract between image acquisitions.

3.2.2 Finite Element Model of Soft Tissue Deformation

As discussed in chapter 2, we approximate soft tissues as nearly incompressible (Poisson's ratio of 0.49), linearly elastic, and isotropic. Although tissue stiffness properties and external forces will be modified during the optimization method, initial default values must be set in the transform parameter vector **p**. Based on tissue stiffness measurements obtained using ultrasound elastography [92], we temporarily assign a Young's modulus of 30 kPa to all soft tissues and assume bones are rigid. We assume initial external forces all have zero magnitude.

We automatically generate a finite element mesh that conforms to the segmented tissue boundaries for the fixed image F. For 2-D, we generate triangular elements using the constrained Delaunay triangulation software program Triangle [144]. For 3-D, we use the tetrahedral mesh generation software TetGen [146]. Elements in the mesh are assigned default stiffness properties. Mesh nodes defining elements inside bones are constrained to be fixed. We let l be the number of nodes along boundaries included in set L.

We use the finite element method (FEM) to estimate tissue deformations. The homologous points $(\mathbf{x}, \mathbf{x}') \in H$ specify displacement constraints for the finite element method, where the node at point \mathbf{x} is displaced by $\mathbf{x}' - \mathbf{x}$ and constrained as fixed. The deformations of the surrounding soft tissues are then computed using FEM. As described in Chapter 2, the FEM problem for a given N-D fixed image mesh with n nodes is defined by a system $\mathbf{K}\mathbf{u} = \mathbf{f}$ containing Nn linear equations where \mathbf{K} is the global stiffness matrix, \mathbf{f} is the external force vector, and \mathbf{u} is the nodal displacement vector. For each fixed node, we remove its N corresponding degrees of freedom from the system. We solve the linear system of equations numerically using the Gauss-Seidel method to compute nodal displacements \mathbf{u} for non-fixed nodes. By using linear interpolation within each element of the mesh, the nodal displacement vector \mathbf{u} defines a complete invertible mapping function T between the fixed image and the moving image. The mapping T is applied to every pixel in the fixed image F to obtain the deformed fixed image $T(F|\mathbf{p})$.

3.2.3 Quality Metric

We use a quality metric S to quantify how closely the deformed fixed image $T(F|\mathbf{p})$ matches the moving image M. Any image similarity metric S can be used, including image intensity metrics such as mutual information, homologous point distance measures, and segmented region overlap metrics [168]. However, the computation time and convergence properties of the optimization algorithm defined in section 3.2.4 depend on the quality metric.

3.2.4 Optimization of Uncertain Parameters

Our image registration method treats tissue stiffness properties and external forces at user-specified nodes as uncertain parameters. The stiffness for soft tissue is constrained between Y_{min} and Y_{max} , where we select $Y_{min} = 1$ kPa and $Y_{max} = 600$ kPa as limits based on tissue elastography results [92]. External force magnitudes are unbounded. We define

the optimization objective function for maximization as:

$$Q = S - \alpha E$$

where S is the selected quality metric, α is a scaling parameter, and E is the percent of strain energy due to external forces. To compute E, the optimization algorithm computes tissue deformations twice, first without external forces and then with external forces added. For each case, it computes the total strain by summing the strain of each element in the mesh, which is quickly computed by multiplication of element stiffness matrices and vectors of node displacements [173]. We subtract αE in the objective function to prioritize optimization of parameters of the physically-based model (tissue stiffness) relative to external forces. Appropriately setting α , which is problem specific, produces visually smoother image mappings by preventing unrealistic large magnitude external forces.

We apply the Steepest Descent method with Armijo's Rule for line search [23] to maximize the nonlinear objective function Q. The variables, which include m tissue stiffness properties and l external force degrees of freedom, are defined in a vector \mathbf{p} of dimension m+l. The quality metric Q is a function $Q(\mathbf{p})$. We numerically compute derivatives for the gradient $\nabla Q(\mathbf{p})$ using finite differences with sufficiently high differences to avoid numerical difficulties. At iteration i of the Steepest Descent optimization method, Armijo's Rule selects the next candidate point $\mathbf{p}_{i+1} = \mathbf{p}_i + 2^t \lambda \nabla Q(\mathbf{p}_i)$ for predefined step size λ by sequentially incrementing integer t starting at t = 0 to solve for the maximum t that improves $Q(\mathbf{p}_{i+1})$. Then the gradient $\nabla Q(\mathbf{p}_{i+1})$ is computed and the Steepest Descent algorithm repeats until iteration j where $\|\nabla Q(\mathbf{p}_j)\| < \epsilon$ for $\epsilon = 0.001$. Because the objective function Q is not guaranteed to be convex, this method may not find a global optimal solution [23]. We label the local optimal solution found as \mathbf{p}^* .

3.2.5 Visualizing Registration Output

In 2-D, rendering the deformed fixed image can be performed quickly using texturemapping, which is built-in to most modern computer graphics cards. We take advantage of the fact that the interpolation function inside triangular elements for linearly elastic finite element methods is linear, as described in Chapter 2. Rather than explicitly applying the mapping T to every pixel in the fixed image F, we instead only compute the transformation $T(\mathbf{x_i}|\mathbf{p})$ for nodes $\mathbf{x_i}$ in the mesh, and use hardware accelerated texture-mapping to linearly interpolate pixel transformations for pixels inside the mesh elements. We are currently developing computationally efficient visualization methods for 3-D deformable image registration results.

3.3 Application to Prostate Cancer Treatment

We apply our deformable registration method to prostate cancer treatment. In 1996, Kurhanewicz et al. showed that magnetic resonance spectroscopic imaging (MRSI), a type of functional imaging that measures concentration of metabolic compounds, can be used to noninvasively diagnose and locate cancerous tumors in the prostate [96, 97, 95, 138]. By measuring choline, polyamine, and citrate levels which change with the evolution and progression of cancer, MRSI can be used to identify the location and extent of dominant intraprostatic lesions (DIL's) in the prostate [94]. Combining magnetic resonance imaging (MRI) with MRSI allows identification of a tumor with specificity of up to 91% [138].

Knowledge of cancer location can assist physicians during radiation treatment planning. Numerous studies are indicating that improving the conformality of radiation dose to the cancer location significantly improves cancer treatment and reduces negative treatment side effects [154, 80, 93]. Physicians can escalate the radiation dose to the cancer location using treatment methods such as HDR brachytherapy [129], permanent seed brachytherapy [170], and external beam radiation treatment [127, 166].

To obtain improved signal-to-noise ratio (SNR) and better spatial resolution MRI and MRSI, an endorectal probe integrated with a pelvic phased array (PPA) coil is commonly used. The endorectal probe is critical for the acquisition of high spatial resolution (≈ 0.3 cc) MRSI data of the prostate due to the approximate 10-fold increase in SNR relative to external phased array coils [96, 95, 138, 75, 72, 78]. However, the probe may cause considerable nonlinear translation and distortion of the prostate [89], as shown in figure 3.3. The probe

is generally removed during imaging for radiation treatment planning and therapy. To effectively utilize the MRSI data, clinicians must register the probe-in image to a probe-out image.

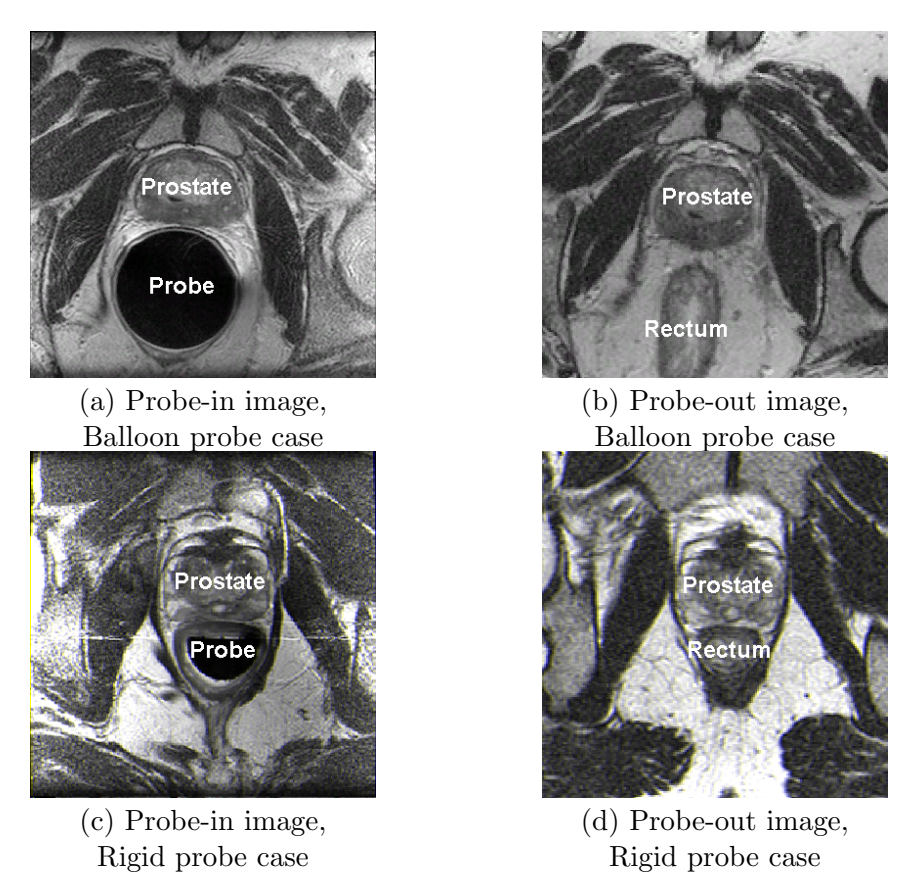
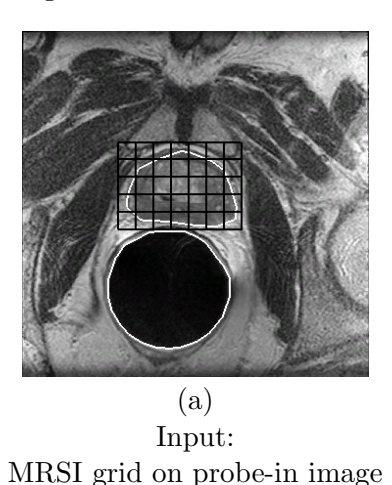
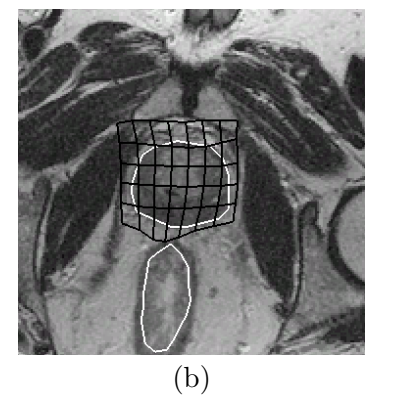


Figure 3.3. MRSI data for the prostate is obtained with a balloon endorectal probe inserted and inflated (a) or a rigid endorectal probe (c) as shown in the axial MR images at the mid-gland of the prostate. Radiation treatment is performed with the probe removed (b), (d).

To register probe-in images obtained during a combined MRI/MRSI staging examination to probe-out images, we apply our deformable registration method described in section 3.2. We use a 2-D finite element model and estimate the deformation of the prostate and surrounding tissues in the plane of the image due to the insertion of an endorectal probe. A 2-D model is sufficient for our application since the out-of-plane deformations are smaller than the thickness of imaging slices [89, 44]. However, patient-specific model parameters required as input for the biomechanical model are not known with certainty, including tissue stiffness properties for the prostate and surrounding soft tissues. Additional uncertain

parameters include forces due to patient position changes, bladder volume changes, and other factors that differ between the probe-out and probe-in images but are not explicitly included in our linear elasticity soft tissue deformation model. As described in section 3.2, we use a local nonlinear optimization algorithm to estimate uncertain patient-specific tissue stiffness properties and external forces to maximize image registration quality. Compensating for computed tissue deformations results in a nonlinear warping of the MRSI grid, as shown in figure 3.4.





Output: Warped MRSI grid on probe-out image

Figure 3.4. Spectroscopy data is obtained for voxels inside the MRSI grid overlaid on an the axial probe-in MR image (a). Our image registration method warps the MRSI grid to the probe-out image for use during treatment planning (b).

Past work on image registration of the prostate includes rigid transformations [60, 89], spline transformations [59, 87], energy models [164], and finite element models [167, 26, 45] for registering dose calculation CT images [167], treatment and interventional MR images [60, 59, 26], probe-in/probe-out MR images [45], and MR images with endorectal balloons at different levels of inflation [164]. Fei et al. ignore tissue deformations that occur between pre-operative and interventional MR images and maximize the mutual information (MI) or correlation coefficient (CC) of the image intensity histograms using rigid body translation and rotation of the prostate [60]. Kim et al. rigidly align probe-in and probe-out images by first rotating the images into the same plane, then doing a rigid 2-D translation in plane [89]. For a sample probe-in/probe-out case in which prostate deformation is minimal, this method achieves less than 2 mm registration error. Fei et al. and Kessler et al. use spline methods, which nonlinearly warp an image using a non-physically based model with

a large number of degrees of freedom [59, 164]. They use multiresolution approaches to increase avoidance of local maxima of the CC and MI metrics. Wu et al. develop a hybrid method for registering MR images with endorectal balloons at different levels of inflation by maximizing an objective function containing a weighted sum of MI and regularization energy from a non-finite element physically based model [164]. A key advantage of these methods based on MI and CC quality metrics is that tissue segmentation is not required, but these methods have large numbers of degrees of freedom, are prone to local maxima, require long computation times (18-22 minutes for Wu et al.), and have potentially larger error due to soft boundaries of deformable tissues [60, 164]. MI and CC metrics cannot be applied in isolation to our problem of registering a probe-in image to a probe-out image because, without segmentation, the probe-out image contains no information on the probe insertion location. Physically based biomechanical models, such as the finite element method, have potential to address some of these limitations. Finite element methods require image segmentation to define tissue type boundaries (to specify tissue-specific material properties) and mesh generation. Yan et al. performed pioneering work in deformable image registration based on the finite element method to calculate fractionated dose in a deforming organ [167]. They segmented a single tissue type, the rectal wall, and applied the method to inter-treatment motion using fiducials to set boundary conditions. Bharatha et al. and Crouch et al. apply linear elasticity finite element modeling to the prostate using a tetrahedral mesh with distinct central gland and peripheral zone regions [26] and a hexahedral mesh using a medially-based solid representation with uniform tissue properties inside the prostate [45]. Image registration based on biomechanical models, including finite element and energy methods, require tissue material properties as input. In past work we are aware of, material properties are either fixed as constants for all patients [167, 26, 45] or implicitly held constant across an entire image [164]. Our image registration method uses nonlinear optimization to set patient-specific values for uncertain parameters in the biomechanical model including separate tissue stiffness values for each segmented tissue type [6, 7, 10, 9]. We also explicitly warp MRSI grids to compensate for tissue deformations.

3.3.1 Patient Image Acquisition

We applied our image registration method retrospectively to 10 patient cases. The patients were recruited from January to June, 2003, at the Magnetic Resonance Science Center (MRSC), University of California, San Francisco. A balloon probe (USA Instruments, Aurora, OH) with 100 cc of air injected was used for 5 patients while a rigid probe (MedRad, Pittsburgh, PA) was used for the remaining 5 patients. Once inflated, the balloon probe had a circular cross-section with a 48 mm diameter. The rigid probe was a half ellipse, in cross-section, with the anterior surface flat. Its right - left extent was 29 mm and its anterior - posterior extent was 16.5 mm. Combined MRI/MRSI was obtained using the balloon or rigid probe in combination with an external phased array of coils on a 1.5 Tesla GE system (Signa, GE Medical Systems, Milwaukee, WI). For rigid probe cases, the USA torso phased array was used, while the GE pelvic phased array was used for the balloon probe cases. These two probes were selected as the MedRad coil is the only MR probe currently available commercially and the USA Instruments probe is commercially manufactured and will soon be a commercially available alternative probe.

The probe-in images used in this study were acquired during a "PROSE" (PROstate Spectroscopy and imaging Examination) MRI/MRSI examination (GE Medical Systems, Milwaukee, WI). The details of the MR imaging method used have been discussed in previous work [96, 129, 89, 67]. Spectroscopy data was obtained for $7 \times 7 \times 7$ mm voxels (≈ 0.3 cc). Thin-section high spatial resolution axial T_2 weighted fast spin-echo images of the prostate and seminal vesicles were obtained with a slice thickness of 3 mm, an inter-slice gap of 0 mm, and a field of view (FOV) of 14 cm. At the end of the "PROSE" MRI/MRSI examination, the endorectal probe was removed with the subject remaining on the imaging table. Additional sagittal and axial fast spin echo T_2 weighted images were acquired without the endorectal probe using the phased array coil alone for signal reception. As with the probe-in case, patients were scanned in the supine position. All image acquisition parameters for the probe-out images were the same as for the probe-in images except for increasing the field-of-view (FOV) from 14 cm to 20 cm to partially compensate for the reduction in SNR obtained without the use of an endorectal probe.

3.3.2 Application of the Deformable Registration Method

We apply the deformable registration method described in section 3.2 to the prostate images described in section 3.3.1 We define the fixed image F as the probe-out image and define the moving image M as the probe-in image. The transform T attempts to mimic the deformation of the prostate and surrounding tissue due to endorectal probe insertion. Given a probe-out image F and a probe-in image M, the goal is to compute parameters \mathbf{p} such that $T(F|\mathbf{p}) = M$. The inverse mapping T^{-1} , which can be used during treatment planning, transforms every point in the MRSI grid of the probe-in image M to its coordinate in the probe-out image F.

From the probe-in and probe-out MR image volumes, we selected a single probe-in image slice M at the mid-gland of the prostate for each patient. We then manually selected a corresponding probe-out image slice F that is at the same level as the probe-in image for the patient. As a pre-processing step, we rigidly register the images by aligning points on non-deforming tissues, such as points in bones, using a homologous point method to translate the images [74].

We manually segmented the selected images using a standard image segmentation method by drawing polygonal outlines on a computer screen to define the boundaries of tissue types. For cases in which the tissue type (such as the rectum) was close to circular, we specified a circle and radius that the software automatically converted to a polygonal approximation. The image registration method requires segmentation of the probe and prostate in the probe-in image and the probe entry location (rectum) and prostate in the probe-out image. For improved accuracy in the biomechanical simulation, we also segmented bones and separately segmented the central gland (CG) and peripheral zone (PZ) of the prostate in the probe-out image. Additional segmentation of the probe-in image will not improve results since the biomechanical model is applied to deform the probe-out image.

For this application, the known constraints on deformation are the displacements caused by the endorectal probe. As shown in figure 3.6, our model expands the rectum lining in the probe-out image to match the probe outline in the probe-in image. We project points along the probe outline in F along the ray based at the rectum center and constrain them to the intersection with the probe outline in M. This defines the set of homologous points H. We define set L as the prostate gland boundary.

We automatically generate a finite element mesh composed of n = 500 nodes and between 800 and 1,000 triangular elements using *Triangle* [144]. Image segmentation and the mesh generated for the probe-out image of a sample case are shown in figure 3.5.

Based on tissue stiffness measurements obtained using ultrasound elastography in previous work [92], we assign a Young's modulus of 60 kPa to the central gland of the prostate and 30 kPa to all surrounding tissues for all patient images during intialization of the method.

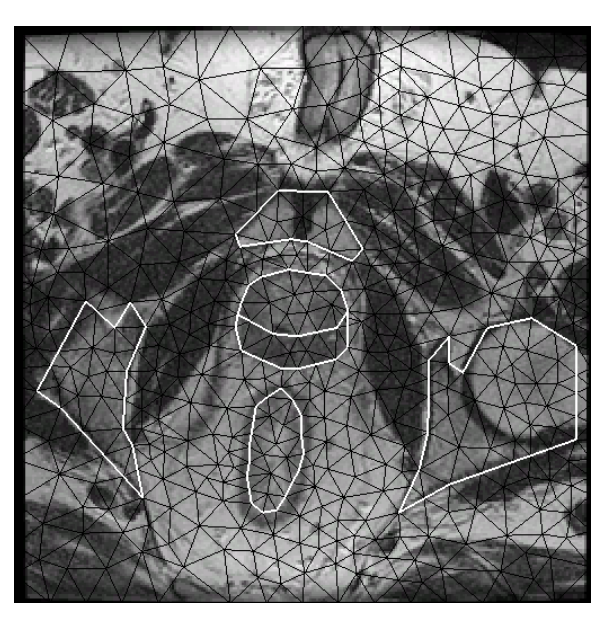


Figure 3.5. Conformal Delaunay triangular mesh (black triangles) for a probe-out image with central gland and peripheral zone of the prostate, probe entry location (rectum), and bones segmented (in white).

The number of distinctly segmented soft tissue types in F was m = 3. After meshing, the number of nodes in set L is typically between 20 and 40. This results in a parameter vector \mathbf{p} of size between 43 and 83.

We define the metric S using the Dice Similarity Coefficient (DSC), a metric that measures overlap of polygonal regions. For this application, we measure the overlap between the prostate area in the probe-in image M and the prostate area in the deformed probe-out

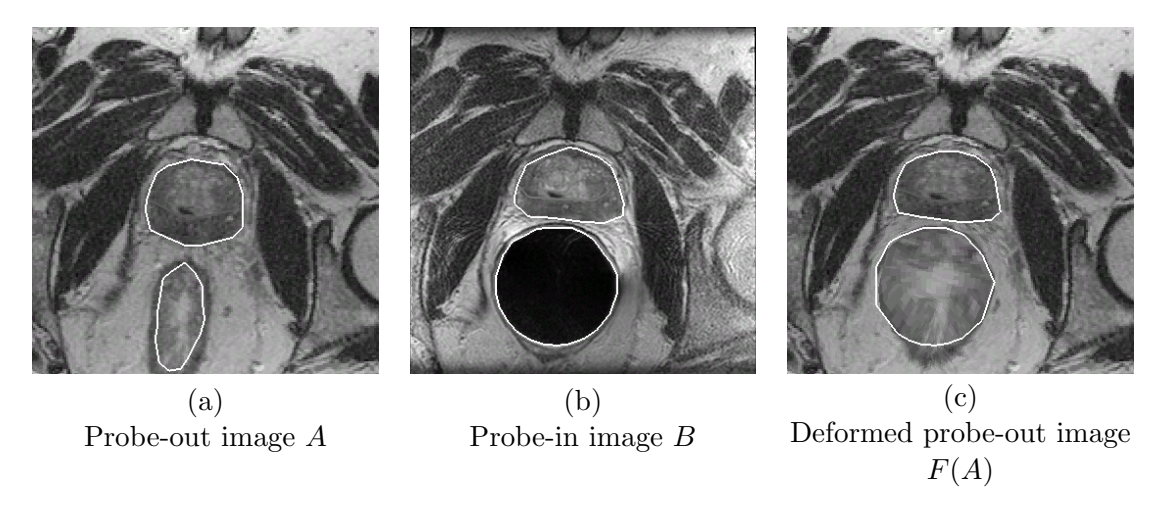


Figure 3.6. Probe-out image A with segmented prostate gland (outlined in white, middle) and rectum (outlined in white, bottom) (a) and the corresponding probe-in image B with prostate and probe segmented (b). The method computes image F(A) (c) which displaces mesh nodes along the rectum in the probe-out image to the probe outline in the probe-in image and estimates the resulting soft tissue deformations. The image registration quality (DSC value) between (b) and (c) is 97.8%.

image $T(F|\mathbf{p})$ using the Dice Similarity Coefficient (DSC). Superimposing an outlined area from two images, the DSC is defined as:

$$D = \frac{2a}{2a+b+c}$$

where a is the number of picture elements (pixels) shared by both areas, b is the number of pixels unique to the first area, and c is the number of pixels unique to the second area [48, 26]. The DSC is a scalar between 0 and 1 with higher values representing better quality registration.

3.3.3 Warping the MRSI Grid

The 3-D MRSI data is collected from a volume and individual spectra are generally reconstructed for $7 \times 7 \times 7$ mm voxels within a grid overlaid on this volume. To help register spectroscopic data to the probe-out image, we transform each intersection point in the regular MRSI grid from the probe-in image plane to the probe-out image using the inverse of mapping T. The warped MRSI grid is the output of the algorithm: it registers the probe-in MRSI data to a probe-out image for use during treatment planning.

3.3.4 Method Evaluation and Parameter Selection

We evaluate the image registration method using two metrics: DSC and point error. We compute the DSC using the prostate outline in the probe-in image M and the prostate outline in the deformed probe-out image $T(F|\mathbf{p}^*)$. We compare our deformable image registration method to a rigid registration method where the center of mass of the prostate total gland is translated in the probe-out image by the distance between its center of mass in the probe-out and probe-in images [26].

As a second measure of image registration quality, we evaluate displacement errors of homologous points in the interior of the prostate on the probe-in images M and the deformed probe-out images $T(F|\mathbf{p}^*)$. As in past work by Bharatha et al. [26], we selected points on the probe-in images at the posterior border of the central gland near the midline of the prostate. We then selected homologous points corresponding to the same tissue location on the probe-out images using patient-specific local image pixel intensity variations as references. Our image registration method maps the point on the probe-out image F to the deformed probe-out image $T(F|\mathbf{p}^*)$ so we can directly measure the point error: the distance between the homologous point in M and $T(F|\mathbf{p}^*)$. We compare this error to the distance between the homologous points in the given probe-in image M and probe-out image F to quantify the registration improvement resulting from the method.

Two parameters of the method that influence image registration quality and must be set are n, the number of nodes in the mesh, and α , the scaling parameter in the objective function Q that weighs direct maximization of the DSC relative to the percent of strain energy E due to external forces. For a subset of the patient data (3 balloon probe cases and 3 rigid probe cases), we evaluated image registration quality for n = 100, 500, and 1,000 and for $\alpha = 0.0$, 0.005, and 0.01.

3.3.5 Results

The mean DSC of our method was 97.5% with a standard deviation of 0.7% for the 5 balloon probe cases. For the 5 rigid probe cases, the mean DSC was 98.1% with a standard

deviation of 0.4%. As shown for a patient case in figure 3.6, the deformed probe-out image closely matches the probe-in image. In Table 3.1, we compare our image registration method to rigid registration based on center-of-mass translation for the prostate total gland. We performed paired t-tests to determine the statistical significance (P < 0.05) of the results and found that the improvement in DSC using our method was statistically significant for both the balloon probe (P = 0.035) and the rigid probe (P = 0.013) cases.

	Rigid Translation	Our Method
5 balloon probe cases	86.6% (10.4%)	97.5% (0.7%)
5 rigid probe cases	86.6%~(10.4%)	$97.5\% \ (0.7\%)$

Table 3.1. DSC mean and standard deviation (in parentheses) for image registration quality.

The results of our method for the point error metric are shown in Table 3.2. Our method reduces displacement error between the homologous points in the probe-in and probe-out images by a mean of 74.8% to a mean error of 1.95 mm for the balloon probe cases. For the rigid probe cases, the reduction was by a mean of 70.0% to a mean error of 0.97 mm. We performed paired t-tests and found that the reduction in error was statistically significant for both the balloon probe (P = 0.0045) and the rigid probe (P = 0.0099) cases.

	Mean point error for probe-in / probe-out images (mm)	Mean point error after our method (mm)	Mean reduction in error (%)
5 balloon probe cases	9.22 (3.22)	1.95 (0.22)	74.8% (15.1%)
5 rigid probe cases	3.93(1.59)	0.97(0.51)	$70.0\% \ (27.2\%)$

Table 3.2. Point displacement error means and standard deviations (in parentheses) for sample homologous points on the boundary of the prostate central gland and peripheral zone near the midline.

For these results, we set parameter α in the formula for objective function Q in section 3.2.4 to 0.005. Decreasing α allows for greater external forces while increasing α penalizes external forces in favor of tissue stiffness during optimization of uncertain parameters. The trade-off effect of α on DSC and point error is shown in figure 3.7(a) and (b). Increasing α to 0.01 or decreasing α to 0.0 results in lower mean DSC and higher mean point errors.

We also performed sensitivity analysis on n, the number of nodes in the finite element

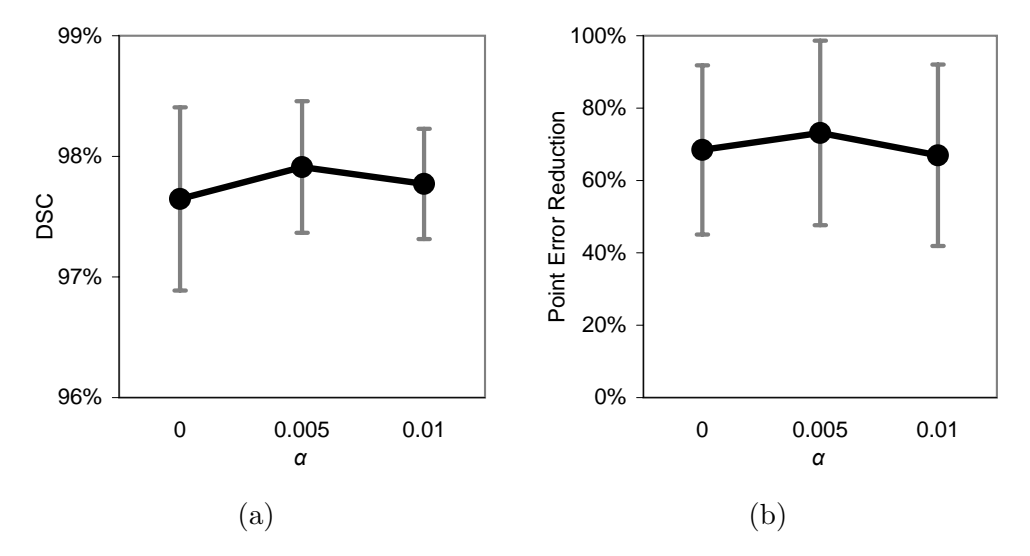


Figure 3.7. Sensitivity of mean image registration quality (DSC and point errors) to the optimization parameter α , with error bars for standard deviations.

mesh. Increasing n improves average image registration quality measured by DSC, as shown in figure 3.8(a). However, this improvement comes at a large computation cost, as shown in figure 3.8(b), with 1,000 node meshes requiring over 6 minutes of computation time on average. Results in this study use meshes with n = 500 nodes, which requires less than 1 minute of computation time per image slice while maintaining good image registration quality; DSC results with n = 500 are not significantly different from DSC results with n = 1,000 (P = 0.324).

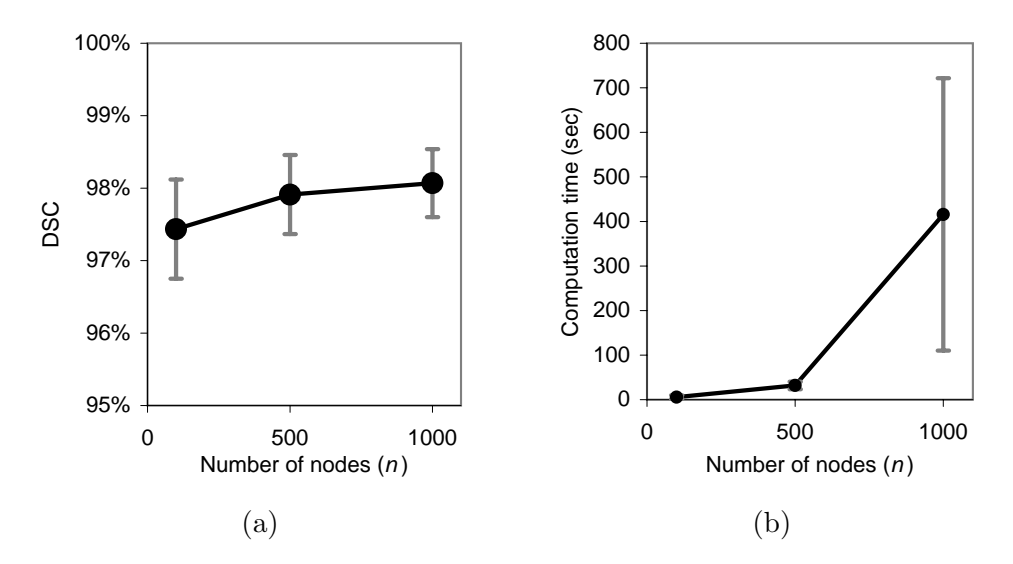


Figure 3.8. Sensitivity of mean DSC image registration quality (a) and computation time (b) to the number of nodes n in the mesh, with error bars for standard deviations.

We show the output of our image registration method for a sample balloon probe patient in figure 3.9 and for a rigid probe patient in figure 3.10. The resulting warping of the MRSI grid is clearly nonlinear in both cases. The percentage of strain energy due to external forces E averaged 8.6% for balloon probe cases and 10.0% for rigid probe cases. The low value for E demonstrates that, for both types of probes, most of the strain energy in the finite element simulation was due directly to the displacement of tissues caused by the probe rather than other uncertain external forces. Mean computation time for the image registration algorithm was comparable for both balloon and rigid probe patients on a 1.6 GHz Pentium-M laptop PC: 39.8 seconds with a standard deviation of 20.8 seconds for balloon probe cases and 34.2 seconds with a standard deviation of 11.8 seconds for rigid probe cases.

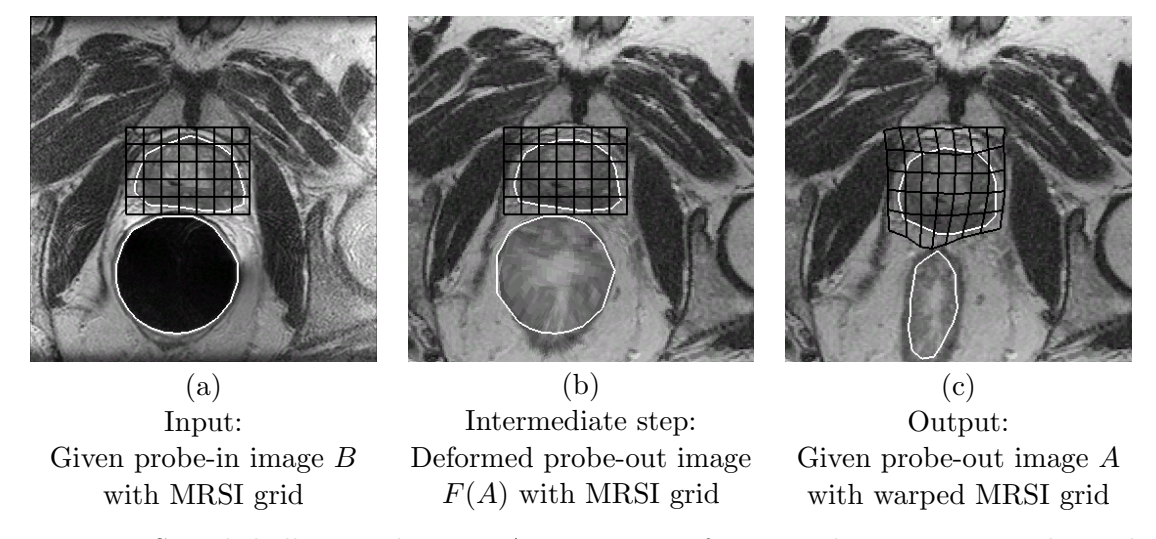


Figure 3.9. Sample balloon probe case. A comparison of input and output images shows the nonlinear warping of the MRSI grid. The probe-in image (a) closely matches the computed deformed probe-out image (b) outside the endorectal probe. The MRSI grid is warped to the undeformed probe-out image (c) for use during treatment planning.

3.3.6 Discussion

Compensating for tissue deformations using biomechanical simulation with nonlinear parameter estimation results in better image registration than center-of-mass translation for all of the 10 cases tested. The DSC increased by an average 7.5% across all patients when using our method. These improvements come at a cost of computation time: our

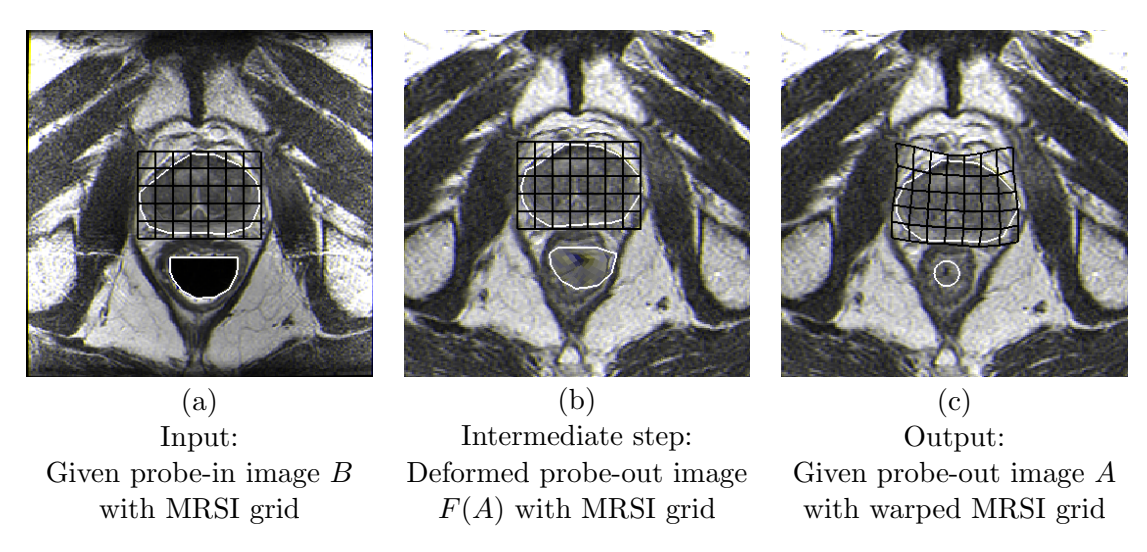


Figure 3.10. Sample rigid probe case.

method required on average 37 seconds for each patient image slice in addition to manual image segmentation time for the probe-in and probe-out images.

Since our method only explicitly considers deformation in a 2-D (x,y) plane, it will not address out-of-plane deformations along the z-axis in a 3-D volume. However, past work has shown that z-axis deformations are small relative to the resolution of the volume images. Kim et al. found that the difference in the superior/inferior length of the prostate between probe-in and probe-out images was always less than the z-axis thickness of an axial MR image (3 mm) for 25 patient cases (15 rigid probe and 10 balloon probe) [89]. Crouch et al. measured seed displacements for 25 implanted seeds between balloon probe-in and probe-out images and found that the z-axis displacement averaged 2.67 mm, less than the 3 mm MR image slice thickness [44].

Our image registration method is sensitive to the segmentation of the image and the optimization algorithm may incorrectly add external forces or modify tissue stiffness properties if the segmentation is incorrect. Bhathara et al. quantified the error introduced by human segmentation: a human subject segmenting five 1.5 T MRI scans five times in random order achieved a mean DSC for segmentation reproducibility of 95% with a 95% confidence interval of (92%, 97%) while a second subject achieved a mean of 96% with confidence interval (95%, 97%) [26].

Using our method for image registration resulted in a greater improvement in mean DSC for balloon probe images (10.9%) than for rigid probe images (4.0%) when compared to registration by center-of-mass translation. Although balloon probes result in better quality images, these probes produce much larger deformations [89]. Kim et al. manually measured the anterior-posterior (AP) and right-left (RL) dimensions of the prostate in probe-in and probe-out images and found that the balloon probes on average compressed the prostate 3.5-fold more in the AP direction and stretched the prostate 2.5-fold more the RL direction than the rigid probe [89].

When compared to other image registration methods based on tissue deformation models, our method performs well. Our results visually appear to have smaller error than results from 2-D slices of 3-D volumes obtained by Wu et al., although a precise comparison is not possible because the accuracy of their method was not numerically quantified [164]. Wu et al. consider images taken with a balloon probe at different levels of inflation which results in different deformations from removing the probe entirely for a probe-out image. Crouch et al. tested their finite element based method using an artificial tissue phantom with 25 radioactive seeds implanted inside [45, 44]. The phantom was deformed by a balloon probe resulting in average seed displacements of 9.377 mm, similar to the 9.22 mm average displacement of our test points in the interior of the prostate. To achieve 2.0 mm average point errors for the seeds, Crouch et al. required a mesh of 14,068 nodes and 14 hours of computation time for full 3-D deformations. Our method, which was tested on MR images of patient cases rather than tissue phantoms, achieved a less than 2 mm error for a representative point but required under 1 minute of computation time per image slice. Our DSC of 97.5% is higher than the 94% obtained by Bharatha et al. with a 3-D biomechanical finite element model for the registration of balloon endorectal probe-in images to rectal obturator (smaller) probe images [26]. However, subjects in that study were scanned in two different positions, supine and lithotomy, at two different field strengths, 1.5 T and 0.5 T, and with two different rectal probes, an MR expandable endorectal probe and a rectal obturator, which may have compromised image registration quality.

3.4 Conclusion and Future Work

Biomechanical modeling with nonlinear estimation of uncertain tissue parameters can improve the quality of deformable image registration. For the application of registering (probe-in) MRSI data with (probe-out) radiation treatment planning, improvements are greater for balloon probes compared to rigid probes due to the larger tissue deformations that occur with balloon probes. The algorithm achieved a mean DSC quality of 97.5% for five balloon probe patients and 98.1% for five rigid probe patients. The improvement over center-of-mass rigid registration is statistically significant (P < 0.05). Our method reduced displacement error between homologous test points in the probe-in and probe-out images by a mean 74.8% to a mean error of 1.95 mm for balloon probe cases and by a mean 70.0% to a mean error of 0.97 mm for rigid probe cases. The method required on average 37 seconds of computation time on a 1.6 GHz Pentium-M laptop PC to estimate and compensate for tissue deformations and produce a nonlinear mapping between probe-in and probe-out images.

Our current implementation independently registers 2-D slices of tissue from a 3-D MRI volume. In future work, we will develop an analogous 3-D biomechanical simulation and image registration method to explicitly account for deformations and displacements that occur between imaging planes in 3-D volumes. Generating patient-specific 3-D conformal tetrahedral meshes with a controlled number of elements and validating the 3-D image registration approach using a new imaging protocol with slices sufficiently thin to capture out-of-plane deformations will require substantial new research.

Chapter 4

Motion Planning for Rigid Needles in Deformable Soft Tissue

Minimally invasive medical procedures such as brachytherapy, biopsies, and treatment injections often require inserting a rigid needle to a specific target location inside the body to implant a radioactive seed, extract a tissue sample, or inject a drug. In all cases, the needle tip should be inserted as close as possible to a predetermined target inside soft tissue. Unfortunately, inserting and retracting a needle causes the surrounding soft tissue to displace and deform: ignoring these deformations can result in substantial placement error, as illustrated in figure 4.1. Physicians must therefore learn to compensate for these effects to insert the needle to the correct location within the tissue.

We develop a sensorless planning system based on a biomechanical simulation of needle insertion to reduce placement error. Here, "sensorless" refers to a minimalist approach to robotics in which no real-time sensor input is required as the procedure is performed [58]; i.e., no real-time tracking of tissues or the needle is required during the procedure. Our pre-operative planning system combines the simulation described in chapter 2 with an optimization algorithm to compute a needle offset that compensates for tissue deformations to reach a given target location. The planner iteratively tests different insertion locations

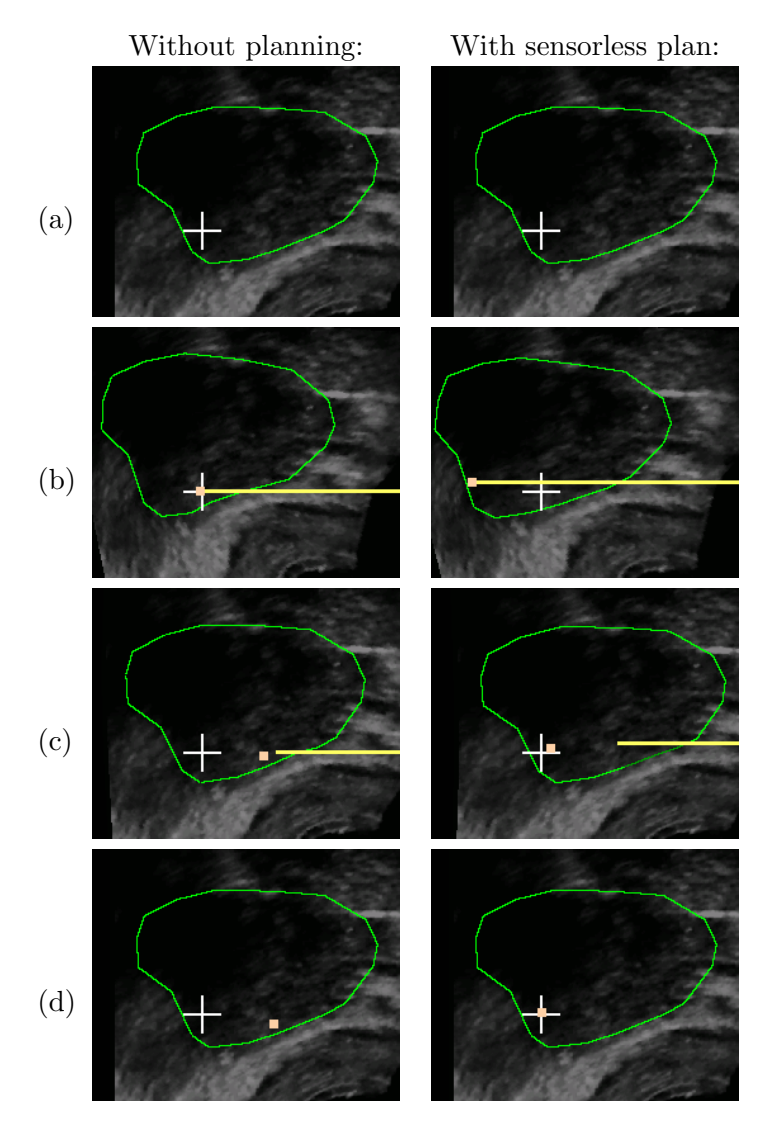


Figure 4.1. Four vertical frames illustrate brachytherapy needle insertion based on deforming an ultrasound image of the human prostate using simulation. The left column shows results without planning, producing substantial placement error. The right column shows results with the sensorless plan, with minimal placement error. The target implant location is indicated in all frames with a cross fixed in the world frame. Frame (a) outlines the undeformed prostate. In Frame (b), the needle is inserted and the radioactive seed (small square) is released at the needle tip. In Frame (c), the needle is retracted. Frame (d) indicates the resulting placement error, the distance between the target and resulting actual seed location. Without planning, placement error is substantial: 26% of the prostate diameter, resulting in damage to healthy tissue and failure to kill cancerous cells. With sensorless planning, shown in the bottom image of Frame (d), placement error is negligible in this simulation.

and depths to compute the optimal needle offset: a sensorless motion plan as illustrated in figure 4.1 right column greatly reduces placement error in simulation.

We apply the system to permanent seed prostate brachytherapy, a minimally invasive medical procedure in which a physician uses needles to permanently implant radioactive seeds inside the prostate that irradiate surrounding tissue over several months. The success of this procedure depends on the accurate placement of radioactive seeds within the prostate gland [46, 131]. For permanent seed brachytherapy, we define seed placement error as the Euclidean distance between the desired location specified by the dosimetric plan (the target) and the actual implanted seed location after needle retraction. An experienced physician implanting seeds (without stabilizing needles) in 20 patients achieved average placement errors of 0.47 cm in depth and 0.22 cm in height for an average placement error of 0.63 cm, a substantial error of 21% of average prostate diameter (3 cm) [148]. Realtime ultrasound imaging is used during the procedure to help guide each needle along a straight path and to verify the depth of the needle tip in the world frame. However, the imaging cannot effectively be used to compensate for deformations because it does not include crisp markers with known positions inside the soft tissues, as shown in figure 1.4. Tissue deformations during needle insertion and retraction contribute to placement error during brachytherapy [131, 148], as illustrated in figure 4.1. In this chapter, we describe our sensorless planning approach to reduce placement error without relying on real-time imaging.

4.1 Related Work: Sensorless Planning and Needle Insertion

In robotics, sensorless planning algorithms, pioneered by Mason and Erdmann in the 1980's [58], have been developed to position and orient mechanical parts using parallel jaws [30, 70], vibrating surfaces [28], single joint robots over conveyor belts [3], and squeeze and roll primitives for micro-scale parts [115]. For seed placement planning using rigid needles, our goal is to model and compensate for mechanical response before actions are performed.

Medical needle insertion procedures may benefit from the more precise control of needle position and velocity made possible through robotic surgical assistants. A survey of recent advances in medical robotics was written by Taylor and Stoianovici [152]. Dedicated hardware for needle insertion is being developed for stereotactic neurosurgery [112], MR compatible surgical assistance [36, 51], and prostate biopsy and therapeutic interventions [61, 139].

When real-time sensor data such as MR or X-ray imaging is available during needle insertion procedures, robotic control algorithms can be used to steer the needle to the desired target when the target and relevant obstacles are all visible in the images. Shi et al. developed an image-guided robotic system containing a needle as an end-effector that uses real-time X-ray imaging to track a target and send its position to a control system [145]. The needle's tip position is computed using forward kinematics and the control system repeatedly updates the insertion path of the needle tip to a straight line path to the target.

When real-time sensor data is unavailable or unreliable, sensorless planning based on pre-operatively predicting the effects of tissue deformations can be applied. Azar et al. use a piece-wise nonlinear finite element model to track the position of a tumor during breast compression before a breast cancer biopsy [19]. Recent work has addressed planning local trajectories in deformable tissue for flexible needles with symmetric tips by translating and rotating the base [54] and steerable bevel-tip needles that can be controlled by rotating the bevel [158, 8]. In this chapter, we explicitly use simulation of insertion of rigid needles into deformable tissues to plan needle procedures without real-time sensor input [16].

4.2 Problem Definition

As illustrated in figure 4.2, we consider a 2-D slice of tissue in the yz plane. The needle moves parallel to the z-axis at some insertion height y_r to an insertion depth z_r . Let $\mathbf{p_t} = (y_t, z_t)$ be a target point in the undeformed prostate specified in the world frame. The point $\mathbf{p_r} = (y_r, z_r)$ denotes the release point, the world frame coordinate of the needle tip when it is fully inserted into the soft tissue and an action or implant is performed. The

release point is the sample collection point in the case of a biopsy, the drug injection point in the case of anesthesia, or the seed implantation location in the case of permanent seed brachytherapy. We assume that the implant moves with the deforming tissue that surrounds it. After needle retraction, the actual final location of the implant is $\mathbf{p_a} = (y_a, z_a)$, the implant point specified in the world frame. In the case of brachytherapy, the implant point is the actual final location of the radioactive seed.

The implant point $\mathbf{p_a}$ is a function of $\mathbf{p_r}$ and $\mathbf{p_a} \neq \mathbf{p_r}$ due to tissue deformations during needle insertion. Placement error ε is the Euclidean distance between $\mathbf{p_a}$ and $\mathbf{p_t}$:

$$\varepsilon = \|\mathbf{p_a} - \mathbf{p_t}\|.$$

For a given target point inside soft tissue, the planning problem is to compute a release point $\mathbf{p_r}$ that minimizes placement error.

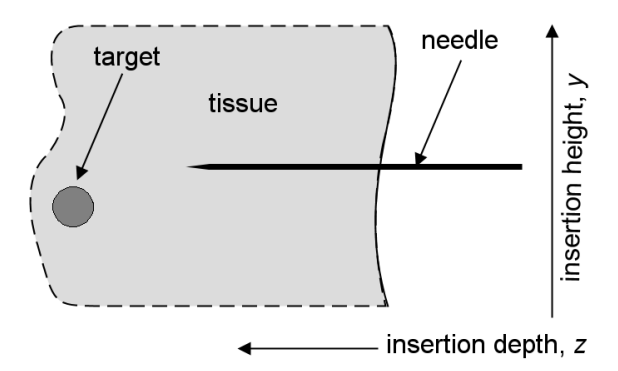


Figure 4.2. Slice of deformable tissue in the yz plane. The needle is inserted from right to left parallel to the z-axis, causing the tissue to deform.

We approximate the needle as thin and rigid. The height of needle insertion is determined by y_r , which we assume is continuous. Needle insertion corresponds to increasing depth z, as shown in figure 4.2. Once the needle is in contact with tissue, its y-coordinate is fixed and it only moves parallel to the horizontal z-axis. Based on anatomical constraints, we assume the maximum feasible insertion depth is given by z_{max} and the region of skin where the needle can be feasibly and safely inserted into the patient is restrict the range of y_r to $y_r \in (y_{min}, y_{max})$.

4.3 Needle Insertion Planning Method

4.3.1 Method Overview

Computing the placement error $\varepsilon = \|\mathbf{p_a} - \mathbf{p_t}\|$ requires a relation between the implant location $\mathbf{p_a}$ and the release point $\mathbf{p_r}$. We compute $\mathbf{p_a}$ as a function of $\mathbf{p_r}$ numerically using simulation. (We are not aware of a closed-form equation that computes deformations in soft tissues caused by needle insertion.)

The planner assumes that the simulator estimates the deformation of elastic soft tissues caused by needle insertion in 2-D over time steps of duration h. We use the simulation described in chapter 2, which computes the node displacements \mathbf{u}_i as a function of time step i as external forces \mathbf{f}_i change over time. We use a fixed time step duration h to obtain simulated deformations for times t=hi, $i \geq 0$.

The planning algorithm's inputs and outputs for each needle and target location are defined by:

Input:

- Needle insertion simulator with required parameters (as defined in chapter 2)
- \bullet **p**_t: Target coordinate in the tissue
- (y_{min}, y_{max}) : Range of feasible insertion heights
- z_{max} : Maximum feasible insertion depth
- v: Needle velocity during insertion and retraction
- h: Simulation time step duration

Output:

• $\mathbf{p_r}^*$: Release point that minimizes placement error

A naïve planner that ignores tissue deformations would set $\mathbf{p_r} = \mathbf{p_t}$. If tissue deformations occur, the naïve will not reach the specified target, as shown in simulation in figure 4.1 left column and using a mesh representation in figure 4.3.

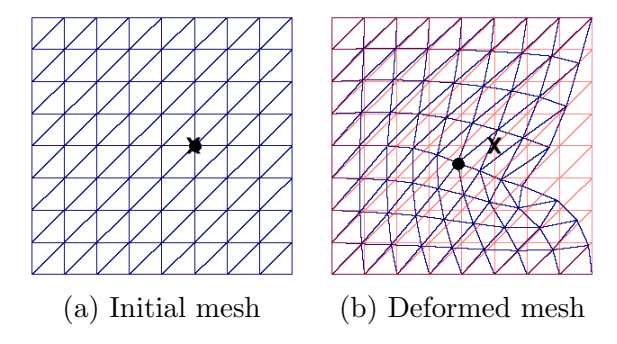
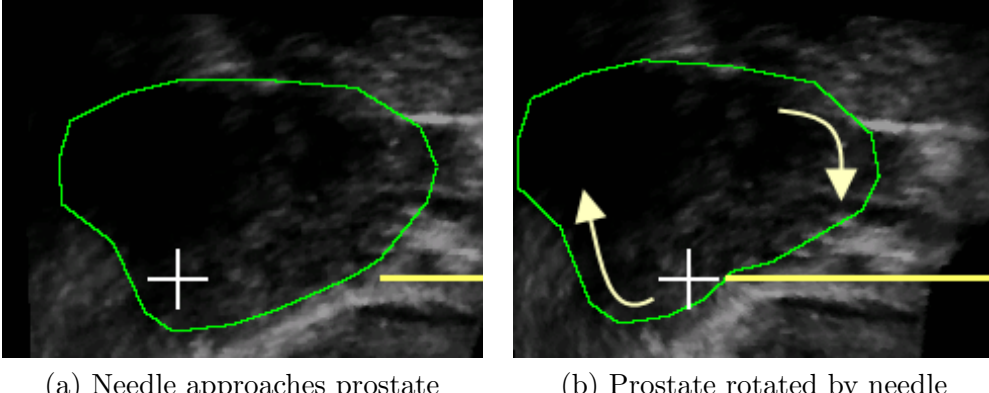


Figure 4.3. Consider a mesh representation of soft tissue as defined in chapter 2 used for simulation. Let the target be located at node k of the mesh. At time step i=0, the coordinate of the target in the reference mesh, denoted by \times , coincides with the target in the world frame, denoted by \bullet , because displacement $\mathbf{u}_{\mathbf{k}0}$ of node k is 0 (a). At time step i>0, the tissue is deformed (b). Both the \times and \bullet represent the same location within the tissue, but the world frame coordinate differs from the reference frame coordinate by the displacement $\mathbf{u}_{\mathbf{k}i} \neq 0$.

To estimate an optimal release point $\mathbf{p_r}^*$, the planner computes an offset from $\mathbf{p_t}$ for both the insertion depth and height. The offset for needle insertion depth is necessary because tissue in front of the needle tip is compressed during insertion; the needle must be inserted deeper than z_t to compensate for this compression. The offset for insertion height is necessary since organs or glands (such as the prostate) may rotate during needle insertion. For example, if the target is located near the bottom of the prostate, inserting the needle near the target height causes the prostate to rotate slightly clockwise, as shown in figure 4.4. The needle must be inserted higher to compensate for its deflected path through the prostate. This occurs because the prostate is composed of a stiffer material than the surrounding soft tissue. Hence, both needle insertion depth and height must be planned to minimize placement error.

4.3.2 Planning Method

Given a target point $\mathbf{p_t}$, the goal of needle insertion planning is to find an optimal release point $\mathbf{p_r}^*$ that minimizes placement error $\varepsilon = \|\mathbf{p_a} - \mathbf{p_t}\|$, where the implant location $\mathbf{p_a}$ is



(a) Needle approaches prostate

(b) Prostate rotated by needle

Figure 4.4. When the needle pushes against the lower half of the prostate from the right, the prostate rotates clockwise slightly because it is stiffer than the surrounding tissue. This slight rotation can lead to significant changes in the optimal needle insertion height.

a function of the release point $\mathbf{p_r}$. The optimal $\mathbf{p_r}^*$ cannot be computed analytically by differentiating the error function ε because the relationship between $\mathbf{p_r}$ and $\mathbf{p_a}$ can only be computed numerically by simulation. Our algorithm efficiently uses simulation to estimate the optimal $\mathbf{p_r}^*$.

We first describe how to efficiently compute $\mathbf{p_a}$ and ε using simulation when given the release point $\mathbf{p_r} = (y_r, z_r)$. Then, we propose a method to estimate the optimal depth z_r^* that minimizes the error ε when a candidate insertion height y_r is given. Finally, we describe how to select candidate insertion heights to estimate the optimal y_r^* that minimizes ε .

Computing Placement Error Given the Release Point

Given the target $\mathbf{p_t}$ and the release point $\mathbf{p_r} = (y_r, z_r)$, the placement error $\varepsilon =$ $\|\mathbf{p_a} - \mathbf{p_t}\|$ requires an estimate of $\mathbf{p_a}$, the implant location after needle insertion and retraction using a release point of $\mathbf{p_r}$. We compute this estimate using simulation. Initially, the needle tip is outside the body, which corresponds to tip depth z < 0. We set the insertion height y_r and simulate needle insertion to a depth of $z = z_r$ and implant a "seed" in the mesh as described in chapter 2. We then simulate needle retraction until z < 0, wait for steady state, and then use the final seed location as an estimate for $\mathbf{p_a}$.

The time required to estimate $\mathbf{p_a}$ can be reduced significantly by replacing the simulation of needle retraction with an O(1) time computation. The simulation algorithm described in section 2.3 always maintains a node at the location of the needle tip during insertion. Assume the needle tip, located at node k, has reached the release point $\mathbf{p_r}$ at time step i in the simulation. As described in chapter 2, both the reference mesh coordinate $\mathbf{x_k}$ and displacement $\mathbf{u_{k_i}}$ for node k at time step i are known after the FEM system of equations has been solved. By the elasticity assumption, the displacement $\mathbf{u_{k_j}}$ will be 0 for all iterations j after needle retraction at steady state because no external forces are being applied to the soft tissue. Hence, the location in the world frame of the release point $\mathbf{p_r}$ after needle retraction will be $\mathbf{x_k} + \mathbf{u_{k_j}} = \mathbf{x_k}$. Since we assumed that the implant location will move with the deforming tissue, the implant location after retraction is $\mathbf{p_a} = \mathbf{x_k}$ and the placement error is $\varepsilon = \|\mathbf{x_k} - \mathbf{p_t}\|$, where $\mathbf{x_k}$ is the reference mesh coordinate of the node k at the needle tip when it reaches the release point $\mathbf{p_r}$ in simulation. Simulating needle retraction is not required.

Minimizing Placement Error Given Insertion Height

When given a candidate needle insertion height y_r , we simulate needle insertion at height y_r to find the insertion depth z_r^* that minimizes placement error ε .

$$z_r^* = \arg\min \varepsilon(z_r|y_r)$$

Because the simulation of needle insertion is history dependent, we must compute $\varepsilon(z|y_r)$ in order to compute $\varepsilon(z+dz|y_r)$ for dz, z > 0. We begin with the needle located outside the soft tissue (z < 0) and simulate needle insertion at height y_r until $z = z_{max}$. Using the simulation described in chapter 2, z is increased by dz = vh every time step, where h is the time step duration and v is the needle velocity. The insertion depth z at each time step serves as a candidate for the optimal release point z_r^* . We compute $\varepsilon(z|y_r)$ in O(1) time as described in section 4.3.2 for every time step and save the z_r^* for which ε is smallest. Because ε is computed for every feasible insertion depth, the optimal z_r^* for the given y_r is guaranteed to be found (within a resolution of dz) regardless of the convexity properties of the function $\varepsilon(z_r|y_r)$.

This optimization computes $z_{max}/(vh)$ simulation time steps, each requiring O(d) time (or slower if a more accurate FEM model or solver is used) as described in chapter 2. Since the needle tip will move a distance vh each time step, the resolution of z^* is vh. A small time step h is desirable to improve the resolution of z^* , but the number of time steps required to compute the optimal insertion depth z^* grows as h decreases.

Estimating Insertion Height to Minimize Placement Error

For any candidate insertion height y_r , we compute the optimal insertion depth z_r^* and the resulting placement error:

$$\varepsilon(y_r) = \min \varepsilon(z_r | y_r).$$

Our goal is to minimize $\varepsilon(y_r)$ over the given feasible range $y_{min} \leq y_r \leq y_{max}$. The value of y_r^*

$$y_r^* = \arg\min \varepsilon(y_r)$$

combined with the corresponding optimal z_r^*

$$z_r^* = \arg\min \varepsilon(z_r|y_r^*)$$

specifies the optimal release point $\mathbf{p_r}^* = (y_r^*, z_r^*)$ that minimizes placement error ε .

Minimizing $\varepsilon(y_r)$ is difficult because derivative values are not available and the function is not guaranteed to be unimodal (strictly quasiconvex). In general, an approximate minimum of $\varepsilon(y_r)$ can be found using a grid search over $y_r \in (y_{min}, y_{max})$.

However, the function $\varepsilon(y_r)$ for some simulations will be unimodal near the minimum. In particular, this property will hold when it is not possible to insert the needle at different heights and still reach the same point in the reference mesh of the tissue. Although this property is not guaranteed, it holds for most feasible targets in our simulation that are not adjacent to a tissue type boundary. In such cases, a line search method can be used to find the optimal y_r^* . We use the golden section search method [23] because, unlike a standard binary search, it does not rely on derivative information (which is not available in the simulation). Golden section search is a variant of the Fibonacci search that requires fewer

error function evaluations. Each iteration of the line search evaluates the error function $\varepsilon(y_r)$ for a new candidate insertion height y_r , which requires simulating needle insertion at height y_r to find an optimal depth z_r^* and resulting error, as described in section 4.3.2. The algorithm iterates until the optimal is found within a specified tolerance; convergence is guaranteed if the error function is unimodal.

4.4 Application to Brachytherapy Seed Implantation

Figure 4.1 provides a simulated case study showing that deformations can produce significant errors in final seed placements during prostate brachytherapy. Placement error should be minimized to achieve the desired radioactive dose distribution.

During permanent seed prostate brachytherapy, roughly 20 stiff needles are each loaded with multiple seeds separated by spacers. As the needle is retracted, the "train" of seeds and spacers are released in the prostate. In this chapter, we only address placement of the first seed in the train and ignore the remaining seeds in each needle. Each needle is fully retracted before the next is inserted. Hence, we assume each needle insertion and seed implantation procedure is independent. Unlike needles, we assume seeds do not cut tissue. Hence, a seed will move only when the surrounding tissue deforms, which satisfies our assumption that an implant moves with the surrounding deforming tissue. Also, a metal block containing approximately 50 holes at fixed coordinates is used by the physician to guide each needle during brachytherapy needle insertion. We relax the discrete insertion coordinate restriction and allow the insertion height y_r to vary continuously, which allows for better minimization of placement error but will require new hardware in medical practice.

Below we demonstrate the performance of the planner for seed placement during prostate brachytherapy. We assume the needle is inserted at a constant velocity of 0.5 cm/sec. The prostate model used in this chapter is based on an anonymous patient who underwent a need insertion procedure at the UCSF Medical Center, as described in section 2.4.

4.4.1 Target Test Case

We test our planning algorithm for the target $\mathbf{p_t} = (1.50 \text{ cm}, 3.00 \text{ cm})$ shown in figure 4.1 for a 3cm diameter prostate. Without planning, deformations are ignored and the needle is inserted with zero offsets to $\mathbf{p_r} = \mathbf{p_t}$. Based on our simulation, this results in the seed being implanted at $\mathbf{p_a} = (1.41 \text{ cm}, 2.21 \text{ cm})$, a placement error of $\varepsilon = 0.79 \text{ cm}$ (26% of the prostate diameter).

4.4.2 Optimizing Insertion Depth

For insertion of a needle at the target height $y_r = y_t = 1.5$ cm, we plot the placement error $\varepsilon(z_r|y_r = y_t)$ in figure 4.5. The insertion depth $z_r = z_t = 3.0$ cm yields a placement error of $\varepsilon = 0.79$ cm, 26% of prostate diameter. The error in the depth coordinate is caused primarily because the tissue in front of the needle tip is being compressed before it is cut. Hence, the needle must be inserted deeper than the target depth to decrease the error. To minimize ε for $y_r = y_t$, the needle should be inserted to a depth of $z_r^* = 3.84$ cm, which reduces the error by 82% to only $\varepsilon = 0.14$ cm, 5% of prostate diameter.

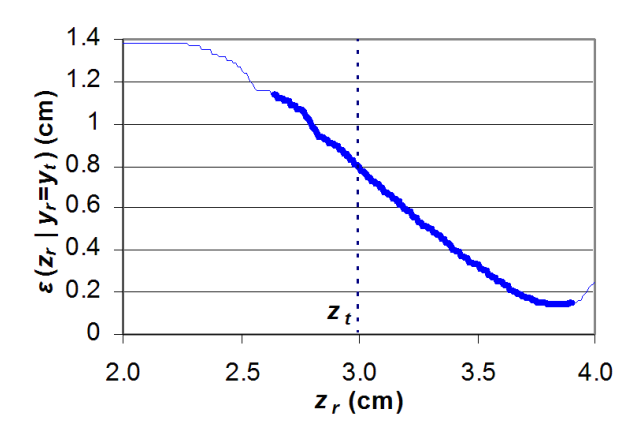


Figure 4.5. Needles should generally be inserted deeper than the target depth to compensate for tissue deformations and minimize placement error. The bold portion of the line denotes feasible seed placements inside the prostate.

4.4.3 Optimizing Insertion Height

For a 0.6 cm range around the target height $y_t = 1.5$ cm, we plot the estimated optimal insertion depth in figure 4.6(a) and the resulting error ε in figure 4.6(b). The planner finds $\mathbf{p_r}^*$ with $\varepsilon^* = 0.003$ cm (0.1% of prostate diameter) by inserting at height $y_r^* = 1.59$ cm to a depth $z_r^* = 3.80$ cm.

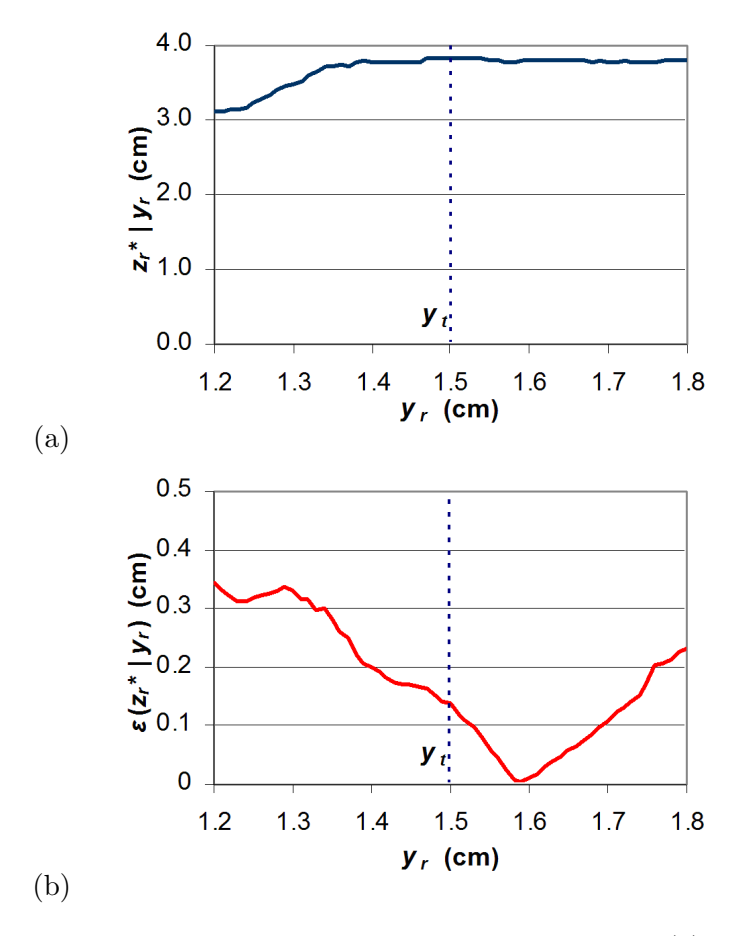


Figure 4.6. For all candidate insertion heights y_r , optimal depth z_r^* (a) and resulting error (b) are computed. Placement error is negligible for $\mathbf{p_r} = (1.59 \text{ cm}, 3.80 \text{ cm})$.

To test planner performance, we selected 12 sample points inside the prostate, shown by the crosses in the figure 4.7. We apply golden section search in the range $y_r \in (y_t - 0.2 \text{ cm}, y_t + 0.2 \text{ cm})$ with tolerance 0.01 cm for each target. Without planning, the average error was 0.59 cm (20% of prostate diameter) with a standard deviation of 0.10 cm. Using our planner, the average error was reduced in simulation to 0.002 cm (0.07% of prostate diameter) with a standard deviation of 0.004 cm.

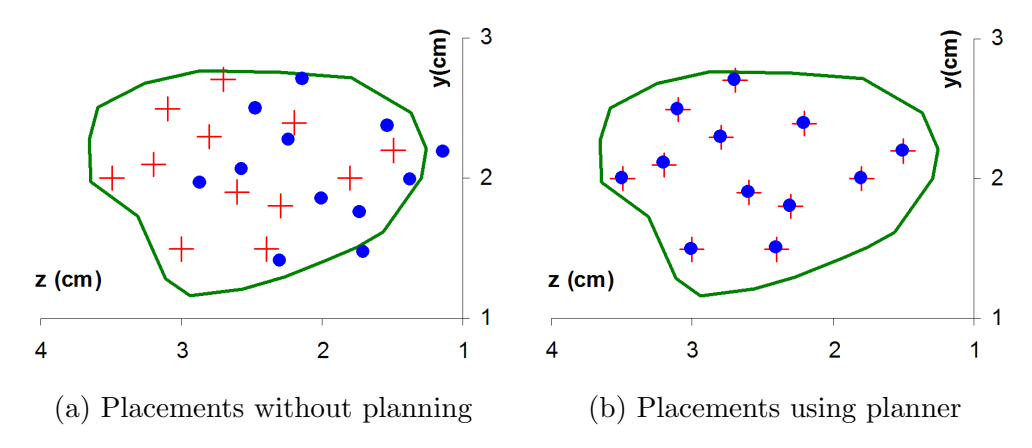


Figure 4.7. Twelve sample points were selected as targets marked "+" inside the prostate. Actual seed placements using simulation are marked "•". Lack of planning results in major placement errors averaging 20% of the prostate diameter (a), which will lead to a poor radioactive dose distribution. Placement error was neglible using the planner (b).

We implemented our needle insertion planner using C++ and tested it on a 750MHz Pentium III PC with 256MB RAM. The average time to compute optimal depth given height was 8.5 seconds and computing both optimal height and depth for each target took an average of 97.7 seconds.

4.5 Conclusion and Future Work

We applied our simulation from Chapter 2 as a component of a sensorless planning system for needle insertion procedures. Our sensorless planning method computes needle offsets to minimize needle placement error by compensating for predicted tissue deformations. The approach combines numerical optimization with soft tissue simulation. The effectiveness of the planner *in-vivo* will be dependent on the accuracy of the simulation of tissue deformations that occur during needle insertion for a specific patient.

Past work on patient-specific image-guided needle procedures uses local control to compensate for errors induced by tissue deformation but does not pre-operatively consider these effects [145]. Conversely, our sensorless planner searches for a globally optimal insertion plan but does not consider anomalies that may occur during execution. In the long run, we believe in combining these methods to create a pre-operative plan that is optimal under uncertainty and then use information from real-time imaging, when available, to correct deviations from the pre-operative plan.

Chapter 5

Motion Planning for Steerable

Needles

Advances in medical imaging such as X-ray fluoroscopy, ultrasound, and MRI are now providing physicians with real-time patient-specific information as they perform medical procedures such as extracting tissue samples for biopsies, injecting drugs for anesthesia, or implanting radioactive seeds for brachytherapy cancer treatment. These diagnostic and therapeutic medical procedures require insertion of a needle to a specific location in soft tissue.

We consider a new class of medical needles, composed of a flexible material and with a bevel-tip, that can be steered to targets in soft tissue that are inaccessible to traditional stiff needles [157, 159, 8, 13, 160, 158, 5]. Steerable needles are controlled by 2 degrees of freedom actuated at the needle base: insertion distance and bevel direction. Webster et al. experimentally demonstrated that, under ideal conditions, a flexible bevel-tip needle cuts a path of constant curvature in the direction of the bevel and the needle shaft bends to follow the path cut by the bevel tip [157]. In a plane, this nonholonomic constraint based on bevel direction is equivalent to a Dubins car that cannot go straight; it can only steer its wheels far left or far right.

The steerable needle motion planning problem is to determine a sequence of controls (in-

sertions and direction changes) so the needle tip reaches the specified target while avoiding obstacles and staying inside the workspace. Given a segmented medical image of the target, obstacles, and starting location, the feasible workspace for motion planning is defined by the soft tissues through which the needle can be steered. Obstacles represent tissues that cannot be cut by the needle, such as bone, or sensitive tissues that should not be damaged, such as nerves or arteries.

We consider motion planning for steerable needles in the context of an image-guided procedure: real-time imaging and algorithms are used to track the position and orientation of the needle tip in the tissue. Recently developed methods can provide this information for a variety of imaging modalities [41, 50]. X-ray fluoroscopy, a relatively low-cost imaging modality capable of obtaining images at regular discrete time intervals, is ideally suited for our application because it generates 2-D projection images from which the needle can be cleanly segmented [41]. In this chapter we consider motion plans in an imaging plane since the speed/resolution trade-off of 3-D imaging modalities is generally poor for 3-D real-time interventional applications.

Our approach to motion planning has four features particularly beneficial for medical planning problems. First, we explicitly consider uncertainty in the motion of the needle. Second, the planning formulation only requires parameters that can be directly extracted from images. Third, we can quickly compute the optimal needle insertion point. Fourth, intra-operative medical imaging can be combined with the pre-computed planning solution to permit optimal control of the needle in the operating room without requiring time-consuming intra-operative re-planning. We apply the method to generate motion plans for steerable needles to reach targets inaccessible to stiff needles and illustrate the importance of considering uncertainty during motion plan optimization.

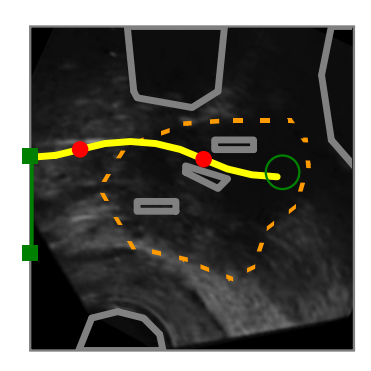
5.1 Uncertainty and Motion Planning

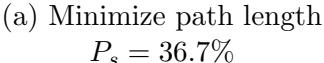
Clinicians performing medical needle insertion procedures must consider uncertainty in the needle's motion through tissue due to patient differences and the difficulty in predicting needle/tissue interaction. These sources of uncertainty may result in deflections of the needle's orientation, which is a type of slip in the motion of a Dubins car. Real-time imaging in the operating room can measure the needle's current position and orientation, but this measurement by itself provides no information about the effect of future deflections during insertion. We develop a new motion planning approach for steering flexible needles through soft tissue that explicitly considers uncertainty: our method formulates the planning problem as a Markov Decision Process (MDP) based on an efficient discretization of the state space, models motion uncertainty using probability distributions, and computes optimal controls (within error due to discretization) using infinite horizon Dynamic Programming (DP).

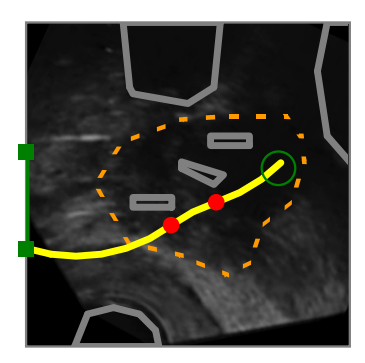
To define optimality for a needle steering plan, we introduce a new objective for image-guided motion planning: maximizing probability of success. In the case of needle steering, the needle is controlled until it reaches the target (success) or until failure occurs, where failure is defined as hitting an obstacle, exiting the feasible workspace, or reaching a state in which it is impossible to prevent the former two outcomes. Since the motion response of the needle is not deterministic, success of the procedure can rarely be guaranteed. Our objective function value for a particular plan has physical meaning: it is the probability that the needle insertion will succeed assuming optimal control of the needle. In addition to this intuitive interpretation of the objective, our formulation has a secondary benefit: all data required for planning can be measured directly from imaging data without requiring tweaking of user-specified parameters. Rather than assigning costs to insertion distance, needle rotation, etc., which are difficult to estimate or quantify, our method only requires the probability distributions of the needle response to each feasible control, which can be estimated from previously obtained images.

Solving the MDP using DP has key benefits particularly relevant for medical planning problems where feedback is provided at regular time intervals using medical imaging or other sensor modalities. Like a well-constructed navigation field, the DP solver provides an optimal control for any state in the workspace. We use the DP look-up table to automatically optimize the needle insertion point. Integrated with intra-operative medical imaging,

this DP look-up table can be used to optimally control the needle in the operating room without requiring costly intra-operative re-planning. Hence, the planning solution can serve as a means of control under real-time medical imaging.







(b) Maximize probability of success $P_s = 73.7\%$

Figure 5.1. Our motion planner computes controls (insertions and direction changes, indicated by dots) to steer the needle from an insertion entry region (vertical line on left between the solid squares) to the target (open circle) inside soft tissue, without touching critical areas indicated by polygonal obstacles in the imaging plane. The motion of the needle is not known with certainty; the needle tip may be deflected during insertion due to tissue inhomogeneities or other unpredictable soft tissue interactions. We explicitly consider this uncertainty to generate motion plans to maximize the probability of success, P_s , the probability that the needle will reach the target without colliding with an obstacle or exiting the workspace boundary. Relative to minimizing path length, our planner can generate longer paths with greater clearance from obstacles to maximize P_s .

In figure 5.1, we apply our motion planner in simulation to prostate brachytherapy, a medical procedure in which physicians implant radioactive seeds at precise locations inside the prostate under ultrasound image guidance to treat prostate cancer. In this ultrasound image of the prostate (segmented by a dotted line), obstacles correspond to bones, the rectum, the bladder, the urethra, and previously implanted seeds. Brachytherapy is currently performed using rigid needles; here we consider steerable needles capable of obstacle avoidance. We compare the output of our new method to previous work on shortest path planning for steerable needles [13]. Our method improves the expected probability of success by over 30% compared to shortest path planning, illustrating the importance of explicitly considering uncertainty in needle motion.

5.2 Related Work on Nonholonomic Motion Planning and MDP's

Nonholonomic motion planning has a long history in robotics and related fields [102, 103, 37, 105]. Past work has addressed deterministic curvature-constrained path planning where a mobile robot's path is, like a car, constrained by a minimum turning radius. Dubins showed that the optimal curvature-constrained trajectory in open space from a start pose to a target pose can be described from a discrete set of canonical trajectories composed of straight line segments and arcs of minimum radius of curvature [56]. Jacobs and Canny considered polygonal obstacles and constructed a configuration space for a set of canonical trajectories [81], and Agarwal et al. developed a fast algorithm for a shortest path inside a convex polygon [2]. For Reeds-Shepp cars with reverse, Laumond et el. developed a nonholonomic planner using recursive subdivision of collision-free paths generated by a lower-level geometric planner [104] and Bicchi et al. proposed a technique that provides the shortest path for circular unicycles [27]. Sellen developed a discrete state-space approach; his discrete representation of orientation using a unit circle inspired our discretization approach [141].

Our planning problem considers steerable needles currently under development that are subject to a *constant* magnitude turning radius rather than a *minimum* turning radius. Webster et al. showed experimentally that, under ideal conditions, steerable bevel-tip needles follow paths of constant curvature in the direction of the bevel tip [157], and that radius of curvature of the needle path is not significantly affected by insertion velocity [159].

Park et al. formulated the planning problem for steerable bevel-tip needles in stiff tissue as a nonholonomic kinematics problem based on a 3-D extension of a unicycle model and used a diffusion-based motion planning algorithm to numerically compute a path [125]. Park's method searches for a feasible path in full 3-D space using continuous control, but it does not consider obstacle avoidance or the uncertainty of the response of the needle to insertion or direction changes, both of which are emphasized in our method.

MDP's are ideally suited for medical planning problems because of the variance in characteristics between patients and the necessity for clinicians to make decisions at discrete time intervals based on limited known information. In the context of medical procedure planning, MDP's have been developed to assist in timing decisions for liver transplants [4], discharge of severe sepsis cases [91], and start dates for HIV drug cocktail treatment [143].

Past work has also addressed insertion planning for a different type of steerable needle: slightly flexible symmetric-tip needles that are guided by translating and orienting the needle base to explicitly deform surrounding tissue, causing the needle to follow a curved path [54, 69]. DiMaio and Salcudean developed a planning approach that guides this type of needle around point obstacles with oval-shaped potential fields [54]. Glozman and Shoham also address symmetric-tip needles and approximate the tissue using springs [69].

5.3 Motion Planning Problem Definition

Steerable bevel-tip needles are controlled by 2 degrees of freedom actuated at the needle base: insertion distance and rotation angle about the needle axis. Insertion pushes the needle deeper into the tissue, while rotation re-orients the bevel at the needle tip. For a sufficiently flexible needle, Webster et al. experimentally demonstrated that rotating the needle base will change the bevel direction without changing the needle's position in the tissue [157]. In the plane, the needle base can be rotated 180° about the insertion axis at the base so the bevel points in either the bevel-left or bevel-right direction. When inserted, the asymmetric force applied by the bevel causes the needle to bend and follow a curved path through the tissue [124, 157]. Under ideal conditions, the curve will have a constant radius of curvature r, which is a property of the needle and tissue. We assume the tissue is stiff relative to the needle and that the needle is thin, sharp, and low-friction so the tissue does not significantly deform. While the needle can be partially retracted and re-inserted, the needle is likely to follow the path in the tissue cut by the needle prior to retraction. Hence, we only consider insertion, not retraction, of the needle in this chapter.

We define the workspace as a 2-D rectangle of depth z_{max} and height y_{max} . We do not consider motion by the needle out of the imaging plane. Obstacles in the workspace are defined by (possibly nonconvex) polygons. The obstacles can be expanded using a

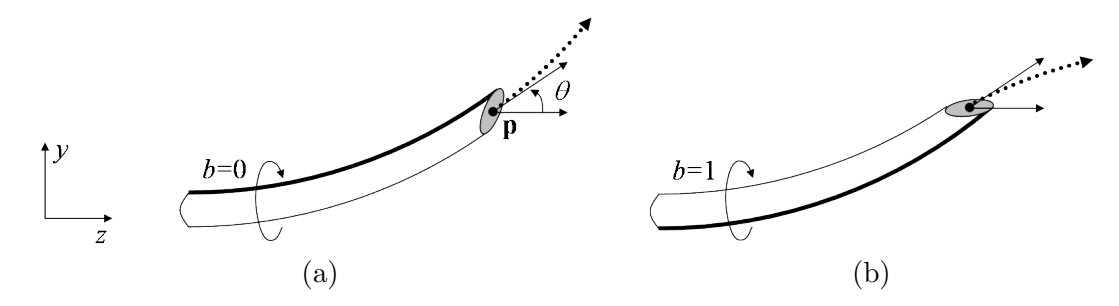


Figure 5.2. The state of a steerable needle during insertion is characterized by tip position \mathbf{p} , tip orientation angle θ , and bevel direction b (a). Rotating the needle about its base changes the bevel direction but does not affect needle position (b). The needle will cut soft tissue along an arc (dotted vector) based on bevel direction.

Minkowski sum to specify a minimum clearance [105]. The target region is defined by a circle with center point \mathbf{t} and radius r_t .

As shown in figure 5.2, the state w of the needle during insertion is fully characterized by the needle tip's position $\mathbf{p} = (p_y, p_z)$, orientation angle θ , and bevel direction b, where b is either bevel-left (b=0) or bevel-right (b=1).

We assume imaging occurs at discrete time intervals and the motion planner obtains needle tip position and orientation information only at these times. Between images, we assume the needle moves at constant velocity and is inserted a distance δ . In our model, direction changes can only occur at discrete decision points separated by the insertion distance δ . One of two controls, or actions, u can be selected at any decision point: insert the needle a distance δ (u = 0), or change direction and insert a distance δ (u = 1).

During insertion, the needle tip orientation may be deflected by inhomogeneous tissue, small anatomical structures not visible in medical images, or local tissue displacements. Additional deflection may occur during direction changes due to stiffness along the needle shaft. These deflections are due to an unknown aspect of the tissue structure or needle/tissue interaction, not errors in measurement of the needle's orientation, and can be considered a type of noise parameter in the plane. We model uncertainty in needle motion due to such deflections using probability distributions. The orientation angle θ may be deflected by some angle β , which we model as normally distributed with mean 0 and standard deviations σ_i for insertion (u = 0) and σ_r for direction changes followed by insertion (u = 1). Since σ_i

and σ_r are properties of the needle and tissue, we plan in future work to automatically estimate these parameters by retrospectively analyzing images of needle insertion.

The goal of motion planning is to compute an optimal control u for every state w in the workspace to maximize the probability of success P_s . We define $P_s(w)$ to be the probability of success given that the needle is currently in state w. If the position of state w is inside the target, $P_s(w) = 1$. If the position of state w is inside an obstacle, $P_s(w) = 0$. Given a control u for some other state w, the probability of success will depend on the response of the needle to the control (the next state) and the probability of success for that next state. The expected probability of success is $P_s(w) = E[P_s(v)|w,u]$, where the expectation is over v, a random variable for the next state. The goal of motion planning is to compute an optimal control u for every state w:

$$P_s(w) = \max_{u} \{ E[P_s(v)|w, u] \}.$$
 (5.1)

5.4 Motion Planning Method

5.4.1 Problem Formulation

To evaluate Eq. 5.1, we approximate needle state $w = \{\mathbf{p}, \theta, b\}$ using a discrete representation. To make this approach tractable, we must round \mathbf{p} and θ without generating an unwieldy number of states while simultaneously bounding error due to discretization. We describe our approximation approach, which results in N discrete states, in section 5.4.2.

For N discrete states, the motion planning problem is to determine the optimal control u_i for each state i = 1, ..., N. We re-write Eq. 5.1 using the discrete approximation and expand the expected value to a summation:

$$P_s(x_i) = \max_{u_i} \left\{ \sum_{j=1}^{N} P_{ij}(u_i) P_s(x_j) \right\},$$
 (5.2)

where $P_{ij}(u_i)$ is the probability of entering state x_j after executing control u_i at current state x_i .

We observe that the needle steering motion planning problem is a type of MDP. In

particular, Eq. 5.2 has the form of the Bellman equation for a stochastic shortest path problem [25]:

$$J^*(x_i) = \max_{u_i} \sum_{j=1}^{N} P_{ij}(u_i) \left(g(x_i, u_i, x_j) + J^*(x_j) \right). \tag{5.3}$$

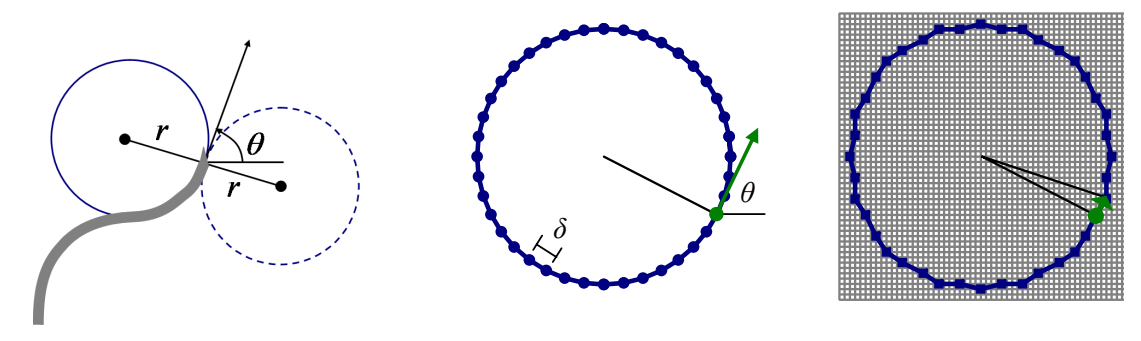
where $g(x_i, u_i, x_j)$ is a "reward" for transitioning from state x_i to x_j after control u_i . In our case, $g(x_i, u_i, x_j) = 0$ for all x_i , u_i , and x_j , and $J^*(x_i) = P_s(x_i)$. Stochastic shortest path problems of this form can be optimally solved using infinite horizon DP, as we describe in section 5.4.3.

5.4.2 State Space Discretization

Our discretization of the planar workspace is based on a grid of points with a spacing Δ horizontally and vertically. We approximate a point $\mathbf{p} = (p_y, p_z)$ by rounding to the nearest point $\mathbf{q} = (q_y, q_z)$ on the grid. For a rectangular workspace bounded by depth z_{max} and height y_{max} , this results in $N_s = \lfloor z_{max} y_{max}/\Delta^2 \rfloor$ position states aligned at the origin.

Rather than directly approximating θ by rounding, which would incur a cumulative error with every transition, we take advantage of discrete insertion distances δ . We define a control circle of radius r, the radius of curvature of the needle. Each point \mathbf{c} on the control circle represents an orientation θ of the needle, where θ is the angle of the tangent of the circle at \mathbf{c} with respect to the z-axis. The needle will trace an arc of length δ along the control circle in a counter-clockwise direction for b=0 and in the clockwise direction for b=1. Direction changes correspond to rotating the point \mathbf{c} by 180° about the control circle origin and tracing subsequent insertions in the opposite direction, as shown in figure 5.3(a). Since the needle traces arcs of length δ , we divide the control circle into N_c arcs of length $\delta = 2\pi r/N_c$. The endpoints of the arcs generate a set of N_c control circle points, each representing a discrete orientation state, as shown in figure 5.3(b). We require that N_c is a multiple of 4 to facilitate the orientation state change after a direction change.

At each position on the Δ grid, the needle may be in any of the N_c orientation states. To define transitions for each orientation state, we overlay the control circle on a regular grid of spacing Δ and round the positions of the control circle points to the nearest grid



(a) Needle tracing control circle

(b) Control circle

(c) Rounded control circle

Figure 5.3. A needle in the bevel-left direction with orientation θ is tracing the solid control circle with radius r (a). A direction change would result in tracing the dotted circle. The control circle is divided into $N_c = 40$ discrete arcs of length δ (b). The control circle points are rounded to the nearest point on the Δ -density grid, and transitions for insertion of distance δ are defined by the vectors between rounded control circle points (c).

point, as shown in figure 5.3(c). The displacements between rounded control circle points encode the transitions of the needle tip. This discretization results in 0 discretization error in orientation when the needle is controlled at δ intervals.

Using this discretization, a needle state $w = \{\mathbf{p}, \theta, b\}$ can be approximated as a discrete state $s = \{\mathbf{q}, \Theta, b\}$, where $\mathbf{q} = (q_y, q_z)$ is the discrete point closest to \mathbf{p} on the Δ -density grid and Θ is the integer index of the discrete control circle point with tangent angle closest to θ . The total number of discrete states is $N = 2N_sN_c$.

Deterministic paths designated using this discrete representation of state will incur error due to discretization, but the error is bounded. At any decision point, the position error due to rounding to the Δ workspace grid is $E_0 = \Delta \sqrt{2}/2$. When the bevel direction is changed, a position error is also incurred because the distance in centers of the original control circle and the center of the control circle after the direction change will be in the range $2r \pm \Delta \sqrt{2}$. Hence, for a needle path with h direction changes, the final orientation is precise but the error in position is bounded above by $E_h = h\Delta\sqrt{2} + \Delta\sqrt{2}/2$.

Due to motion uncertainty, actual needle paths will not always exactly trace the control circle. The deflection angle β defined in section 5.3 must also be approximated as discrete. We define discrete transitions from a state x_i , each separated by an angle of deflection of $\alpha = 360^{\circ}/N_c$, and store the transition probability in $P_{ij}(u)$. In this chapter, we model β

using a normal distribution with mean 0 and standard deviation σ_i or σ_r , and compute the probability for each discrete transition by integrating the corresponding area under the normal curve, as shown in figure 5.4. We set the number of discrete transitions N_{p_i} such that the areas on the left and right tails of the normal distribution sum to less than 1%. The left and right tail probabilities are added to the left-most and right-most transitions, respectively.

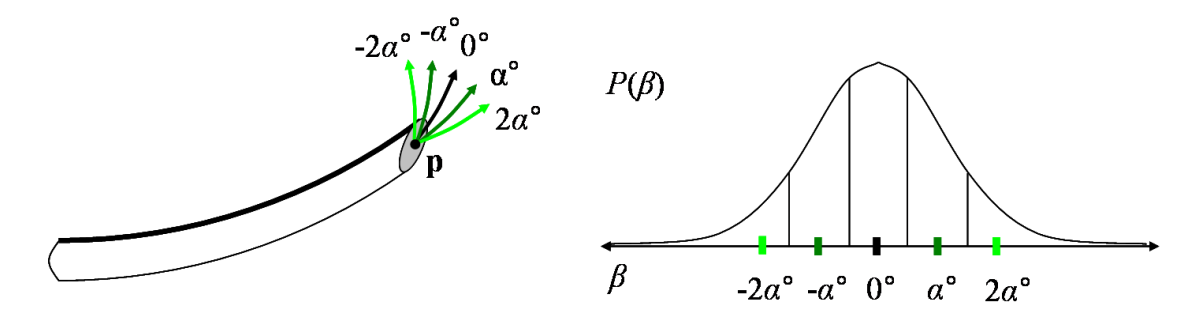


Figure 5.4. When the needle is inserted, the insertion angle θ may be deflected by some angle β . We model the probability distribution of β using a normal distribution with mean 0 and standard deviation σ_i for insertion or σ_r for direction change. For a discrete sample of deflections ($\beta = \{-2\alpha, -\alpha, 0, \alpha, 2\alpha\}$), we obtain the probability of each deflection by integrating the corresponding area under the normal curve.

Certain states and transitions must be handled as special cases. States inside the target region and states inside obstacles are absorbing states. If the transition arc from feasible state x_i exits the workspace or intersects an edge of a polygonal obstacle, a transition to an obstacle state is used.

5.4.3 Optimization Using Infinite Horizon Dynamic Programming

Infinite horizon dynamic programming is a type of dynamic programming in which there is no finite time horizon [25]. For stationary problems, this implies that the optimal control at each state is purely a function of the state without explicit dependence on time. In the case of needle steering, once a state transition is made, the next control is computed based on the current position, orientation, and bevel direction without explicit dependence on past controls.

To solve the infinite horizon DP problem defined by the Bellman Equation (equation

5.3), we use the value iteration algorithm [25], which iteratively updates $P_s(x_i)$ for each state i by evaluating Eq. 5.2. This generates a DP look-up table containing the optimal control u_i and the probability of success $P_s(x_i)$ for i = 1, ..., N.

Termination of the algorithm is guaranteed in N iterations if the transition probability graph corresponding to some optimal stationary policy is acyclicBertsekas2000. Violation of this requirement will be rare in motion planning since it implies that an optimal control sequence results in a path that, with probability greater than 0, loops and passes through the same point at the same orientation more than once. Each iteration requires matrix-vector multiplication. To improve performance, we take advantage of the sparsity of the matrices $P_{ij}(u)$ for u = 0 and u = 1. Although $P_{ij}(u)$ has N^2 entries, each row of $P_{ij}(u)$ has only k nonzero entries, where k << N since the needle will only transition to a state j in the spatial vicinity of state i. Hence, $P_{ij}(u)$ has at most kN nonzero entries. By only accessing nonzero entries of $P_{ij}(u)$ during computation, each iteration of the value iteration algorithm requires only O(kN) rather than $O(N^2)$ time and memory. Thus, the total algorithm's complexity is $O(kN^2)$. To further improve performance, we terminate value iteration when the maximum change ϵ over all states is less than 10^{-3} , which in our test cases occurred in far fewer than N iterations, as described in section 5.5.

5.5 Computational Results

We implemented the motion planner in C++ and tested it on a 2.21 GHz Athlon 64 PC. In figure 5.1, we set the needle radius of curvature r=5.0, defined the workspace by $z_{max}=y_{max}=10$, and used discretization parameters $N_c=40$, $\Delta=0.1$, and $\delta=0.785$. The resulting DP problem contained N=800,000 states. In all further examples, we set r=2.5, $z_{max}=y_{max}=10$, $N_c=40$, $\Delta=0.1$, and $\delta=0.393$, resulting in N=800,000 states.

Optimal plans and probability of success P_s depend on the level of uncertainty in needle motion. As shown in figure 5.1 and figure 5.5, explicitly considering the variance of needle motion significantly affects the optimal plan relative to shortest path plan generated under

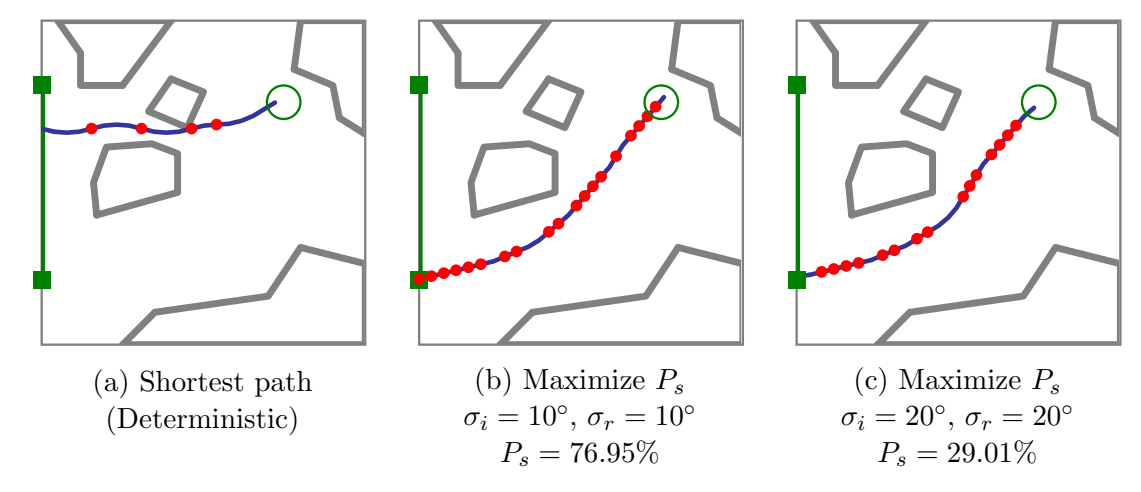


Figure 5.5. As in figure 5.1, optimal plans maximizing the probability of success P_s illustrate the importance of considering uncertainty in needle motion. The shortest path plan passes through a narrow gap between obstacles (a). Since maximizing P_s explicitly considers uncertainty, the optimal expected path has greater clearance from obstacles, decreasing the probability that large deflections will cause failure to reach the target. Here we consider medium (b) and large (c) variance in tip deflections for a needle with smaller radius of curvature than in figure 5.1.

the assumption of deterministic motion. We also vary the variance during direction changes independently from the variance during insertions without direction changes. Optimal plans and probability of success P_s are highly sensitive to the level of uncertainty in needle motion due to direction changes. As shown in figure 5.6, the number of direction changes decreases as the variance during direction changes increases.

By examining the DP look-up table, we can optimize the initial insertion location, orientation, and bevel direction, as shown in figures 5.1, 5.5, and 5.6. In these examples, the set of feasible start states was defined as a subset of all states on the left edge of the workspace. By linearly scanning the DP look-up table, the method identifies the bevel direction b, insertion point (height y on the left edge of the workspace), and starting orientation angle θ (which varies from -90° to 90°) that maximizes probability of success, as shown in figure 5.7.

Integrating intra-operative medical imaging with the pre-computed DP look-up table could permit optimal control of the needle in the operating room without requiring costly intra-operative re-planning. We demonstrate the potential of this approach using simulation of needle deflections based on normal distributions with mean 0 and standard deviations

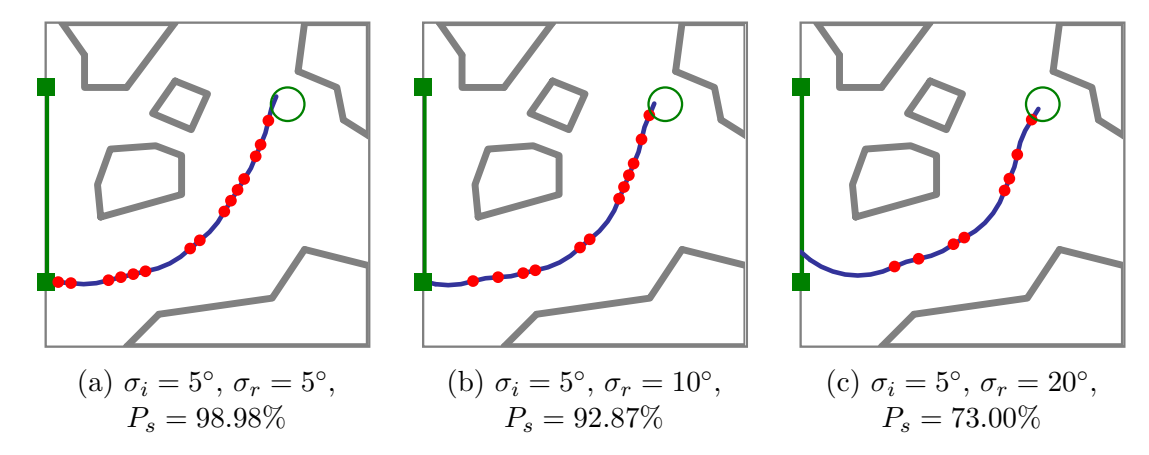
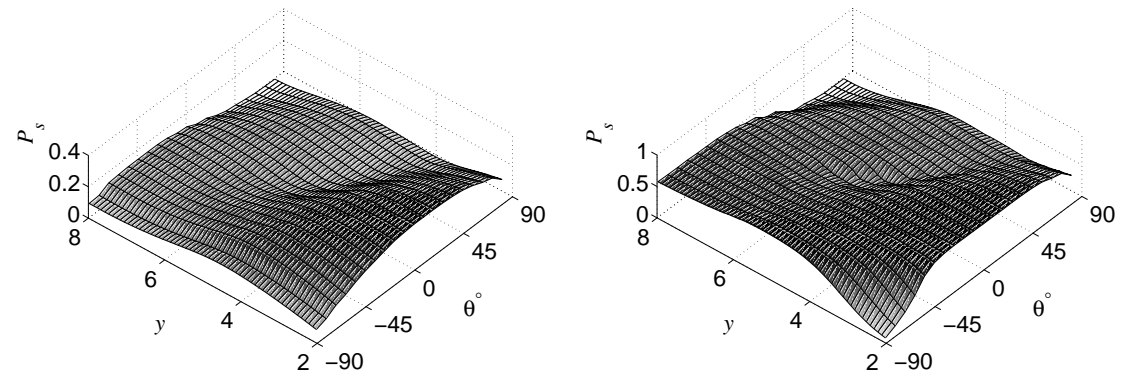


Figure 5.6. Optimal plans demonstrate the importance of considering uncertainty in needle motion, where σ_i and σ_r are the standard deviations of needle tip deflections that can occur during insertion and direction changes, respectively. For higher σ_r relative to σ_i , the optimal plan includes fewer direction changes. Needle motion uncertainty at locations of direction changes may be substantially higher than uncertainty during insertion due to transverse stiffness of the needle.

 $\sigma_i = 5^{\circ}$ and $\sigma_r = 20^{\circ}$ in figure 5.8. After each insertion distance δ , we assume the needle tip is localized in the image. Based on the DP look-up table, the needle is either inserted or the bevel direction is changed. The effect of uncertainty can be seen as deflections in the path, i.e., locations where the tangent of the path abruptly changes. Since $\sigma_r > \sigma_i$, deflections are more likely to occur at points of direction change. In practice, clinicians could monitor P_s , insertion length, and self-intersection while performing needle insertion.

As defined in section 5.4.3, the computational complexity of the motion planner is $O(kN^2)$. Fewer than 300 iterations were required for each example, with fewer iterations required for smaller σ_i and σ_r . In all examples, the number of transitions per state $k \leq 25$. Computation time to solve the MDP for the examples ranged from 67 sec to 110 sec on a 2.21 GHz AMD Athlon 64 PC, with higher computation times required for problems with greater variance, due to the increased number of transitions from each state. As computation only needs to be performed at the pre-procedure stage, we believe this computation time is reasonable for the intended applications. Intra-operative computation time is effectively instantaneous since only a memory access to the DP look-up table is required to retrieve the optimal control after the needle has been localized in imaging.



- (a) Optimization surface for figure 5.5(c)
- (b) Optimization surface for figure 5.6(c)

Figure 5.7. The optimal needle insertion location y, angle θ , and bevel direction b are found by scanning the DP look-up table for the feasible start state with maximal P_s . Here we plot optimization surfaces for b = 0. The low regions correspond to states from which the needle has high probability of colliding with an obstacle or exiting the workspace, and the high regions correspond to better start states.

5.6 Conclusion and Future Work

We developed a new motion planning approach for steering flexible needles through soft tissue that explicitly considers uncertainty: the planner computes optimal controls to maximize the probability that the needle will reach the desired target. Motion planning for steerable needles, which can be controlled by 2 degrees of freedom at the needle base (bevel direction and insertion distance), is a variant of nonholonomic planning for a Dubins car with no reversals, binary left/right steering, and uncertainty in motion direction.

Given a medical image with segmented obstacles and target, our method formulates the planning problem as a Markov Decision Process (MDP) based on an efficient discretization of the state space, models motion uncertainty using probability distributions, and computes controls to maximize the probability of success using infinite horizon DP. We implemented the motion planner and ran test problems of 800,000 states on a 2.21 GHz Athlon 64 PC. The method generated motion plans for steerable needles to reach targets inaccessible to stiff needles and illustrated the importance of considering uncertainty in needle motion, as shown in figures 5.1, 5.5, and 5.6.

Our approach has key features particularly beneficial for medical planning problems.

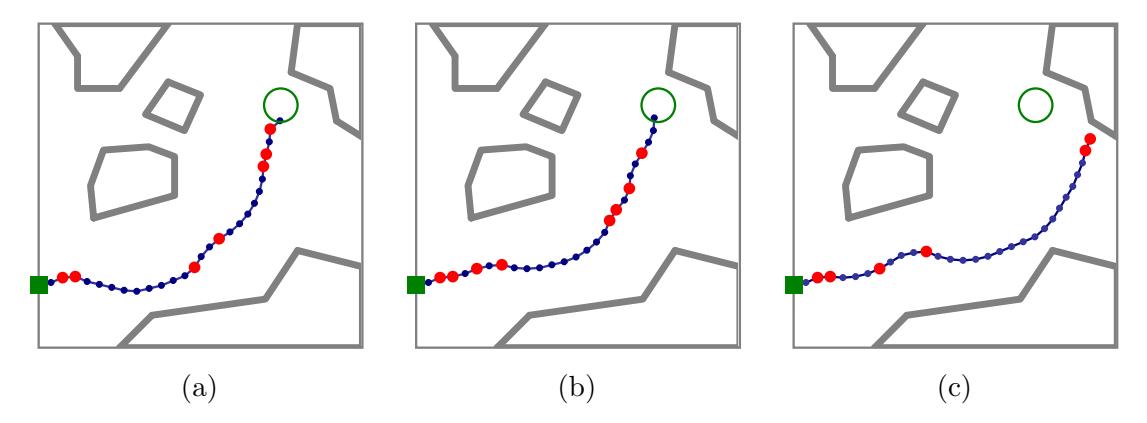


Figure 5.8. Three simulated image-guided needle insertion procedures from a fixed starting point with needle motion uncertainty standard deviations of $\sigma_i = 5^{\circ}$ during insertion and $\sigma_r = 20^{\circ}$ during direction changes. After each insertion distance δ , we assume the needle tip is localized in the image and identified using a dot. Based on the DP look-up table, the needle is either inserted (small dots) or a direction change is made (large dots). The effect of uncertainty can be seen as deflections in the path, i.e., locations where the tangent of the path abruptly changes. Since $\sigma_r > \sigma_i$, deflections are more likely to occur at points of direction change. In all cases, $P_s = 72.35\%$ at the initial state. In (c), multiple deflections and the nonholonomic constraint on needle motion prevent the needle from reaching the target.

First, the planning formulation only requires parameters that can be directly extracted from images (the variance of needle orientation after insertion with or without direction change). Second, we can locate the optimal needle insertion point by examining the DP look-up table of optimal controls for every needle state, as demonstrated in figure 5.7. Third, intra-operative medical imaging can be combined with the pre-computed DP look-up table to permit optimal control of the needle in the operating room without requiring time-consuming intra-operative re-planning, as shown in figure 5.8.

In future work, we plan to extend the motion planner to 3-D. Although the mathematical formulation can be naturally extended, substantial effort will be required to specify 3-D state transitions and improve solving methods to handle the larger state space. We also plan to develop automated methods to estimate curvature and variance properties from images and explore the inclusion of multiple tissue types in the workspace with different needle/tissue interaction properties.

Our motion planner has implications outside the needle steering domain. We can directly extend the method to motion planning problems with a bounded number of discrete

turning radii where current position and orientation can be measured but future motion response to controls is uncertain. For example, mobile robots subject to motion uncertainty with similar properties can receive periodic "imaging" updates from GPS or satellite images. Optimization of "insertion location" could apply to automated guided vehicles in a factory setting, where one machine is fixed but a second machine can be placed to maximize the probability that the vehicle will not collide with other objects on the factory floor. By identifying a relationship between needle steering and infinite horizon DP, we developed a motion planner capable of rigorously computing plans that are optimal in the presence of uncertainty.

Chapter 6

Dose Optimization for

High-Dose-Rate Brachytherapy

High-dose-rate (HDR) brachytherapy is a type of radiation treatment for cancer. In this procedure, a physician guides radioactive sources through catheters that have been inserted inside or near the cancerous cells. The goal is to provide a high radioactive dose to treat the tumor while not significantly damaging surrounding healthy tissues. HDR brachytherapy has been successfully used for treating many types of cancer, including prostate cancer [129], cervical cancer [107], and breast cancer [77].

When treating cancer using radiation, physicians desire dose distributions that conform to patient anatomy and satisfy dose prescriptions for the tumor target and nearby critical organs [76]. Using medical images of patient anatomy and estimates of tumor location, physicians prescribe radiation dose requirements for cancerous tumors and surrounding tissues. A sample slice of a CT scan used for this purpose for a prostate cancer patient case is shown in figure 6.1. The goal is then to select dwell times for the radioactive source inside the catheters to generate a dose distribution that satisfies the clinical criteria as best as possible. This goal can be formulated as an optimization problem: compute dwell times to minimize deviation from prescribed dose subject to dwell position and dose feasibility constraints.

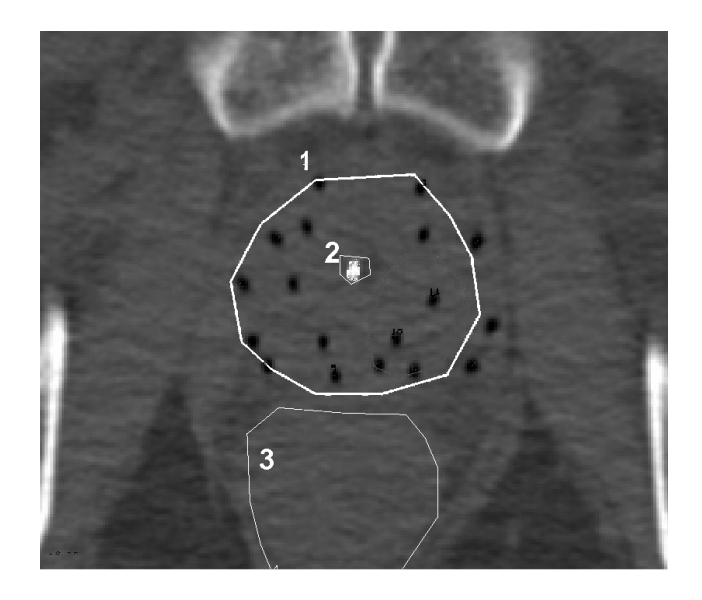


Figure 6.1. Transverse slice of a CT scan with white contours of the prostate (1), urethra (2), and rectum (3). The catheters are marked with black dots.

We re-introduce linear programming into dose optimization by developing a fast and exact method to optimize radioactive source locations and dwell times for HDR brachytherapy cancer treatment. The method uses the objective and clinical criteria framework of Inverse Planning by Simulated Annealing (IPSA), an approach developed by Lessard and Pouliot in 2000 that has been used in the treatment of over a thousand patients [108, 107, 106]. By formulating the HDR brachytherapy dose optimization problem as a linear program, we enable the fast computation of mathematically optimal solutions.

In this chapter, we present our linear programming formulation and apply the method to a sample of 20 prostate cancer patient cases [11, 12]. We then quantitatively compare the mathematically optimal dwell times solutions for HDR brachytherapy treatment obtained using the LP method to the solutions currently being obtained clinically using simulated annealing (SA), a probabilistic method that is not guaranteed to return an optimal solution in finite computation time. We show that the LP method resulted in significantly improved objective function values compared to SA, but the dose distributions produced by the dwell times solutions were clinically equivalent as measured by standard dosimetric indices with a 2% threshold.

6.1 Introduction to HDR Brachytherapy and Dose Optimization

High-dose-rate (HDR) brachytherapy is a type of radiation treatment for cancer in which a physician guides radioactive sources through catheters that have been inserted inside or near the cancerous cells. The specifics of the procedure depend on the cancer site. For the case of the HDR brachytherapy for prostate cancer, the physician commonly implants 14 to 18 catheters in the prostate through the perineum under ultrasound guidance. The physician obtains an image (usually CT scan or MRI) of the catheters and the surrounding tissue, which is used to specify dose prescriptions for the patient anatomy. The catheters are then attached to an HDR Remote Afterloader for treatment delivery. The afterloader, a type of robot, moves a single radioactive source, typically 4.5 mm long and 0.9 mm in diameter containing ¹⁹²Ir, inside each catheter, stopping temporarily at predetermined dwell locations. By adjusting the length of time (dwell time) that the source remains at any location within a catheter (dwell position), it is possible to generate a wide variety of dose distributions.

To address the dose optimization problem, Lessard and Pouliot developed Inverse Planning by Simulated Annealing (IPSA) [108, 107, 106]. IPSA has been used in the treatment planning of over a thousand patients at UCSF since 2000 and has been independently evaluated by different American and European institutions [98, 111, 39, 113, 47, 150].

A complete description of IPSA and its clinical applications was recently published [130]. Only the elements required for the present work are described here. Using hand-segmented boundaries of the dominant intraprostatic lesions and nearby organs [129], the software generates a discrete sample of dose calculation points inside and on the boundary of the tissue types. For dose calculation points of each tissue type, IPSA permits the physician to prescribe unique dose ranges as well as penalty costs that grow linearly when actual dose violates of the prescribed dose ranges. Setting dwell times to minimize dose penalty costs rather than using rigid dose constraints guarantees that the method will find an achievable solution. IPSA defines an objective function equal to a weighted sum of penalty costs at

dose calculation points given the dwell times. In the IPSA framework, the mathematically optimal solution is the solution of dwell times that globally minimizes the objective function. IPSA's single objective function assumes that the clinician has specified desirable dose penalty costs and generates a single dwell times solution, in contrast to multi-objective optimization formulations that consider the weights as variables and generate a Pareto front of solutions [100, 101].

The current version of IPSA software uses simulated annealing (SA) to compute dwell times to minimize the objective function. The computation time for a typical case is about 10 seconds on PC with a 3.6 GHz Intel Xeon processor (Nucletron's Masterplan Station). The computation time includes the automatic selection of the active dwell positions, the generation of the dose calculation points, the generation of a look-up dose-rate table, and 100,000 simulated annealing iterations. SA applies a random search with the ability to escape local minima and offers a statistical guarantee to converge asymptotically to the global minimum [66, 155, 1]. The longer the SA algorithm searches for a solution, the higher the probability that the optimal solution is found. Although this method has worked well in clinical practice using 100,000 iterations, there previously was no general quantitative information available regarding the closeness to mathematical optimality of the solutions obtained using simulated annealing, a probabilistic method that cannot guarantee the achievement of a global minimum within a finite computation time.

6.2 Linear Programming for HDR Brachytherapy

Our primary contribution is to take the well-established dose optimization problem defined by IPSA and show that it can be exactly formulated as a linear programming (LP) problem. Because the global minimum for an LP problem can be computed exactly and deterministically using pre-existing algorithms, this formulation provides strong performance guarantees for cost minimization: one can rapidly find the minimum cost solution for any patient case and clinical criteria parameters. LP does not require setting parameters specific to the optimization method, such as stopping criteria or pseudo-temperatures for SA

or mutation probabilities for GA [100, 169, 101]. This allows clinicians to customize dose prescriptions and penalty costs based on medical considerations without concern about their effect on the convergence of the optimization method. Unlike other deterministic algorithms such as local search [108], the LP method will never be trapped at sub-optimal solutions of IPSA's objective function. Since the LP solution is guaranteed to globally minimize the objective function, it provides a precise baseline for evaluating solutions currently being obtained clinically by probabilistic methods such as SA.

Our second contribution is to quantitatively compare the dwell times solutions for HDR treatment currently being obtained clinically using simulated annealing (SA) to the mathematically optimal solutions obtained using LP. With a sample of 20 prostate cancer patient cases, we show that the LP method resulted in significantly improved objective function values compared to SA, but the dose distributions produced by the dwell times solutions were clinically equivalent as measured by standard dosimetric indices.

A linear programming problem is defined by an objective function and constraints that are linear functions of the variables. An LP problem can be solved using the Simplex algorithm, a global deterministic optimization method that considers the geometric polyhedron defined by the linear constraints and systematically moves along edges of the polyhedron to new feasible solutions (represented as vertices of the polyhedron) with successively better values of the objective function until the optimum is reached [118]. In 1990, Renner et al. was the first group to propose a linear programming formulation for HDR brachytherapy dose optimization. Their method minimizes the time the source is irradiating tissue subject to a minimum dose constraint for a set of points in the target volume [132]. Kneschaurek et al. extended this method to permit the specification of dose ranges using rigid constraints for both minimum and maximum dose [90]. Jozsef et al. also used rigid constraints on dose range and minimized the maximum deviation from a prescribed dose constant at dose calculation points [84]. However, a solution of dwell times that results in a dose distribution that satisfies the rigid constraints may not be physically realizable. By defining the dwell times as variables and defining rigid linear constraints on dose, these previous approaches formulated the LP problem in a manner that does not guarantee the output of a solution since no feasible solution may exist. Finding a clinically realizable solution in such cases necessitates arbitrarily removing some rigid dose constraints, which requires substantial human intervention.

Our new linear programming (LP) formulation combines the advantages of IPSA's cost functions and extensive clinical validation with the benefits of deterministic global optimization for cost minimization. We show that the new LP method computes in finite time the mathematically optimal solution for dwell times to generate the best achievable dose distribution given the clinical objectives and the pre-optimization data generated by IPSA (active dwell positions, dose calculation points, and dose rate look-up table). We applied both SA and the new LP method to 20 prostate cancer patient cases and evaluated improvement of results using objective function values and standard dosimetric indices.

6.2.1 Patient Data Input

The input to the method are 3-D images of the tissues surrounding the tumor. We assume anatomical structures corresponding to b tissue types are segmented, including the clinical target volume (CTV) and critical organs (CO). We also assume the catheters are segmented. From the segmented anatomical structures, we use IPSA to select the active dwell positions and generated a set of m dose calculation points for which the optimization methods will calculate dose. The dose calculation points are distributed based on the anatomy and the implant in order to represent an accurate measurement of the clinical objectives [106]. For each contoured volume, IPSA uses two categories of dose calculation points: "surface" and "volume." This results in q=2b dose calculation point types: "surface" and "volume" for the b segmented tissue types. For each tissue type, adjusting the dose to "surface" dose calculation points controls the dose coverage and conformality while adjusting the dose to "volume" dose calculation points controls the dose homogeneity [76].

6.2.2 Dose Calculation

Dwell positions are defined as points along catheters at which a source can be placed for a non-zero interval of time. The n active dwell positions were selected by IPSA. We define the dwell time of a source at dwell position j by t_j . A dwell time of 0 corresponds to skipping past a dwell position. The dwell times t_j are the variables that will be set to produce a dose distribution that satisfies the clinical criteria as best as possible.

We calculate the dose-rate contribution d_{ij} of a dwell position j to a dose calculation point i as specified in the AAPM TG-43 dosimetry protocol [119, 133]. The dose-rate contribution is the energy imparted by the radioactive source into an absorbing material (the tissue) per unit time and has units cGy/sec, where 1 gray (Gy) equals 1 joule per kilogram. The dose-rate contribution is a function of r_{ij} , the distance between the dwell position j and the dose calculation point i. It also depends on the radioactive material used in the source, which was ¹⁹²Ir. Since small differences in the dose calculation may affect the outcome of the optimization, we use the look-up dose-rate table calculated by IPSA as an input for the LP method.

The dose contribution of a dwell position j to a dose calculation point i is computed by multiplying the dose-rate contribution d_{ij} by the dwell time t_j . The dose D_i at a dose calculation point i, which has units of cGy, is calculated by summing the dose contribution from each dwell position.

$$D_i = \sum_{j=1}^n d_{ij} t_j.$$

The dose D_i has units of cGy, which describes the energy imparted by radiation into a unit mass of tissue.

6.2.3 Clinical Criteria

After contouring, the physician prescribes dose ranges for each anatomical structure. The dose ranges used in this study, listed in Table 6.1, are typical values clinically used at the UCSF Comprehensive Cancer Center for treating prostate cancer [76]. This includes the

minimum dose D_s^{min} and maximum dose D_s^{max} for each dose calculation point type s. For a dose calculation point i of type s, the desired dose D_{si} should satisfy $D_s^{min} \leq D_{si} \leq D_s^{max}$.

\overline{s}	Dose calculation point type	D_s^{min} (cGy)	M_s^{min}	D_s^{max} (cGy)	M_s^{max}
1	Prostate (surface)	950	100	1425	100
2	Prostate (volume)	950	100	1425	30
3	Urethra (surface)	950	100	1140	30
4	Urethra (volume)	950	100	1140	30
5	Rectum (surface)	0	0	475	20
6	Rectum (volume)	0	0	475	20
7	Bladder (surface)	0	0	475	20
8	Bladder (volume)	0	0	475	20

Table 6.1. Clinical criteria parameters for dose penalty cost functions for a typical prostate cancer case.

In practice, it may not be physically possible to provide a radioactive dose in the physician specified range for every dose calculation point in the 3-D volume. Hence, the physician also specifies a "penalty" for any point for which the clinical criteria is not satisfied. If the actual dose is below or above the prescribed range, the penalty increases linearly at rates M_s^{min} and M_s^{max} , respectively. Adjustment of M_s^{min} and M_s^{max} sets the relative importance of dose range satisfaction between anatomical structures. The penalty weights M_s^{min} and M_s^{max} listed in Table reftab:HDRClinicalCriteriaParameters are typical values used at the UCSF Comprehensive Cancer Center for prostate cancer cases [76]. The penalty w_{si} at a dose calculation point i of type s can be described in mathematical form using a cost function.

$$w_{si} = \begin{cases} -M_s^{min}(D_{si} - D_s^{min}) & \text{if } D_{si} \le D_s^{min} \\ M_s^{max}(D_{si} - D_s^{max}) & \text{if } D_{si} \ge D_s^{max} \\ 0 & \text{if } D_s^{min} < D_{si} < D_s^{max} \end{cases}$$
(6.1)

Figure 6.2 plots the cost functions (penalty as a function of dose) for the prostate cancer clinical criteria in Table 6.1.

6.2.4 Linear Programming Formulation

The objective is to satisfy the clinical criteria as best as possible by computing dwell times that minimize the net dose penalty costs. Equation (6.1) from section 6.2.3 defines

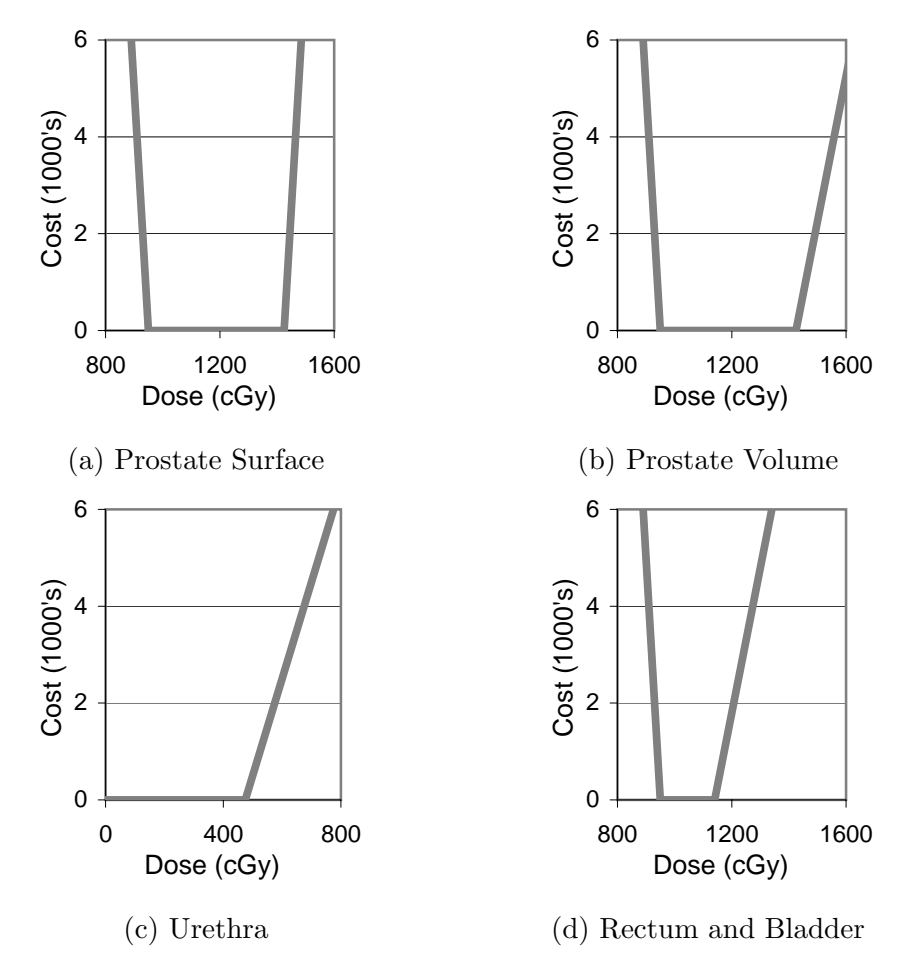


Figure 6.2. The clinical criteria, plotted here for a typical prostate cancer case, are specified using cost functions which define penalty as a function of dose for each dose calculation point type.

the cost function for an individual dose calculation point i of type s based on the clinical criteria for that point. For each type s, we define the penalty cost E_s as the average penalty cost per point:

$$E_s = \sum_{i=1}^{m_s} \frac{w_{si}}{m_s}$$
 (6.2)

where m_s is the number of dose calculation points of type s. The objective function E is effectively a weighted sum of the average cost for each tissue type s, where the relative weights are determined by the costs M_s^{min} and M_s^{max} . The global objective function is to minimize the sum of the penalty costs for the q dose calculation point types:

$$E = \sum_{s=1}^{q} E_s = \sum_{s=1}^{q} \sum_{i=1}^{m_s} \frac{w_{si}}{m_s}.$$
 (6.3)

This objective function is identical to the objective function used by IPSA [108].

The objective function E is not linear because it is composed of nonlinear functions w_{si} . However, each function w_{si} is piece-wise linear. We can formulate this problem as a linear program by creating artificial variables c_{si} to represent cost and defining the following constraints:

$$c_{si} \ge -M_s^{min}(D_{si} - D_s^{min})$$

$$c_{si} \ge M_s^{max}(D_{si} - D_s^{max})$$

$$c_{si} \ge 0.$$

$$(6.4)$$

Because w_{si} is a piece-wise linear and convex function, the constraints above guarantee that $c_{si} \geq w_{si}$ for all i, s. Furthermore, we redefine the global objective function to

$$E = \sum_{s=1}^{q} \sum_{i=1}^{m_s} \frac{c_{si}}{m_s}.$$
 (6.5)

For minimized E where the costs c_{si} satisfy the inequalities (6.4), we are guaranteed $c_{si} = w_{si}$ for all s, i. We show this by proving the contrapositive ($c_{si} \neq w_{si}$ implies E not minimized), which is logically equivalent [151]. If $c_{si} \neq w_{si}$, then $c_{si} > w_{si}$ for some s, i and there will exist a cost c'_{si} such that $c_{si} > c'_{si} \geq w_{si}$. Since c'_{si} will not violate any constraint in inequalities (6.4), it is feasible. We define E' exactly as E except using c'_{si} instead of c_{si} . Hence, E' < E and no cost variables used to compute E' violate a constraint, which implies E is not minimized. Hence, for minimized E, we are guaranteed $c_{si} = w_{si}$.

Constants:

 m_s Number of dose calculation points of type s.

Number of dwell positions.

 d_{sij} Dose-rate contribution from dwell position j to dose calculation point i of type s.

Variables:

 t_i Source dwell time for dwell position j.

 c_{si} Penalty cost at dose calculation point i of type s.

Objective:

E Global cost function.

Table 6.2. HDR dose optimization LP formulation constants, variables, and functions.

We summarize constants, variables, and the objective function for the LP formulation in Table 6.2. In equation (6.6), we explicitly define the linear program in canonical form [118] by plugging into the constraints the dose distribution D_{si} at point i of type s due to dwell

times t_i .

Minimize
$$E = \sum_{s=1}^{q} \sum_{i=1}^{m_s} \frac{c_i}{m_s}$$

Subject to:

$$c_{si} + \sum_{j=1}^{n} M_s^{min} d_{sij} t_j \ge M_s^{min} D_s^{min} \qquad s = 1, \dots, q; i = 1, \dots, m_s$$

$$c_{si} - \sum_{j=1}^{n} M_s^{max} d_{sij} t_j \ge -M_s^{max} D_s^{max} \qquad s = 1, \dots, q; i = 1, \dots, m_s$$

$$c_{si} \ge 0 \qquad \qquad s = 1, \dots, q; i = 1, \dots, m_s$$

$$t_j \ge 0 \qquad \qquad j = 1, \dots, n$$

$$(6.6)$$

A (non-optimal) feasible solution for the LP formulation can be trivially found by setting $t_j = 0$ for all j and setting

$$c_{si} = \max \left\{ -M_s^{min} \left(\left(\sum_{j=1}^n d_{sij} t_j \right) - D_s^{min} \right), 0, M_s^{max} \left(\left(\sum_{j=1}^n d_{sij} t_j \right) - D_s^{max} \right) \right\}$$

for all i and s.

Because of the properties of the artificial variables c_{si} shown above for minimized E, the optimal solution obtained for the linear program in equation (6.6) will be the same as the optimal solution to the nonlinear formulation based on the objective function in equation (6.3) with the cost functions in equation (6.1). We effectively transformed the nonlinear IPSA optimization problem in equation (6.3) (for which deterministic optimization algorithms such as local search could be trapped in sub-optimal solutions [108]) to a higher dimensional space with artificial variables in which an equivalent linear formulation (6.6) can be minimized deterministically to find the global optimal solution using the Simplex algorithm.

6.3 Application to Prostate Cancer Treatment

We implemented software using C++ to read patient specific parameters from IPSA and output the linear program (6.6) in the file format of AMPL (A Mathematical Programming Language) [62]. We solved the linear program specified in each AMPL file using ILOG

CPLEX 9.0, an advanced implementation of the Simplex algorithm [118] designed for large industrial optimization problems [79]. Computation was performed on a 3.0 GHz Pentium IV computer running the Linux operating system.

6.3.1 Patient Data Sets

We applied the LP method retrospectively to 20 prostate cancer patient cases. The prostate volumes ranged from 23 cc to 103 cc. For these patients, the physician implanted 14 to 18 catheters in the prostate with transrectal ultrasound (TRUS) guidance while the patient was under epidural anesthesia. Then Flexi-guide catheters (Best Industries, Inc., Flexi-needles, 283-25 (FL153-15NG)), which are 1.98 mm diameter hollow plastic needles through which the radioactive source will move, were inserted transperineally by following the tip of the catheter from the apex of the prostate to the base of the prostate using ultrasound and a stepper. A Foley catheter was inserted to help visualize the urethra.

After catheter implantation, a treatment planning pelvic CT scan was obtained for each patient. Three-millimeter-thick CT slices were collected using a spiral CT. The clinical target volume (CTV) and critical organs (CO) including bladder, rectum, and urethra were contoured using the Nucletron Plato Version 14.2.6 (Nucletron B.V., Veenendaal, The Netherlands). The CTV included only the prostate and no margin was added. When segmenting the bladder and rectum, the outer most mucosa surface was contoured. The urethra was defined by the outer surface of the Foley catheter. Only the urethral volume within the CTV was contoured. The CO's were contoured on all CT slices containing the CTV and at least two additional slices above and below. Implanted catheters were also segmented. A slice of a 3-D CT scan with contoured anatomical structures (prostate, urethra, rectum, and bladder) and catheters is shown in figure 6.1.

For the 20 cases, the number of dose calculation points m ranged from 1781 to 3510. Since the selection of the active dwell positions and dose calculation points affects the outcome of optimization [99], we use those generated by IPSA as input for the LP method. For the prostate cases, the images contained q = 8 dose calculation point types: "surface" and "volume" for the four contoured tissue types (prostate, urethra, bladder, and rectum). The clinical criteria used in this study are shown in 6.1.

All patients were treated at UCSF Comprehensive Cancer Center using dosimetric plans generated by the current version of IPSA. We used imaging and dosimetry records from those treatments to compare SA with LP.

6.3.2 Evaluation Metrics

We recorded the dwell times and the objective function value E for the solutions obtained using SA and LP. We evaluated the resulting dose distributions using standard dosimetric indices, including prostate V100 and V150 (the percentage of the prostate receiving over 100% and over 150% of the prescribed dose, respectively). As dose inside the prostate should fall between 100% (D^{min}) and 150% (D^{max}) of prescribed dose, ideally V100 should be 100% and V150 should be 0%. Similarly, we also evaluated V100 and V150 for the urethra. Dosimetric indices for normal structures (non-cancerous tissues) include the rectum (V50 and V100) and the bladder (V50 and V100). As normal structures should be spared radioactive dose, these indices ideally should be close to 0%. We also computed dosimetric indices in absolute dose, including the prostate D90 (the maximal dose that covers 90% of prostate volume), urethra D10 (the maximal dose that covers 10% of urethra volume), and rectum and bladder D2cc (the maximal dose that covers 2 cc of the organ volume).

6.3.3 Results

ILOG CPLEX solved for the optimal solution to the linear programming formulation in an average time of 9.00 seconds per case with a standard deviation of 3.77 seconds for the 20 prostate cancer patient cases. The times ranged from 3.68 seconds to 14.63 seconds. The Simplex algorithm in ILOG CPLEX required an average of 1653 iterations with a standard deviation of 341 iterations.

The average objective function value for the 20 prostate cancer patient cases was 3.27 for the LP method compared to 3.33 for SA. The percent difference in objective function

value between the solution found using SA and the optimal solution found using LP for each individual patient case is shown in figure 6.3. Improvement varies from a minimum of 0.84% to a maximum of 4.59%. We performed paired t-tests to determine the statistical significance (P < 0.01) of the results and found that the improvement in objective function value using the LP method compared to SA was statistically significant ($P = 1.54 \times 10^{-7}$).

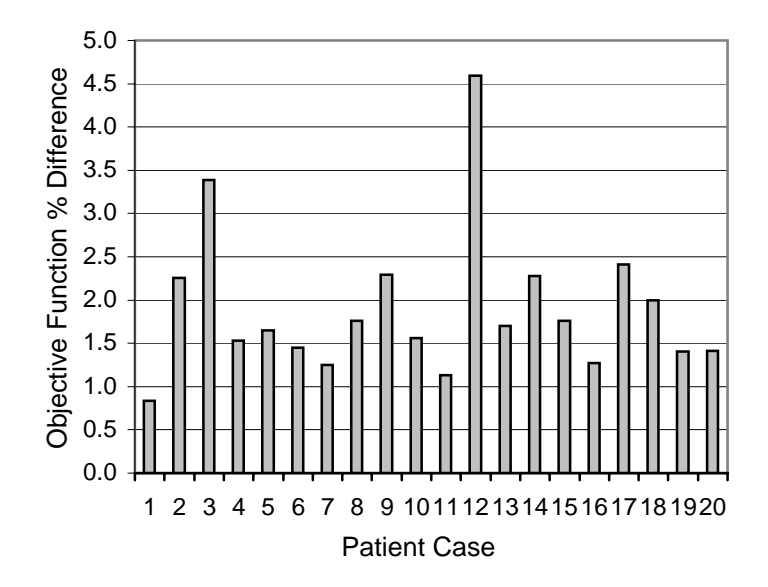


Figure 6.3. The percent difference in objective function value between the optimal solution (found using the LP method) and the solution found by SA for 20 prostate cancer patient cases. The difference is statistically significant $(P = 1.54 \times 10^{-7})$.

Figure 6.4 displays the standard dosimetric indices for both the SA and LP solutions. The bars indicate the mean indices as percents and the error bars indicate the maximum and minimum indices obtained for the 20 prostate cancer patient cases. Based on these dosimetric indices, the difference between the dose distributions generated by SA and LP was small. None of the dosimetric indices indicated a statistically significant (P < 0.01) difference between the dose distributions generated by SA and LP. The largest improvement for the prostate D90, the rectum D2cc, and the bladder D2cc were lower than 1%. The largest improvement for the urethra D10 was 2%. The urethra V150 was zero for both LP and SA method for this case. Additional dosimetric indices are shown in Table 6.3 where positive values indicate improvement and negative values indicate deterioration. The deterioration of one dosimetric index is sometimes traded for the improvement of other

dosimetric indices and the improvement of the global solution. The maximum improvement of LP over SA was a reduction of 1.65% for the prostate V150 index. However, for the same patient, LP resulted in a reduction of 0.38% of the prostate V100. Similarly, the maximum deterioration of LP over SA was an increase of 1.63% for the prostate V150 index inducing an improvement of 0.84% of the prostate V100. Even with these two extreme cases, the LP and SA methods provide two different solutions that are difficult to distinguish clinically. Figure 6.5 plots the dose-volume-histogram (DVH) for each tissue type for the patient case with the greatest magnitude improvement in a dosimetric index between the SA and LP solutions. Figure 6.6 displays a CT scan of the same patient with overlaid isodose contours for both solutions.

Dosimetric	Maximum	Minimum	Mean	99%	Significance
Index	Improvement	Improvement	Improvement	CI	P
Prostate V100	0.95	-0.49	0.13	(-0.10, 0.37)	0.1644
Prostate V150	1.65	-1.63	0.51	(-0.02, 1.04)	0.0217
Urethra V100	1.52	-1.50	0.12	(-0.33, 0.57)	0.4858
Urethra V150	0.11	-0.05	0.00	(-0.01, 0.02)	0.7621
Rectum V50	0.50	-0.81	-0.17	(-0.36, 0.02)	0.0344
Rectum V100	0.03	0.00	0.01	(-0.00, 0.01)	0.0289
Bladder V50	0.75	-0.48	0.03	(-0.17, 0.23)	0.7042
Bladder V100	0.13	-0.02	0.02	(-0.00, 0.04)	0.0225

Table 6.3. Improvement of LP solutions over SA solutions for 20 prostate cancer patient cases calculated as the absolute difference in dosimetric index percent values. Negative values indicate deterioration in the dosimetric index. The significance P of the differences was computed using paired t-tests.

6.4 Discussion

The dosimetric index results are not significantly different from those of the current version of IPSA, which was previously shown to be superior to the commonly used method of geometric optimization followed by manual adjustment [76, 98]. The small variances observed for the prostate and urethra in figure 6.4 show the consistency of the treatment plan quality for both the SA and LP methods. The larger variances for the prostate V150, the rectum, and the bladder are due to differences between patients in anatomy, prostate volume, and distances between the prostate and organs at risk.

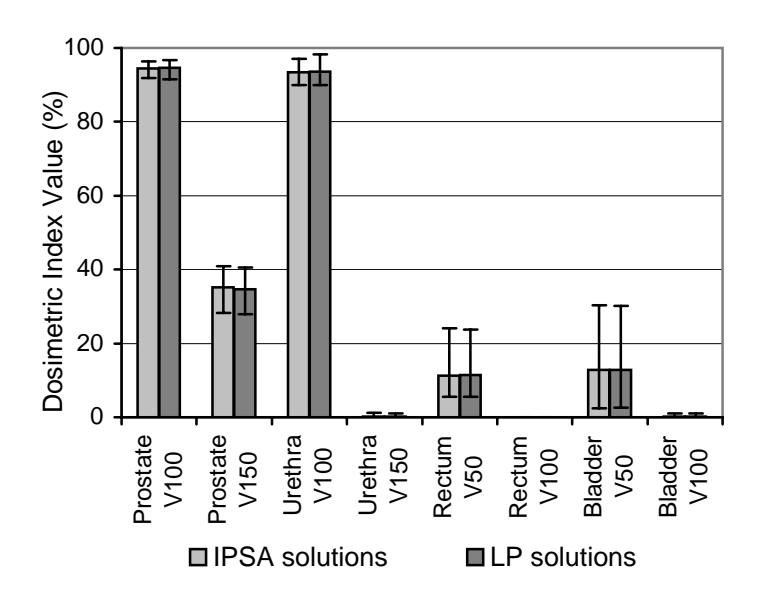


Figure 6.4. Mean dosimetric index results for the SA and LP methods for 20 prostate cancer patient cases. Error bars indicate maximum and minimum values for the 20 patient cases.

The LP and SA methods are both based on IPSA's objective function for the HDR brachytherapy dwell time optimization problem. The only difference is the optimization algorithm used, simulated annealing versus an equivalent linear programming formulation that can be solved using the Simplex algorithm. As simulated annealing is a probabilistic method, it is only guaranteed to converge to an optimal solution after an infinite amount of computation time. Standard termination criteria, such as stopping the algorithm after a fixed number of iterations, can result in sub-optimal solutions. During the development phase of the current version of IPSA, a large number of cases were run using a very large number of iterations (>1 million) and no significant improvements in the dosimetric indices were found compared to the values found after 100,000 iterations. However, the closeness to mathematical optimality of the solutions of the current version of IPSA could not be guarantied for every new clinical case.

Because the LP formulation of IPSA's objective function can be solved deterministically to find the solution that globally minimizes costs, the LP method solution provides a precise baseline for evaluating solutions obtained by probabilistic methods such as SA. The LP method computed a solution with a better objective function value compared to SA for every patient case. The improvement in objective function values of LP compared to SA was

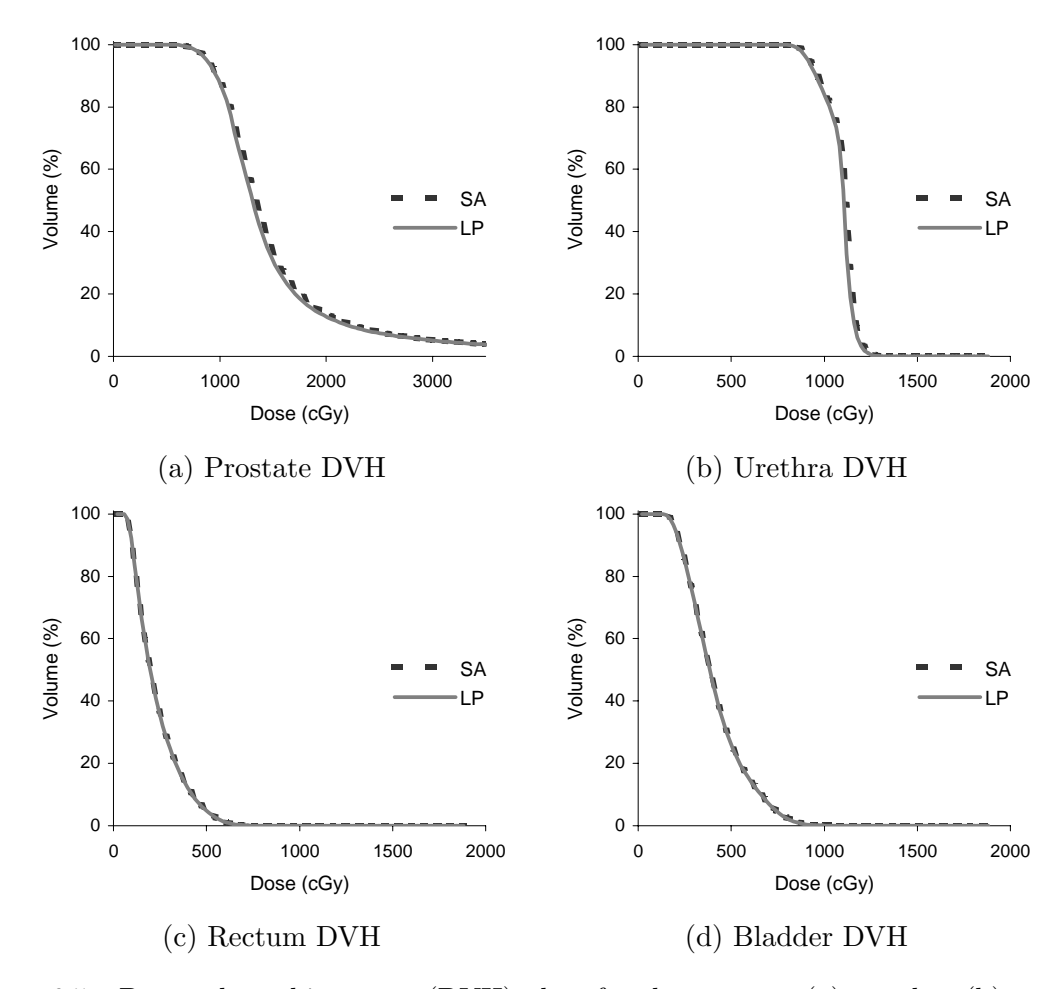


Figure 6.5. Dose-volume-histogram (DVH) plots for the prostate (a), urethra (b), rectum (c), and bladder (d) for the patient case with greatest difference in dosimetric indices between the LP and SA solutions. For dose less than D^{min} for each tissue type, the desired volume is 100%. For dose greater than D^{max} , the desired volume 0%.

statistically significant. However, the effect size of the objective function improvement was not sufficient to result in statistically significant differences in standard dosimetric indices for our sample of 20 prostates with volume ranging from 23 cc to 103 cc. We observe that the DVH plots for the patient case with the largest difference in dosimetric indices are similar for both methods (figure 6.5) while differences are observable on the isodose curves (figure 6.6). The hot spots (prostate V150) have different shapes and the prostate V120 curve is at a different location. This indicates that the local dose distribution (isodose) is different while global dose delivered to the organs (DVH) and critical dose delivered to the organs (dosimetric indices) are equivalent. This quantitatively indicates that the dose distributions generated by SA are clinically equivalent to the best achievable dose distributions based on

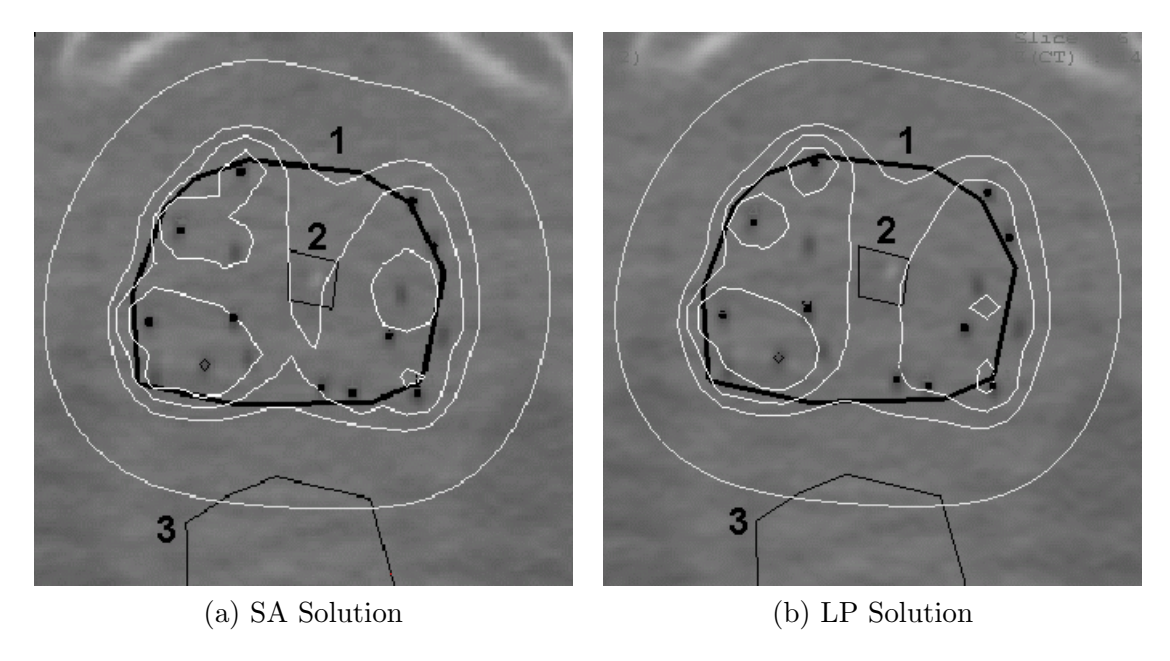


Figure 6.6. Isodose curves for the SA (a) and LP (b) solutions for the patient case with greatest difference in dosimetric indices. The prostate (1), urethra (2), and rectum (3) are contoured in black. Catheters are shown as black dots. Isodose curves for 50%, 100% (D^{min}), 120%, and 150% (D^{max}) of prostate minimum prescribed dose are plotted in white.

the current IPSA objective function with dose constraints and penalty weights selected for prostate cancer cases.

6.5 Conclusion and Future Work

Prostate cancer is increasingly treated with high-dose-rate (HDR) brachytherapy, a type of radiotherapy in which a radioactive source is guided through catheters temporarily implanted in the prostate. Clinicians must set dwell times for the source inside the catheters so the resulting dose distribution minimizes deviation from dose prescriptions that conform to patient-specific anatomy. The primary contribution of this chapter is to take the well-established dwell times optimization problem defined by Inverse Planning by Simulated Annealing (IPSA) developed at UCSF and exactly formulate it as a linear programming (LP) problem. Because LP problems can be solved exactly and deterministically, this formulation provides strong performance guarantees: one can rapidly find the dwell times solution that globally minimizes IPSA's objective function for any patient case and clinical

criteria parameters. For a sample of 20 prostate cancer patient cases, the new LP method optimized dwell times in less than 15 seconds per case on a standard PC.

We quantitatively compared the dwell times solutions currently being obtained clinically using simulated annealing (SA), a probabilistic method, to the mathematically optimal solutions obtained using the LP method. The LP method resulted in significantly improved objective function values compared to SA, but none of the dosimetric indices indicated a statistically significant difference. The results indicate that solutions generated by the current version of IPSA are clinically equivalent to the mathematically optimal solutions.

IPSA's objective function with dose constraints and penalty weights covers all organs and all clinical objectives so they can be optimized simultaneously. The physician can adjust the objectives for each optimization. However, if a particular set of objectives generates the desired results then the same set of objectives can be used for optimization of clinically similar cases (i.e. prostate) without further adjustments. This set of objectives, commonly called a class solution, can be used as a starting point for every patient, significantly reducing the time needed to plan individual patient treatments.

Although we focused on the application of our linear programming formulation to prostate cancer patient cases, the mathematical formulation can also be applied to other cancer types for which HDR brachytherapy is used by incorporating different clinical parameters. The method can also be extended to support any piece-wise linear convex cost functions, not solely the 3-piece cost functions presented above. Recent developments in magnetic resonance spectroscopy imaging and image registration introduce a new clinical criterion, a dose boost to the tumor volume within the prostate [89, 6, 9]. Although we do not explicitly consider that dose calculation point type, the mathematical formulation we defined can be extended to incorporate it by adding a tumor volume tissue type. A potential advantage of the LP method for each of these extensions is that it will use the well-established framework of IPSA and deterministically compute mathematically optimal dwell time solutions for all patient cases.

Although we used linear programming purely as an optimization method in this chapter,

linear programming brings with it a vast literature of tools and extensions. This includes well-established tools like sensitivity analysis [118], as well as newer extensions like robust optimization that considers uncertainty in input parameters [24]. In future work, we plan to explore these tools and extensions to provide clinicians with patient-specific information about the trade-offs between feasible treatment plans.

Chapter 7

Conclusion

The main contributions of this dissertation are new algorithms that computationally plan and optimize image-guided medical procedures based on physician-specified clinical criteria. Computational methods to address these problems are now possible because of advances in computation power and exciting recent developments in medical imaging, which are enabling clinicians to noninvasively examine anatomy and metabolic processes deep below the skin's surface. We focus on four planning and optimization problems: target localization in deformable tissues, motion planning for rigid needles in deformable tissue, motion planning for steerable needles, and dose optimization for brachytherapy cancer treatment.

Each of the planning and optimization problems covered in this dissertation introduce new computational challenges and are subject to unique planning and optimization constraints imposed by the physician's treatment requirements, the patient's anatomy, and the physical limitations of medical equipment and devices. We present planning and optimization algorithms for each of these general problems, and then customize the solution to the specific application of prostate brachytherapy.

7.1 Contributions

An essential component of several of our planning and optimization algorithms is a simulation of tissue deformations that occur when surgical instruments such as needles contact soft tissue. We identified and implemented appropriate models and algorithms to interactively estimate soft tissue deformations due to forces applied during surgical and interventional medical procedures. The software tools integrate methods from real-time physically-based modeling in computer graphics and classical finite element modeling. We then developed a 2-D simulation of medical needle insertion that estimates tissue deformations using a finite element model and real-time mesh maintenance.

7.1.1 Target Localization using Deformable Image Registration

We designed a deformable image registration method that explicitly considers tissue deformations when mapping targets between images captured at different times by possibly different imaging modalities. Our method creates a biomechanical model of the soft tissue and uses nonlinear optimization to estimate uncertain model parameters. We implemented a 2-D version of this algorithm. In collaboration with researchers in the Magnetic Resonance Science Center and the Department of Radiation Oncology at UCSF, we applied it to prostate MR Spectroscopic Imaging (MRSI), a recently developed imaging modality that is enabling physicians to non-invasively pinpoint the location of cancerous cells inside the body by measuring concentrations of metabolic compounds correlated with cancer. Results using our method with these prostate medical images indicate a statistically significant improvement in target registration accuracy compared with previous methods.

7.1.2 Motion Planning for Rigid Needles in Deformable Tissue

Accurately guiding a needle to a specific target inside the human body is crucial for the success of many medical procedures, from biopsies to anesthesia injections to cancer treatments such as cryotherapy and brachytherapy. However, significant errors are common in current practice due to soft tissue deformation caused by forces exerted on the tissue by

the needle during insertion. We designed and implemented a motion planning algorithm for traditional stiff medical needle insertion procedures to correct for errors caused by predicted soft tissue deformations. The method combines a finite element model of needle insertion in soft tissue with numeric optimization. In collaboration with researchers in Radiation Oncology at UCSF, we applied the planner to an example from prostate brachytherapy and demonstrated in simulation that pre-procedure planning can substantially reduce radioactive seed placement error.

7.1.3 Motion Planning for Steerable Needles

We designed and implemented a motion planning algorithm that explicitly considers uncertainty in motion for nonholonomic mobile robots subject to a constant turning radius. We applied this planning approach to a new class of *steerable* medical needles that we are developing with researchers from The Johns Hopkins University. The needles have two features enabling steering: a bevel-tip that exerts asymmetric forces on the surrounding soft tissue, and high flexibility causing the needles to bend in the direction of their bevel. These needles can be steered to targets in soft tissue previously inaccessible to stiff needles. The motion planning algorithm combines geometric planning with Markov Decision Processes and Dynamic Programming. Results indicate that traditional shortest paths do not maximize the probability of successfully acquiring the target when the motion of the needle cannot be predicted with certainty.

7.1.4 Dose Optimization for Brachytherapy Cancer Treatment

We formulated the HDR brachytherapy dose optimization problem as a linear program, enabling the fast computation of mathematically optimal solutions. Dose prescriptions are specified by the physician using medical images of patient anatomy and estimates of tumor location. The linear program uses the objective and clinical criteria framework of the IPSA software developed at UCSF and maximizes satisfaction of the physician specified dose prescriptions. In collaboration with researchers in Radiation Oncology at UCSF, we

used the guaranteed mathematical optimality of our linear program solutions to statistically validate the performance of the current IPSA software, which is based on the probabilistic method of simulated annealing, a method that has been used in the treatment of over a thousand cancer patients internationally.

7.2 Future Work

In this thesis, we focused on planning and optimization problems for image-guided medical procedures that consider tissue on a 2-D imaging plane. Due to constraints of many imaging modalities such as ultrasound imaging, often only 2-D anatomical and tissue deformation information is available. However, the improving performance and increasing availability of full 3-D imaging modalities such as CT scans and MRI is introducing the ability to acquire 3-D patient-specific information pre- and intra-operatively. We plan to extend our 2-D methods to consider full 3-D tissue volumes. We also plan to develop new planning algorithms that explicitly consider uncertainty in tool/tissue interaction.

7.2.1 Realistic Simulation of Image-Guided Medical Procedures

In chapter 2, we focused on tissue deformations that occur in a 2-D imaging plane during needle insertion procedures. We will build on our experience with 2-D simulation of traditional needles inserted into soft tissues to develop an accurate and efficient 3-D FEM simulation of tissue deformations.

The first challenge is to define meshes of appropriate complexity to represent heterogeneous tissue. Our input will be a 3-D image volume and the segmented boundaries of the tissues of interest specified using polygonal outlines on multiple slices of the 3-D volume. From these outlines, we can generate surface meshes for each tissue type using methods such as Marching Cubes [110]. We then hope to use and extend open source software tools such as NETGEN and TetGen [140, 146] to automatically generate a 3-D tetrahedral mesh from the tissue type surface meshes.

The next challenge is representing forces exerted by the needle on the soft tissue. In 2-D, we modified the mesh as the needle was being inserted, maintaining mesh nodes along the needle shaft so that we could apply cutting and frictional forces as FEM boundary conditions. In 3-D, we plan to consider three approaches: mesh modification, mesh refinement, and meshless methods. Although mesh modification worked well in our 2-D simulation in chapter 2, we need to investigate whether modification of the 3-D mesh can be performed without resulting in degenerate elements (elements that invert and have "negative" area). With mesh refinement, we will create new nodes in the vicinity of the needle path, which has been successfully applied to needle insertion in 2-D [121], but will require significant improvements in algorithmic computational complexity to be appropriate for real-time interactive 3-D simulation. We also plan to explore meshless methods, a relatively new approach based on clouds of linked nodes [109].

For many types of soft tissue, the relationship between stress and strain is highly nonlinear [63]. Fast and accurate simulation of 3-D deformable soft tissues with nonlinear
behavior has not yet been integrated into a practical surgery simulator. We plan to explore
computationally efficient ways to simulate realistic tissue mechanics and dynamics due to
forces applied by surgical instruments or devices such as needles. In chapter 2, we focused
on linearly elastic models of soft tissue. In future work, we hope to incorporate nonlinear tissue behavior, including both nonlinear geometry and nonlinear soft tissue material
properties, to accurately simulate large deformations. To more realistically model tissue dynamics, we also hope to explicitly model slip between tissue types. Rather than considering
the mesh of heterogeneous tissue to be connected, we will allow each independently meshed
tissue type to deform and move independently and affect neighboring tissues through collision and frictional forces. For computational efficiency, we will consider oct-trees and
related data structures to accelerate collision detection of deformable objects [73]. Because
patient-specific tissue parameters generally cannot be known exactly, we hope to develop
probabilistic models to compute and display uncertainty in tissue deformations.

Finally, it is crucial to validate these new simulation and planning algorithms using data from physical experiments. We plan to validate simulations using both controlled tissue phantom experiments like those conducted using the JHU needle insertion testbed [158] as well as medical images and videos from actual patient cases.

7.2.2 Planning Algorithms for Image-Guided Medical Procedures

New treatment technologies also introduce new computational planning challenges. In this dissertation, we discussed motion planning for steerable needles, a new treatment approach that we recently submitted for a United States patent [160]. New extensions to needle steering are already being proposed which change the dynamic behavior of the needle, including a flattened and expanded bevel tip [57]. In future work, we plan to explore motion planning for steerable needles in 3-D, where the needle can follow complicated corkscrew trajectories. Using extensions to the needle simulation presented in chapter 2, we also plan to explicitly consider the effects of tissue deformations.

There is also a renaissance in new research on thermal therapy for cancer treatment, a procedure in which directional beams of heat are used to kill cancer cells. This type of therapy raises dose planning problems mathematically similar to HDR brachytherapy dose optimization but with the new capability of directional beams [49]. This treatment approach introduces new challenges for planning since the plan must be updated in real-time during treatment to override the natural tendency of living tissues to compensate for temperature changes.

We also plan to explore the more general topic of motion planning with explicit consideration of motion uncertainty. The standard formulation of the motion planning problem considers a static workspace or deterministically moving obstacles [105]. However, we showed in chapter 5 that, due to motion uncertainty, traditional shortest path metrics are not generally optimal in medical applications. Developing new classes of motion planners that explicitly consider motion uncertainty and its effect on the planning objective will improve the effectiveness of surgical planners operating inside the highly variable environment of living tissue.

7.3 Conclusion

In medicine, improvements in imaging, combined with improved accuracy in reaching what is revealed, can lead to improved treatment and patient health. Innovations in medical imaging are continuously improving existing modalities and introducing new modalities. Mega-voltage Cone-beam Computed Tomography (MV CBCT) is a new imaging modality that uses the same linac as Intensity Modulated Radiation Therapy (IMRT), allowing physicians to image and treat the patient using the same device without moving and realigning the patient [128, 116]. Optical coherence tomography (OCT) is an optical in vivo imaging method with micron-scale resolution which can be used to visualize the tiny intraretinal and intracorneal anatomy [55]. Molecular imaging techniques are enabling radiologists to visualize in vivo intra-cellular biochemical pathways, introducing the potential to identify pathways involved in disease before traditional symptoms appear [161]. Each new imaging modality introduces a wealth of new digital information, which introduces new computational challenges. By combining medical imaging with planning and optimization algorithms, we hope to assist physicians and, ultimately, improve patient care.

Bibliography

- [1] E. Aarts and J. Korst. Simulated annealing and Boltzmann Machines (Interscience Series in Discrete Mathematics and Optimization). John Wiley & Sons, Inc., 1st edition, 1989.
- [2] P. K. Agarwal, T. Biedl, S. Lazard, S. Robbins, S. Suri, and S. Whitesides. Curvature-constrained shortest paths in a convex polygon. SIAM J. Comput., 31(6):1814–1851, 2002.
- [3] S. Akella, W. Huang, K. M. Lynch, and M. T. Mason. Sensorless parts feeding with a one joint robot. In *Workshop on the Algorithmic Foundations of Robotics*, July 1996.
- [4] O. Alagoz, L. M. Maillart, A. J. Schaefer, and M. Roberts. The optimal timing of living-donor liver transplantation. *Management Science*, 50(10):1420–1430, 2005.
- [5] R. Alterovitz, M. Branicky, and K. Goldberg. Constant-curvature motion planning under uncertainty with applications in image-guided medical needle steering. In *Workshop on the Algorithmic Foundations of Robotics*, July 2006.
- [6] R. Alterovitz, K. Goldberg, J. Kurhanewicz, J. Pouliot, and I.-C. Hsu. Image registration for prostate MR Spectroscopy using biomechanical modeling and optimization of force and stiffness parameters. In Proc. Int. Conf. of the IEEE Engineering In Medicine and Biology Society, Sept. 2004.
- [7] R. Alterovitz, K. Goldberg, J. Kurhanewicz, J. Pouliot, and I.-C. Hsu. Registering MR with MRS images for HDR prostate treatment using finite element modeling. In *American Association of Physicists in Medicine (AAPM) 46th Annual Meeting*, July 2004.
- [8] R. Alterovitz, K. Goldberg, and A. Okamura. Planning for steerable bevel-tip needle insertion through 2D soft tissue with obstacles. In *Proc. IEEE Int. Conf. on Robotics and Automation*, pages 1652–1657, Apr. 2005.
- [9] R. Alterovitz, K. Goldberg, J. Pouliot, I.-C. J. Hsu, Y. Kim, S. M. Noworolski, and J. Kurhanewicz. Registration of MR prostate images with biomechanical modeling and nonlinear parameter estimation. *Medical Physics*, 33(2):446–454, Feb. 2006.
- [10] R. Alterovitz, Y. Kim, J. Kurhanewicz, J. Pouliot, I.-C. J. Hsu, and K. Goldberg. Prostate MR spectroscopy image registration using biomechanical modeling of tissue deformations due to endorectal probe insertion. In *Annual Meeting of the American Brachytherapy Society*, June 2005.

- [11] R. Alterovitz, E. Lessard, J. Pouliot, I.-C. J. Hsu, J. F. O'Brien, and K. Goldberg. High-dose-rate brachytherapy dose optimization for prostate cancer using linear programming. In *Annual Meeting of the Institute for Operations Research and the Management Sciences (INFORMS)*, Nov. 2005.
- [12] R. Alterovitz, E. Lessard, J. Pouliot, I.-C. J. Hsu, J. F. O'Brien, and K. Goldberg. Optimization of HDR brachytherapy dose distributions using linear programming with penalty costs. *to appear in Medical Physics*, 2006.
- [13] R. Alterovitz, A. Lim, K. Goldberg, G. S. Chirikjian, and A. M. Okamura. Steering flexible needles under Markov motion uncertainty. In *Proc. IEEE/RSJ Int. Conf. on Intelligent Robots and Systems*, pages 120–125, Aug. 2005.
- [14] R. Alterovitz, J. Pouliot, R. Taschereau, I.-C. Hsu, and K. Goldberg. Modeling seed misplacement by simulating tissue deformations. In *Annual Meeting of the American Brachytherapy Society*, May 2003.
- [15] R. Alterovitz, J. Pouliot, R. Taschereau, I.-C. Hsu, and K. Goldberg. Needle insertion and radioactive seed implantation in human tissues: Simulation and sensitivity analysis. In *Proc. IEEE Int. Conf. on Robotics and Automation*, volume 2, pages 1793–1799, Sept. 2003.
- [16] R. Alterovitz, J. Pouliot, R. Taschereau, I.-C. Hsu, and K. Goldberg. Sensorless planning for medical needle insertion procedures. In *Proc. IEEE/RSJ Int. Conf. on Intelligent Robots and Systems*, volume 3, pages 3337–3343, Oct. 2003.
- [17] R. Alterovitz, J. Pouliot, R. Taschereau, I.-C. Hsu, and K. Goldberg. Simulating needle insertion and radioactive seed implantation for prostate brachytherapy. In J. D. Westwood et al., editors, *Medicine Meets Virtual Reality 11*, pages 19–25. IOS Press, Jan. 2003.
- [18] M. A. Audette, H. Delingette, A. Fuchs, O. R. Astley, and K. Chinzei. A topologically faithful, tissue-guided, spatially varying meshing strategy for computing patient-specific head models for endoscopic pituitary surgery simulation. In J. D. Westwood et al., editors, *Medicine Meets Virtual Reality* 14, pages 22–27. IOS Press, Jan. 2005.
- [19] F. S. Azar, D. N. Metaxas, and M. D. Schnall. A deformable finite element model of the breast for predicting mechanical deformations under external perturbations. *Academic Radiology*, 8(10), 2001.
- [20] R. Bajcsy and C. Broit. Matching of deformed images. In 6th Int. Conf. on Pattern Recognition, pages 351–353, 1982.
- [21] D. Baraff and A. Witkin. Large steps in cloth animation. In *Proc. SIGGRAPH 98*, pages 43–54, July 1998.
- [22] J. L. Barker, A. Garden, K. K. Ang, J. C. O'Daniel, H. Wang, L. E. Court, W. H. Morrison, D. Rosenthal, K. Chao, S. Tucker, R. Mohan, and L. Dong. Quantification of volumetric and geometric changes occurring during fractionated radiotherapy for head-and-neck cancer using an integrated CT/linear accelerator system. *Int. J. of Radiation Oncology, Biology, Physics*, 59(4):960–970, 2004.

- [23] M. S. Bazaraa, H. D. Sherali, and C. M. Shetty. Nonlinear Programming: Theory and Algorithms. John Wiley & Sons, Inc., 2 edition, 1993.
- [24] A. Ben-Tal and A. Nemirovski. Robust solutions of uncertain linear programs. *Operations Research Letters*, 25:1–13, 1999.
- [25] D. P. Bertsekas. Dynamic Programming and Optimal Control. Athena Scientific, Belmont, MA, 2nd edition, 2000.
- [26] A. Bharatha, M. Hirose, N. Hata, S. K. Warfield, M. Ferrant, K. H. Zou, E. Suarez-Santana, J. Ruiz-Alzola, A. D'Amico, R. A. Cormack, R. Kikinis, F. A. Jolesz, and C. M. C. Tempanya. Evaluation of three-dimensional finite element-based deformable registration of pre- and intraoperative prostate imaging. *Medical Physics*, 28(12):2551–2560, Dec. 2001.
- [27] A. Bicchi, G. Casalino, and C. Santilli. Planning shortest bounded-curvature paths for a class of nonholonomic vehicles among obstacles. In *Proc. IEEE Int. Conf. on Robotics and Automation*, pages 1349–1354, 1995.
- [28] K.-F. Böhringer, V. Bhatt, B. R. Donald, and K. Goldberg. Algorithms for sensorless manipulation using a vibrating surface. *Algorithmica*, 26:389–429, 2000.
- [29] M. Bro-Nielsen, J. Tasto, R. Cunningham, and G. Merril. Preop endoscopic simulator: A pc-based immersive training system. In J. D. Westwood et al., editors, *Medicine Meets Virtual Reality* 7, pages 76–82. IOS Press, Jan. 1999.
- [30] R. C. Brost. Automatic grasp planning in the presence of uncertainty. *Int. J. of Robotics Research*, 7(1):3–17, Feb. 1988.
- [31] I. Brouwer, J. Ustin, L. Bentley, A. Sherman, N. Dhruv, and F. Tendick. Measuring in vivo animal soft tissue properties for haptic modeling in surgical simulation. In J. D. Westwood et al., editors, *Medicine Meets Virtual Reality*, pages 69–74. IOS Press, Jan. 2001.
- [32] J. Brown, S. Sorkin, C. Bruyns, J. Latombe, K. Montgomery, and M. Stephanides. Real-time simulation of deformable objects: tools and applications. *Computer Animation*, Nov. 2001.
- [33] J. D. Brown, J. Rosen, Y. S. Kim, L. Chang, M. N. Sinanan, and B. Hannaford. In-vivo and in-situ compressive properties of porcine abdominal soft tissues. In J. D. Westwood et al., editors, Medicine Meets Virtual Reality 11, pages 26–32. IOS Press, Jan. 2003.
- [34] D. R. Cahill, M. J. Orland, and G. M. Miller. Atlas of human cross-sectional anatomy: with CT and MR Images. Wiley-Liss, New York, NY, 3rd edition, 1995.
- [35] M. C. Cavusoglu. Telesurgery and Surgical Simulation: Design, Modeling and Evaluation of Haptic Interfaces to Real and Virtual Surgical Environments. PhD thesis, University of California, Berkeley, 2000.
- [36] K. Chinzei, N. Hata, F. A. Jolesz, and R. Kikinis. MR compatible surgical assist robot: System integration and preliminary feasibility study. In *Medical Image Computing and Computer Assisted Intervention*, pages 921–930, Oct. 2000.

- [37] H. Choset, K. M. Lynch, S. Hutchinson, G. Kantor, W. Burgard, L. E. Kavraki, and S. Thrun. *Principles of Robot Motion: Theory, Algorithms, and Implementations*. MIT Press, 2005.
- [38] G. Christensen, M. Miller, M. Vannier, and U. Grenander. Individualizing neuroanatomical atlases using a massively parallel computer. *IEEE Computer*, 29(1):32–38, 1996.
- [39] D. Citrin, H. Ning, H. Guion, G. Li, R. Susil, R. Miller, E. Lessard, J. Pouliot, X. Huchen, J. Capala, C. Coleman, K. Camphausen, and C. Menard. Inverse treatment planning based on MRI for HDR prostate brachytherapy. *Int. J. of Radiation Oncology, Biology, Physics*, 61(4):1267–1275, 2005.
- [40] F. G. Claus, H. Hricak, and R. R. Hattery. Pretreatment evaluation of prostate cancer: Role of MR imaging and ¹H MR spectroscopy. *Radio Graphics*, 24:S167–S180, 2004.
- [41] K. Cleary, L. Ibanez, N. Navab, D. Stoianovici, A. Patriciu, and G. Corral. Segmentation of surgical needles for fluoroscopy servoing using the Insight Software Toolkit (ITK). In *Proc. Int. Conf. of the IEEE Engineering In Medicine and Biology Society*, pages 698–701, 2003.
- [42] S. Cotin and H. Delingette. Real-time surgery simulation with haptic feedback using finite elements. In *Proc. IEEE Int. Conf. on Robotics and Automation*, pages 3739–3744, 1998.
- [43] S. Cotin, H. Delingette, and N. Ayache. Real-time elastic deformations of soft tissues for surgery simulation. *IEEE Trans. on Visualization and Computer Graphics*, 5(1), 1999.
- [44] J. R. Crouch. Medial Techniques for Automating Finite Element Analysis. PhD thesis, University of North Carolina, Chapel Hill, 2003.
- [45] J. R. Crouch, S. M. Pizer, E. L. Chaney, and M. Zaider. Medially based meshing with finite element analysis of prostate deformation. In *Medical Image Computing and Computer Assisted Intervention*, pages 108–115, 2003.
- [46] J. E. Dawson, T. Wu, T. Roy, J. Y. Gy, and H. Kim. Dose effects of seeds placement deviations from pre-planned positions in ultrasound guided prostate implants. *Radiotherapy and Oncology*, 32(2):268–270, 1994.
- [47] K. DeWitt, I.-C. Hsu, V. Weinberg, E. Lessard, and J. Pouliot. 3-d inverse treatment planning for the tandem and ovoid applicator in cervical cancer. *Int. J. of Radiation Oncology, Biology, Physics*, 63(4):1270–1274, 2005.
- [48] L. R. Dice. Measures of the amount of ecologic association between species. *Ecology*, 26(3):297–302, 1945.
- [49] C. J. Diederich, R. J. Stafford, W. H. Nau, E. C. Burdette, R. E. Price, and J. D. Hazle. Transurethral ultrasound applicators with directional heating patterns for prostate thermal therapy: In vivo evaluation using MR thermometry. *Medical Physics*, 31(2):405–413, 2004.

- [50] S. P. DiMaio, D. F. Kacher, R. E. Ellis, G. Fichtinger, N. Hata, G. P. Zientara, L. P. Panych, R. Kikinis, and F. A. Jolesz. Needle artifact localization in 3T MR images. In J. D. Westwood et al., editors, *Medicine Meets Virtual Reality* 14, pages 120–125. IOS Press, Jan. 2006.
- [51] S. P. DiMaio, S. Pieper, K. Chinzei, N. Hata, E. Balogh, G. Fichtinger, C. M. Tempany, and R. Kikinis. Robot-assisted needle placement in open-MRI: System architecture, integration and validation. In J. D. Westwood et al., editors, *Medicine Meets Virtual Reality* 14, pages 126–131. IOS Press, Jan. 2006.
- [52] S. P. DiMaio and S. E. Salcudean. Needle insertion modeling and simulation. In *Proc. IEEE Int. Conf. on Robotics and Automation*, pages 2098–2105, May 2002.
- [53] S. P. DiMaio and S. E. Salcudean. Needle insertion modeling and simulation. IEEE Trans. on Robotics and Automation, 19(5):864–875, Oct. 2003.
- [54] S. P. DiMaio and S. E. Salcudean. Needle steering and model-based trajectory planning. In Medical Image Computing and Computer Assisted Intervention, pages 33–40, 2003.
- [55] W. Drexler, U. Morgner, R. K. Ghanta, F. X. Kärtner, J. S. Schuman, and J. G. Fujimoto. Ultrahigh-resolution ophthalmic optical coherence tomography. *Nature Medicine*, 7:502–507, 2001.
- [56] L. Dubins. On curves of minimal length with a constraint on average curvature and with prescribed initial and terminal positions and tangents. American J. of Mathematics, 79:497–516, 1957.
- [57] J. Engh, G. Podnar, D. Kondziolka, and C. Riviere. Toward effective needle steering in brain tissue. In *Proc. Int. Conf. of the IEEE Engineering In Medicine and Biology Society*, Sept. 2006.
- [58] M. Erdmann and M. Mason. An exploration of sensorless manipulation. *IEEE J. of Robotics and Automation*, 4(4):369–379, Aug. 1986.
- [59] B. Fei, C. Kemper, and D. L. Wilson. A comparative study of warping and rigid body registration for the prostate and pelvic MR volumes. *Computerized Medical Imaging and Graphics*, 27:267–281, 2003.
- [60] B. Fei, A. Wheaton, Z. Lee, J. I. Duerk, and D. Wilson. Automatic MR volume registration and its evaluation for the pelvis and prostate. *Physics in Medicine and Biology*, 47(5):823–838, Mar. 1999.
- [61] G. Fichtinger, T. L. DeWeese, A. Patriciu, A. Tanacs, D. Mazilu, J. H. Anderson, K. Masamune, R. H. Taylor, and D. Stoianovici. System for robotically assisted prostate biopsy and therapy with intraoperative CT guidance. *Academic Radiology*, 9(1):60–74, 2002.
- [62] R. Fourer, D. M. Gay, and B. W. Kernighan. *AMPL: a modeling language for mathematical programming*. Thomson/Brooks/Cole, 2 edition, 2003.
- [63] Y. C. Fung. Biomechanics: Mechanical Properties of Living Tissues. Springer, 2nd edition, 1993.

- [64] Y. C. Fung. A First Course in Continuum Mechanics. Prentice Hall, 3rd edition, 1994.
- [65] A. Gallagher, E. Ritter, H. Champion, G. Higgins, M. Fried, G. Moses, C. Smith, and R. Satava. Virtual reality simulation for the operating room: proficiency-based training as a paradigm shift in surgical skills training. *Annals of Surgery*, 241:364–372, Feb. 2005.
- [66] S. Geman and D. Geman. Stochastic relation, gibbs distribution and bayesian restoration of images. *IEEE Trans. Patt. Anal. Mac. Int.*, 6:721–741, 1984.
- [67] General Electric Company. PROSE Pulse Sequence, chapter 6. 2002.
- [68] S. F. Gibson and B. Mirtich. A survey of deformable modeling in computer graphics. Technical report, MERL, TR-97-19, 1997.
- [69] D. Glozman and M. Shoham. Flexible needle steering and optimal trajectory planning for percutaneous therapies. In *Medical Image Computing and Computer Assisted* Intervention, Sept. 2004.
- [70] K. Y. Goldberg. Orienting polygonal parts without sensing. *Algorithmica*, 10:201–255, 1993.
- [71] E. K. Hansen, K. Bucci, J. M. Quivey, V. Weinberg, and P. Xia. Repeat CT imaging and re-planning during the course of IMRT for head and neck cancer. *Int. J. of Radiation Oncology, Biology, Physics*, 2006.
- [72] C. E. Hayes, M. J. Dietz, B. F. King, and R. L. Ehman. Pelvic imaging with phased array coils: quantitative assessment of signal-to-noise ratio improvement. *Journal of Magnetic Resonance Imaging*, 2:321–326, 1992.
- [73] D. Hearn and M. P. Baker. Computer Graphics. Prentice Hall, 2003.
- [74] R. Horn. Closed-form solution of absolute orientation using unit quaternions. *Journal* of the Optical Society of America A, 4:629–642, 1987.
- [75] H. Hricak, S. White, D. Vigneron, J. Kurhanewicz, A. Kosco, D. Levin, J. Weiss, P. Narayan, and P. Carroll. Carcinoma of the prostate gland: MR imaging with pelvic phased-array coils versus integrated endorectal-pelvic phased-array coils. *Radiology*, 193:703-709, 1994.
- [76] I.-C. J. Hsu, E. Lessard, V. Weinberg, and J. Pouliot. Comparison of inverse planning simulated annealing and geometrical optimization for prostate high-dose-rate brachytherapy. *Brachytherapy*, 3:147–152, 2004.
- [77] S. Hui and R. Das. Optimization of conformal avoidance: a comparative study of prone vs. supine interstitial high-dose-rate breast brachytherapy. *Brachytherapy*, 4(2):137–140, 2005.
- [78] J. E. Husband, A. R. Padhani, A. D. MacVicar, and P. Revell. Magnetic resonance imaging of prostate cancer: comparison of image quality using endorectal and pelvic phased array coils. *Clinical Radiology*, 53:673–681, 1998.

- [79] ILOG, Inc. . ILOG CPLEX: High-performance software for mathematical programming and optimization. Available: http://www.ilog.com/products/cplex/, 2005.
- [80] R. Jacob, A. Hanlon, E. Horwitz, B. Movsas, R. Uzzo, and A. Pollack. The relationship of increasing radiotherapy dose to reduced distant metastases and mortality in men with prostate cancer. *Cancer*, 100(3):538–543, 2004.
- [81] P. Jacobs and J. Canny. Planning smooth paths for mobile robots. In *Proc. IEEE Int. Conf. on Robotics and Automation*, pages 2–7, May 1989.
- [82] D. L. James and D. K. Pai. ARTDEFO: Accurate real time deformable objects. In *Proceedings of ACM SIGGRAPH 99*, pages 65–72, 1999.
- [83] A. Jemal, R. C. Tiwari, T. Murray, A. Ghafoor, A. Samuels, E. Ward, E. J. Feuer, and M. J. Thun. Cancer statistics, 2004. CA: A Cancer Journal for Clinicians, 54:8–29, 2004.
- [84] G. Jozsef, O. E. Streeter, and M. A. Astrahan. The use of linear programming in optimization of HDR implant dose distributions. *Medical Physics*, 30(5):751–760, May 2003.
- [85] D. Kalanovic, M. P. Ottensmeyer, J. Gross, G. Buess, and S. L. Dawson. Independent testing of soft tissue visco-elasticity using indentation and rotary shear deformations. In J. D. Westwood et al., editors, *Medicine Meets Virtual Reality* 11, pages 137–143. IOS Press, Jan. 2003.
- [86] H. Kataoka, T. Washio, K. Chinzei, K. Mizuhara, C. Simone, and A. Okamura. Measurement of tip and friction force acting on a needle during penetration. In Medical Image Computing and Computer Assisted Intervention, pages 216–223, 2002.
- [87] M. Kessler, M. Roberson, R. Zeng, and J. Fessler. Deformable image registration using multiresolution B-splines. *Medical Physics (Abstract)*, 31:1792, 2004.
- [88] Y. Kim. Image-Based High Dose Rate (HDR) Brachytherapy for Prostate Cancer. PhD thesis, University of California, Berkeley, Dec. 2003.
- [89] Y. Kim, S. M. Noworolski, J. Pouliot, I.-C. J. Hsu, D. B. Vigneron, and J. Kurhanewicz. Expandable and rigid endorectal coils for prostate MRI: Impact on prostate distortion and rigid image registration. *Medical Physics*, 32(12):3569–3578, Dec. 2005.
- [90] P. Kneschaurek, W. Schiess, and R. Wehrmann. Volume-based dose optimization in brachytherapy. *Int. J. of Radiation Oncology, Biology, Physics*, 45(3):811–815, 1999.
- [91] J. Kreke, A. J. Schaefer, M. Roberts, and M. Bailey. Optimizing testing and discharge decisions in the management of severe sepsis. In *Annual Meeting of INFORMS*, Nov. 2005.
- [92] T. A. Krouskop, T. M. Wheeler, F. Kallel, B. S. Garria, and T. Hall. Elastic moduli of breast and prostate tissues under compression. *Ultrasonic Imaging*, 20(4):260–274, Oct. 1998.

- [93] D. Kuban, A. Pollack, E. Huang, L. Levy, L. Dong, G. Starkschall, and I. Rosen. Hazards of dose escalation in prostate cancer radiotherapy. *Int. J. of Radiation Oncology*, *Biology, Physics*, 57(5):1260–1268, 2003.
- [94] J. Kurhanewicz, M. Swanson, S. J. Nelson, and D. Vigneron. Combined magnetic resonance imaging and spectroscopic imaging approach to molecular imaging of prostate cancer. *Journal of Magnetic Resonance Imaging*, 16:451–463, 2002.
- [95] J. Kurhanewicz, D. Vigneron, and S. J. Nelson. Three-dimensional magnetic resonance spectroscopic imaging of brain and prostate cancer. *Neoplasia*, 2:166–189, 2000.
- [96] J. Kurhanewicz, D. B. Vigneron, H. Hricak, P. Narayan, P. Carroll, and S. J. Nelson. Three-dimensional H-1 MR spectroscopic imaging of the in situ human prostate with high (0.24-0.7-cm3) spatial resolution. *Radiology*, 198(3):795–805, Mar. 1996.
- [97] J. Kurhanewicz, D. B. Vigneron, H. Hricak, F. Parivar, S. J. Nelson, K. Shinohara, and P. R. Carroll. Prostate cancer: Metabolic response to cryosurgery as detected with 3d H-1 MR spectroscopic imaging. *Radiology*, 200(2):489–496, Aug. 1996.
- [98] B. Lachance, D. Beliveau-Nadeau, E. Lessard, M. Chretien, I. C. Hsu, J. Pouliot, L. Beaulieu, and E. Vigneault. Early clinical experience with anatomy-based inverse planning dose optimization for high-dose-rate boost of the prostate. *Int. J. of Radia*tion Oncology, Biology, Physics, 54:86–100, 2002.
- [99] M. Lahanas, D. Baltas, S. Giannouli, N. Milickovic, and N. Zamboglou. Generation of uniformly distributed dose points for anatomy-based three-dimensional dose optimization methods in brachytherapy. *Medical Physics*, 27(5):1034–1046, May 2000.
- [100] M. Lahanas, D. Baltas, and N. Zamboglou. Anatomy-based three dimensional dose optimization in brachytherapy using multiobjective genetic algorithms. *Medical Physics*, 26(9):1904–1918, 1999.
- [101] M. Lahanas, D. Baltas, and N. Zamboglou. A hybrid evolutionary algorithm for multiobjective anatomy-based dose optimization in high dose rate brachytherapy. *Physics* in Medicine and Biology, 48:399–415, 2003.
- [102] J.-C. Latombe. Robot Motion Planning. Kluwer Academic Pub., 1991.
- [103] J.-C. Latombe. Motion planning: A journey of robots, molecules, digital actors, and other artifacts. *Int. J. of Robotics Research*, 18(11):1119–1128, Nov. 1999.
- [104] J.-P. Laumond, P. E. Jacobs, M. Taïx, and R. M. Murray. A motion planner for nonholonomic mobile robots. *IEEE Trans. on Robotics and Automation*, 10(5):577 – 593, Oct. 1994.
- [105] S. M. LaValle. *Planning Algorithms*. Cambridge University Press, 2006.
- [106] E. Lessard. Development and clinical introduction of an inverse planning dose optimization by simulated annealing (IPSA) for high dose rate brachytherapy. *Medical Physics (Thesis abstract)*, 31(10):2935, 2004.
- [107] E. Lessard, I.-C. J. Hsu, and J. Pouliot. Inverse planning for interstitial gynecological template brachytherapy: truly anatomy based planning. *Int. J. of Radiation Oncology*, *Biology*, *Physics*, 54(5):1243–1250, 2002.

- [108] E. Lessard and J. Pouliot. Inverse planning anatomy-based dose optimization for HDR-brachytherapy of the prostate using fast simulated annealing algorithm and dedicated objective function. *Medical Physics*, 28(5):773–779, May 2001.
- [109] G.-R. Liu. Mesh free methods: moving beyond the finite element method. CRC Press,, 2003.
- [110] W. E. Lorensen and H. E. Cline. Marching Cubes: A high resolution 3D surface construction algorithm. *Computer Graphics (Proceedings of SIGGRAPH '87)*, 21(4):163–169, 1987.
- [111] A. Mamoudieh, C. Tremblay, L. Beaulieu, B. Lachance, F. Harel, E. Lessard, J. Pouliot, and E. Vigneault. Anatomy based inverse planning dose optimization in HDR prostate implant: A toxicity study. *Radiotherapy and Oncology*, 75(3):318–324, June 2005.
- [112] K. Masamune, L. Ji, M. Suzuki, T. Dohi, H. Iseki, and K. Takakura. A newly developed stereotactic robot with detachable drive for neurosurgery. In *Medical Image Computing and Computer Assisted Intervention*, 1998.
- [113] C. Ménard, R. Susil, P. Choyke, G. Gustafson, W. Kammerer, H. Ning, R. Miller, K. Ullman, N. Crouse, S. Smith, E. Lessard, J. Pouliot, V. Wright, E. McVeigh, C. N. Coleman, and K. Camphausen. MRI-guided HDR prostate brachytherapy in a standard 1.5T scanner. Int. J. of Radiation Oncology, Biology, Physics, 59(5):1414–1423, 2004.
- [114] C. Mendoza and C. Laugier. Simulating soft tissue cutting using finite element models. In *Proc. IEEE Int. Conf. on Robotics and Automation*, pages 1109–1114, Sept. 2003.
- [115] M. Moll, K. Goldberg, M. Erdmann, and R. Fearing. Orienting micro-scale parts with squeeze and roll primitives. In *Proc. IEEE Int. Conf. on Robotics and Automation*, May 2002.
- [116] O. Morin, A. Gillis, J. Chen, M. Aubin, M. K. Bucci, M. Roach, and J. Pouliot. Megavoltage cone-beam CT: System description and IGRT clinical applications. *submitted to Medical Dosimetry: Special Issue on Image-Guided Radiation Therapy (IGRT)*, 2006.
- [117] G. C. Morton. The emerging role of high-dose-rate brachytherapy for prostate cancer. *Clinical Oncology*, 17:219–227, 2005.
- [118] S. G. Nash and A. Sofer. Linear and Nonlinear Programming. McGraw-Hill, 1996.
- [119] R. Nath, L. L. Anderson, G. Luxton, K. A. Weaver, J. F. Williamson, and A. S. Meigooni. Dosimetry of interstitial brachytherapy sources: recommendations of the AAPM Radiation Therapy Committee Task Group No. 43. *Medical Physics*, 22(2):209–234, Feb. 1995.
- [120] National Center for Health Statistics. Prostate disease. Available: http://www.cdc.gov/nchs/fastats/prostate.htm, May 2004.
- [121] H.-W. Nienhuys. Cutting in Deformable Objects. PhD thesis, Utrecht University, June 2003.

- [122] J. F. O'Brien and J. K. Hodgins. Graphical modeling and animation of brittle fracture. In *Proc. of SIGGRAPH 99*, pages 137–146, Aug. 1999.
- [123] A. M. Okamura, C. Simone, and M. D. O'Leary. Force modeling for needle insertion into soft tissue. *IEEE Trans. on Biomedical Engineering*, 51(10):1707–1716, 2004.
- [124] M. D. O'Leary, C. Simone, T. Washio, K. Yoshinaka, and A. M. Okamura. Robotic needle insertion: Effects of friction and needle geometry. In *Proc. IEEE Int. Conf. on Robotics and Automation*, pages 1774–1780, Sept. 2003.
- [125] W. Park, J. S. Kim, Y. Zhou, N. J. Cowan, A. M. Okamura, and G. S. Chirikjian. Diffusion-based motion planning for a nonholonomic flexible needle model. In *Proc. IEEE Int. Conf. on Robotics and Automation*, pages 4611–4616, Apr. 2005.
- [126] G. Picinbono, H. Delingette, and N. Ayache. Nonlinear and anisotropic elastic soft tissue models for medical simulation. Proc. IEEE Int. Conf. on Robotics and Automation, pages 1370–1375, May 2001.
- [127] B. Pickett, E. Vigneault, J. Kurhanewicz, L. Verhey, and M. Roach. Static field intensity modulation to treat a dominant intraprostatic lesion to 90 Gy compared to seven field 3-dimensional radiotherapy. *Int. J. of Radiation Oncology, Biology, Physics*, 43:921929, 1999.
- [128] J. Pouliot, A. Bani-Hashemi, J. Chen, M. Svatos, F. Ghelmansarai, M. Mitschke, M. Aubin, P. Xia, O. Morin, K. Bucci, I. M. Roach, P. Hernandez, Z. Zheng, D. Hristov, and L. Verhey. Low-dose megavoltage cone-beam CT for radiation therapy. *Int. J. of Radiation Oncology, Biology, Physics*, 61:552–560, 2005.
- [129] J. Pouliot, Y. Kim, E. Lessard, I.-C. J. Hsu, D. B. Vigneron, and J. Kurhanewicz. Inverse planning for HDR prostate brachytherapy used to boost dominant intraprostatic lesions defined by magnetic resonance spectroscopy imaging. *Int. J. of Radiation Oncology, Biology, Physics*, 59(4):1196–1207, 2004.
- [130] J. Pouliot, E. Lessard, and I.-C. J. Hsu. Advanced 3D Planning, chapter 21. Medical Physics Publishing, 2nd edition, 2005.
- [131] J. Pouliot, R. Taschereau, C. Coté, J. Roy, and D. Tremblay. Dosimetric aspects of permanent radioactive implants for the treatment of prostate cancer. *Physics in Canada*, 55(2):61–68, 1999.
- [132] W. D. Renner, T. P. O'Conner, and N. M. Bermudez. An algorithm for generation of implant plans for high-dose-rate irradiators. *Medical Physics*, 17(1):35–40, Jan. 1990.
- [133] M. J. Rivard, B. M. Coursey, L. A. DeWerd, W. F. Hanson, M. S. Huq, G. S. Ibbott, M. G. Mitch, R. Nath, and J. F. Williamson. Update of AAPM task group no. 43 report: A revised AAPM protocol for brachytherapy dose calculations. *Medical Physics*, 31(3):633–674, Mar. 2004.
- [134] P. L. Roberson, V. Narayana, P. L. McShan, R. J. Winfield, and P. W. McLaughlin. Source placement error for permanent implant of the prostate. *Medical Physics*, 24:251–257, 1997.

- [135] R. M. Satava. Emerging technologies for surgery in the 21st century. *Archives of Surgery*, 134:1197–1202, Nov. 1999.
- [136] R. M. Satava. Disruptive visions: predictive simulation—between scientific method and clinical trial is the role of modeling and simulation in scientific discovery and validation. *Surgical Endoscopy*, 18:1297–1298, Sept. 2004.
- [137] R. M. Satava. Identification and reduction of surgical error using simulation. *Minimally Invasive Therapy & Allied Technologies*, 14:257–261, 2005.
- [138] J. Scheidler, H. Hricak, D. B. Vigneron, K. K. Yu, D. L. Sokolov, L. R. Huang, C. J. Zaloudek, S. J. Nelson, P. R. Carroll, and J. Kurhanewicz. Prostate cancer: Localization with three-dimensional proton MR spectroscopic imaging-clinicopathologic study. *Radiology*, 213(2):473–480, Nov. 1999.
- [139] C. Schneider, A. M. Okamura, and G. Fichtinger. A robotic system for transrectal needle insertion into the prostate with integrated ultrasound. In *Proc. IEEE Int. Conf. on Robotics and Automation*, pages 2085–2091, May 2004.
- [140] J. Schöberl. Netgen automatic mesh generator. Available: http://www.hpfem.jku.at/netgen/, 2004.
- [141] J. Sellen. Approximation and decision algorithms for curvature-constrained path planning: A state-space approach. In P. K. Agarwal, L. E. Kavraki, and M. T. Mason, editors, Workshop on the Algorithmic Foundations of Robotics, pages 59–67. AK Peters, Ltd., Houston, 1998.
- [142] N. Seymour, A. Gallagher, S. Roman, M. O'Brien, V. Bansal, D. Andersen, and R. Satava. Virtual reality training improves operating room performance: results of a randomized, double-blinded study. *Annals of Surgery*, 236:458–463, Oct. 2002.
- [143] S. Shechter, A. J. Schaefer, S. Braithwaite, M. Roberts, and M. Bailey. The optimal time to initiate HIV therapy. In *Annual Meeting of INFORMS*, Nov. 2005.
- [144] J. Shewchuk. Triangle: A two-dimensional quality mesh generator and delaunay triangulator. Available: http://www-2.cs.cmu.edu/quake/triangle.html, 2003.
- [145] M. Shi, H. Liu, and G. Tao. A stereo-fluoroscopic image-guided robotic biopsy scheme. *IEEE Trans. on Control Systems Technology*, 10(3):309–317, May 2002.
- [146] H. Si. Tetgen: A quality tetrahedral mesh generator and three-dimensional delaunay triangulator. Available: http://tetgen.berlios.de/, Jan. 2006.
- [147] C. Simone and A. M. Okamura. Modeling of needle insertion forces for robot-assisted percutaneous therapy. In *Proc. IEEE Int. Conf. on Robotics and Automation*, pages 2085–2091, May 2002.
- [148] R. Taschereau, J. Pouliot, J. Roy, and D. Tremblay. Seed misplacement and stabilizing needles in transperineal permanent prostate implants. *Radiotherapy and Oncology*, 55(1):59–63, Apr. 2000.
- [149] R. Taschereau, J. Roy, and J. Pouliot. Monte Carlo simulations of prostate implants to improve dosimetry and compare planning methods. *Medical Physics*, 26(9):1952–1959, Sept. 1999.

- [150] R. Taschereau, P. Stauffer, I. Hsu, J. Schlorff, A. Milligan, and J. Pouliot. Radiation dosimetry of a conformal heat-brachytherapy applicator. *Technology in Cancer Research and Treatment*, 3(4), Aug. 2004.
- [151] R. G. Taylor. Models of Computation and Formal Languages. Oxford University Press, 1998.
- [152] R. H. Taylor and D. Stoianovici. Medical robotics in computer-integrated surgery. *IEEE Trans. on Robotics and Automation*, 19(5):765–781, Oct. 2003.
- [153] D. Terzopolous, J. Platt, A. Barr, and K. Fleischer. Elastically deformable models. *Computer Graphics*, 21(4), July 1987.
- [154] M. Tubiana and F. Eschwege. Conformal radiotherapy and intensity-modulated radiotherapy. *Acta Oncologica*, 39(5):555–567, 2000.
- [155] P. J. M. van Laarhoven and E. H. L. Aarts. Simulated Annealing: Theory and Applications (Mathematics and Its Applications). D. Reidel Publishing Company, 1st edition, 1987.
- [156] K. Waters. Muscle model for animating three-dimensional facial expression. *Computer Graphics*, 21(4):17–24, July 1987.
- [157] R. J. Webster III, N. J. Cowan, G. Chirikjian, and A. M. Okamura. Nonholonomic modeling of needle steering. In *Proc. 9th Int. Symp. on Experimental Robotics*, June 2004.
- [158] R. J. Webster III, J. S. Kim, N. J. Cowan, G. S. Chirikjian, and A. M. Okamura. Nonholonomic modeling of needle steering. *Int. J. of Robotics Research*, 25:509 – 525, May 2006.
- [159] R. J. Webster III, J. Memisevic, and A. M. Okamura. Design considerations for robotic needle steering. In Proc. IEEE Int. Conf. on Robotics and Automation, pages 3599–3605, Apr. 2005.
- [160] R. J. Webster III, A. M. Okamura, N. J. Cowan, G. S. Chirikjian, K. Goldberg, and R. Alterovitz. Distal bevel-tip needle control device and algorithm. Provisional patent submitted 5/19/2005, full patent submitted 5/19/2006. US patent application number 11/436,995., May 2005.
- [161] R. Weissleder and U. Mahmood. Molecular imaging. Radiology, 219:316–333, 2001.
- [162] H. M. Westergaard. Theory of Elasticity and Plasticity. Dover Publications, Inc., 1964.
- [163] W. L. Wood. Some transient and coupled problems a state-of-the art review. In R. W. Lewis et al., editors, Numerical methods in transient and coupled problems, chapter 8. Wiley, New York, 1987.
- [164] X. Wu, S. J. Dibiase, R. Gullapalli, and C. X. Yu. Deformable image registration for the use of magnetic resonance spectroscopy in prostate treatment planning. *Int. J. of Radiation Oncology, Biology, Physics*, 58(5):1577–1583, 2004.

- [165] X. Wu, M. Downes, T. Goktekin, and F. Tendick. Adaptive nonlinear finite elements for deformable body simulation using dynamic progressive meshes. *Eurographics*, 20(3):349–358, 2001.
- [166] P. Xia, B. Pickett, E. Vigneault, L. Verhey, and M. Roach. Forward or inversely planned segmental multileaf collimator IMRT and sequential tomotherapy to treat multiple dominant intraprostatic lesions of prostate cancer to 90 Gy. Int. J. of Radiation Oncology, Biology, Physics, 51:244254, 2001.
- [167] D. Yan, D. A. Jaffray, and J. W. Wong. A model to accumulate fractionated dose in a deforming organ. *Int. J. of Radiation Oncology, Biology, Physics*, 44:665–675, 1999.
- [168] T. S. Yoo, editor. Insight into Images: Principles and Practice for Segmentation, Registration, and Image Analysis. AK Peters, 1 edition, 2004.
- [169] Y. Yu, J. Zhang, G. Cheng, M. Schell, and P. Okunieff. Multi-objective optimization in radiotherapy: application to stereotactic radiosurgery and prostate brachytherapy. *Artificial Intelligence in Medicine*, 19:39–51, 2000.
- [170] M. Zaider, M. J. Zelefsky, E. K. Lee, K. L. Zakian, H. I. Amols, J. Dyke, G. Cohen, Y. Hu, A. K. Endi, C. Chui, and J. A. Koutcher. Treatment planning for prostate implants using magnetic-resonance spectroscopy imaging. *Int. J. of Radiation Oncology*, *Biology, Physics*, 47(4):1085–1096, July 2000.
- [171] Y. Zhuang. Real-time simulation of physically realistic global deformations. PhD thesis, University of California, Berkeley, 2000.
- [172] Y. Zhuang and J. Canny. Real-time simulation of physically realistic global deformation. In *IEEE Vis '99 Late Breaking Hot Topics*, 1999.
- [173] O. C. Zienkiewicz and R. Taylor. The Finite Element Method. Butterworth-Heinemann, 5th edition, 2000.